REPORT TITLE: NANOSCALE REINFORCED, POLYMER DERIVED CERAMIC MATRIX COATINGS

TYPE OF REPORT: FINAL SCIENTIFIC/TECHNICAL

REPORTING PERIOD START DATE: AUGUST 1, 2005
REPORTING PERIOD END DATE: JULY 31, 2009

PRINCIPAL AUTHOR: RAJENDRA K. BORDIA (PRINCIPAL INVESTIGATOR

DATE REPORT ISSUED: JUNE 2010

DOE AWARD NO.: DE-FG26-05NT42528

SUBMITTING ORGANIZATION: UNIVERSITY OF WASHINGTON
ADDRESS OF ORGANIZATION: OFFICE OF SPONSORED PROGRAMS
4333 BROOKLYN AVE. NE, BOX 359472
SEATTLE, WA 98195-9472

Abstract

The goal of this project was to explore and develop a novel class of nanoscale reinforced ceramic coatings for high temperature (600-1000 ^{0}C) corrosion protection of metallic components in a coal-fired environment. It was focused on developing coatings that are easy to process and low cost. The approach was to use high-yield preceramic polymers loaded with nano-size fillers. The complex interplay of the particles in the polymer, their role in controlling shrinkage and phase evolution during thermal treatment, resulting densification and microstructural evolution, mechanical properties and effectiveness as corrosion protection coatings were investigated.

Executive Summary

Fe-and Ni-based alloys currently used in coal-fired environments do not possess the requisite corrosion and oxidation resistance for next generation of advanced power systems. One example of this is the power plants that use ultra supercritical steam as the working fluid. The increase in thermal efficiency of the plant and decrease in pollutant emissions are only possible by changing the properties of steam from supercritical to ultra supercritical. However, the conditions, 650ºC and 34.5 MPa, are too severe and result in higher rate of corrosion due to higher metal temperatures. Coating the metallic components with ceramics that are resistant to corrosion, oxidation and erosion, is an economical and immediate solution to this problem.

Good high temperature corrosion protection ceramic coatings for metallic structures must have a set of properties that are difficult to achieve using established processing techniques. The required properties include ease of coating complex shapes, low processing temperatures, thermal expansion match with metallic structures and good mechanical and chemical properties.

Nanoscale reinforced composite coatings in which the matrix is derived from preceramic polymers have the potential to meet these requirements. The research was focused on developing suitable material systems and processing techniques for these coatings. In addition, we investigated the effect of microstructure on the mechanical properties and oxidation protection ability of the coatings. Coatings were developed to provide oxidation protection to both ferritic and austentic alloys and Ni-based alloys).

The coatings that we developed are based on low viscosity pre-ceramic polymers. Thus they can be easily applied to any shape by using a variety of techniques including dip-coating, spray-coating and painting. The polymers are loaded with a variety of nanoparticles. The nanoparticles have two primary roles: control of the final composition and phases (and hence the properties); and control of the shrinkage during thermal decomposition of the polymer. Thus the selection of the nanoparticles was the most critical aspect of this project. Based on the results of the processing studies, the performance of selected coatings in oxidizing conditions (both static and cyclic was investigated.

The specific tasks of the research were:

Task 1: Selection of material systems
- **Subtask 1.1**: Optimization of Polymer/nanoparticle compositions
- **Subtask 1.2**: Densification and microstructure development during pyrolysis
- **Subtask 1.3**: Evaluation of corrosion properties

Task 2: Processing of coatings including optimization of slurry rheology
- **Subtask 2.1**: Development of coating procedures including slurry rheology optimization
- **Subtask 2.2**: Densification and microstructure development of the coatings (multiple coatings if needed)

Task 3: Characterization of coatings (mechanical and environmental)

Subtask 3.1: mechanical property evaluation: hardness, toughness and interfacial properties (adhesion)
Subtask 3.2: Environmental characterization: corrosion and oxidation in simulated coal-fired environment

Work was conducted on all the tasks and the subtask. A series of coatings were developed that have the appropriate characteristics as determined in laboratory setting. The coatings provide excellent oxidation protection to both austentic steel and Ni-based alloys Currently, we are exploring partnerships with national labs and industrial partners to evaluate these coatings in simulated coal fired environments and in the field.

Final Scientific/Technical Report

TABLE OF CONTENTS

LIST OF FIGURES

Figure Number

5.15 Effect of coating on the oxidation of steel (static oxidation test in flowing air for 100 hours at 800 ^{0}C). Note that there is no oxidation layer at the interface and the coating and substrate interface remains chemical and mechanically integral

5.16 Effect of coating on the oxidation of steel (cyclic oxidation test in flowing air for cycling ten times between room temperature and 800 ^{0}C). Note that there is no oxidation layer at the interface and the coating and substrate interface remains chemical and mechanically integral with no signs of delamination.

LIST OF TABLES

Table Number

TASKS AND THE RELEVANT CHAPTERS FOR THEM

Task 1: Selection of material systems (Details in Chapter 1 and 3)

Subtask 1.1: Optimization of polymer/nanoparticle compositions

Subtask 1.2: Densification and microstructure development during pyrolysis

Subtask 1.3: Evaluation of corrosion properties

Task 2: Processing of coatings including optimization of slurry rheology (Details in Chapter 4)

Subtask 2.1: Development of coating procedures including slurry rheology optimization

Subtask 2.2: Densification and microstructure development of the coatings (multiple coatings if needed)

Task 3: Characterization of coatings (mechanical and environmental) (Details in Chapter 5)

Subtask 3.1: mechanical property evaluation: hardness, toughness and interfacial properties (adhesion)

Subtask 3.2: Environmental characterization: corrosion and oxidation in simulated coal-fired environment

CHAPTER I

INTRODUCTION AND BACKGROUND

1.1 Introduction

Ceramic materials are good for high temperature applications mainly because of their unique combination of properties. For instance, mechanically, ceramics are hard and have high modulus so that they can be used as structural materials. Because of their chemical inertness and high melting temperature, ceramics have significant potential in high temperature, chemically aggressive and harsh environments. They either can serve as functional parts themselves, or provide desired protection to other materials in a system, if used as coatings. Due to these properties, ceramics are used in a broad range of applications, including energy conversion, chemical and material processing, automotive, electronic and biomedical devices. However, conventional processing routes using powders require high processing temperatures and have limitations in terms of shapes that can be made. This coupled with the brittle nature of ceramics and the difficulty in machining them has been the primary drawback of ceramics.

An alternative approach to make ceramics involves molecular precursors. It uses organo-elemental compounds called preceramic polymers, which decompose during high temperature pyrolysis to form the derived ceramic. This category of polymers usually contains elements, such as Si, C, Al, N, B, O, Ti, Mo, etc. Upon pyrolysis, ceramic materials can be formed as carbides, nitrides and oxides, or their ternary and quaternary systems providing tailored and unique properties for different applications. This route to make ceramics is called polymer derived ceramics (hereinafter PDCs). In this approach,

not only the pyrolysis and sintering temperatures can be significantly lowered, but also conventional polymer processing techniques can be used to make complex ceramic shapes in the unfired, green state. This is because most of these preceramic polymers are thermosetting materials, which are liquid at room temperature or solid but soluble in common solvents.

Due to these advantages, this approach has drawn significant attention internationally. Research has been focused both on the synthesis of new preceramic polymers and on the ceramics and composites formed after pyrolysis. Groups dedicated in this field of research are largely from Europe (Germany), Japan and the United States. This study aims to address some interesting topics and problems found in one of the most promising areas of PDCs: thermal and environmental barrier coatings for harsh environments.

1.2 Polymer Derived Ceramics

1.2.1 History

Ceramics have a set of outstanding properties for high temperature structural and functional use in corrosive and erosive environments. These include high melting and softening point, high modulus and hardness, outstanding chemical resistance, etc. Among non-oxide ceramics, carbides and nitrides are particularly attractive in a wide range of applications. For example, tailored Si_3N_4 ceramics have been used in engine components due to their superb mechanical properties [1]. This was achieved by a special microstructure design and overcoming (to some extent) the following handicaps for such ceramics.

There are two significant challenges for producing covalent ceramics like SiC and Si_3N_4. One is that their high hardness and brittleness make them difficult to machine and reshape. The other one is that due to the covalent bonding, their diffusion coefficients are poor, therefore, their sintering temperatures are usually very high (1700-2100°C [2]). In most cases, they require liquid phase sintering, and additives to be added, which compromises their high temperature performance.

In order to further optimize the properties of advanced ceramics, novel fabrication techniques are necessary. The aforementioned handicaps have lead to the idea of forming ceramic materials by a polymer pyrolysis route, in which a wet chemistry process is followed by intermediate temperature pyrolysis, resulting in amorphous or nano-crystalline ceramics. As early as 1921, polydiphenylsilanes and later in 1949, polydimethylsilanes were respectively synthesized by Kipping [3] and Burkhard [4] using similar dechlorination reactions (See Equations 1.2.1 and 1.2.2).

$$n \cdot ph_2SiCl_2 \xrightarrow{Na} \left[ph_2Si\right]_n + 2n \cdot NaCl \quad (1.2.1)$$

$$n \cdot \left(CH_3\right)_2SiCl_2 \xrightarrow{Na} \left[\left(CH_3\right)_2Si\right]_n + 2n \cdot NaCl \quad (1.2.2)$$

However, due to technical limitations of that time, it was impossible to determine and characterize the molecular structure, weight distribution, etc, of such organosilicon polymers. No researchers tried to transform these synthesized compounds into ceramic materials either. In the mid 1960's, Chantrell *et al* did some initial work on converting preceramic polymers to ceramics [5]. In the 1970's, there were significant and pioneering research activities in this field. Verbeek *et al* [6, 7] in Germany (on SiCN ceramics), Yajima *et al* [8-15] (on SiC fibers) in Japan and Rice *et al* [16, 17] in USA (on SiC-B_4C) respectively reported their success in producing and characterizing silicon-based non-

oxide ceramics with substantial improvement in mechanical properties. From then on, a large variety of new organosilicon and organoelement polymers have been steadily developed as precursors to Si-based and Al-, B- or Ti-based non-oxide ceramics. Table 1.1 summarizes some representative precursors and their pyrolytic products.

Table 1.1: Preceramic polymers and their pyrolytic non-oxide ceramic products [2].

Ceramic Product	Organoelement Polymer
AlN	$[RAlNH]_n$, $[Cl_2Al\text{-}N(H)Si(CH_3)_3]_n$
BN	$[HNBCl]_3 + ((CH_3)_3Si)_2NH$
BC_4N	$C_5H_5N.BH_3$
BC_2N	$HNC_4H_8NH.BH_3$
B_4C/BN	$[B_{10}H_{12}.H_2N\text{-}CH_2\text{-}CH_2\text{-}NH_2]_2$
SiC	$H\text{-}[CH_3SiH]_n\text{-}H$
SiC/C-composite	$[(CH_3)Si(H)\text{-}CH_2]_n$, $[((CH_3)_2Si)_x(CH_3SiC_6H_5)_y]_n$
$Si_xC_yN_z$	$[CH_3SiHNH]_m.[CH_3SiN]_n$
$Si_xC_yO_z$	$[(CH_3)_2SiO]_m.[CH_3SiO_{1.5}]_n$
TiN	$[(C_4H_9N)_2Ti]_n$
ZrB_2	$Zr[BH_4]_4$

1.2.2 Types of Silicon-based Preceramic Polymers

Preceramic polymers are the organo-element precursor to ceramic materials, which upon pyrolysis can form oxides, silicides, carbide, nitrides and their composites (Examples listed in Table 1.1). Organosilicon polymers and their ceramic products have been studied most intensively by researchers due to their high versatility and promising properties of the ceramics produced from them. Essentially, there are four types of silicon-based preceramic polymers (see below), categorized by their backbone characteristics [2]:

1. Polysiloxanes: $[\text{-}R_2SiO\text{-}]_n$

2. Polysilanes: $[-R_2Si-]_n$
3. Polycarbosilanes: $[-R_2SiCH_2-]_n$
4. Polysilazanes: $[-R_2SiNH-]_n$

We define a term, ceramic yield, α^P as follows (Equation 1.2.3).

$$\alpha^P = \frac{mass_{pyrolyzed\_ceramic}}{mass_{polymer\_precursor}} \quad (1.2.3)$$

A high ceramic yield for preceramic polymers—polymer precursor in the equation—is naturally desired for two reasons: low weight loss and minimal shrinkage. In constrained sintering case, this results in extra advantages like the ease of densification and low residual stress to prevent cracking [18]. Usually, α^P is expected to be greater than 75%, but numbers over 80-85% have been reported on different systems [19, 20].

Figure 1.1 illustrates the four basic elements in silicon-based preceramic polymers: Si, C, N and O, and how their combinations can make up different polymers and ceramics. Notice that there are several types of preceramic polymers in this figure that have not been included into the four main types, because they can be easily categorized into the listed type that contains the same basic elements. However, the two carbodiimides (polysilylcarbodiimides and polysilsesquicarbodiimides) can be seen as the unique combinations of polysilazanes and polycarbosilanes, which contain Si, C, and N elements.

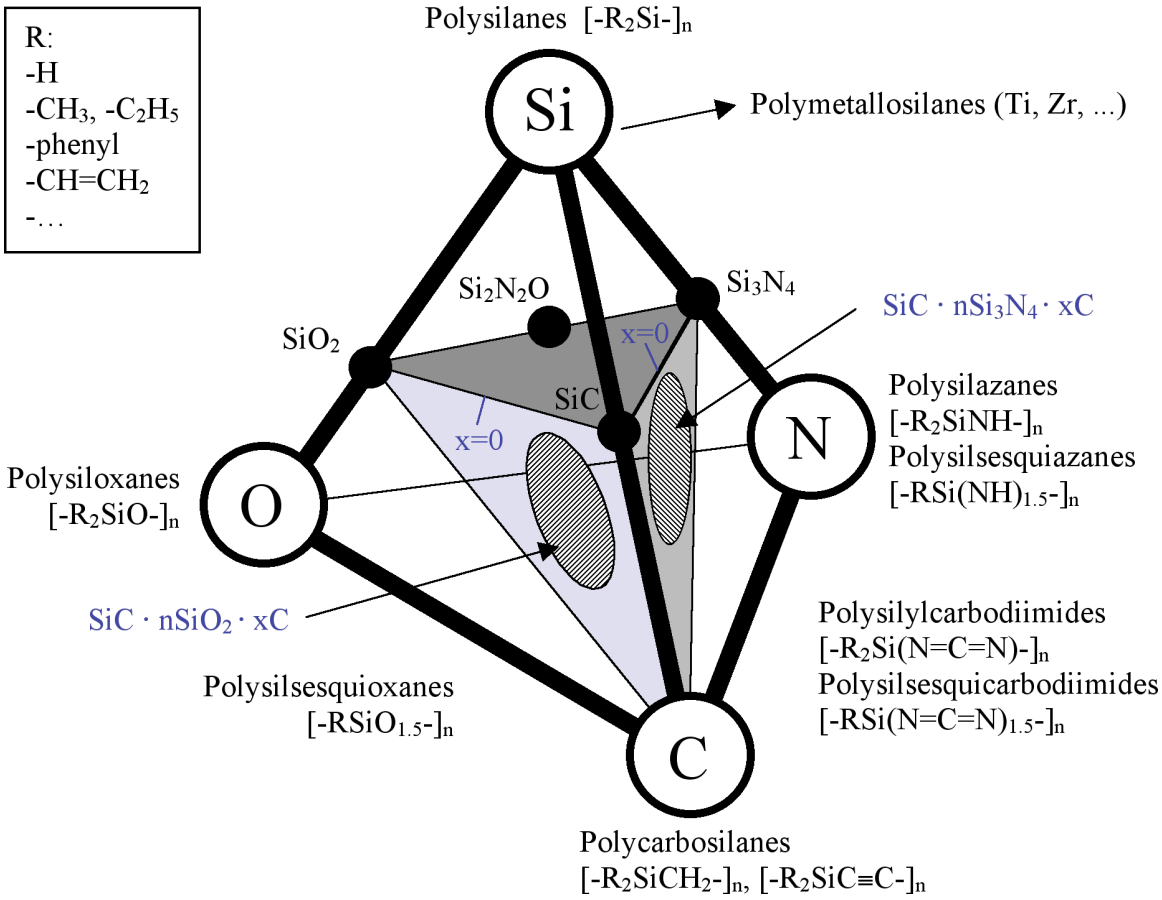

Figure 1.1: Types of silicon-based preceramic polymers and composition regimes for SiCO and SiCN PDCs.

Polysilanes and polycarbosilanes were extensively studied by Yajima *et al* [15] in the 1970s as a precursor to make SiC fibers. This technology was commercially used by Nippon Carbon Co., Ltd. of Japan to produce NICALON™ ceramic fibers in a wide variety of electrical grades, product forms and surface treatment options. Although both polymers can form SiC theoretically, polysilanes are rarely studied due to its low ceramic yield—linear polymers, especially with Si-Si backbone structures, usually have reversion reactions, i.e. the generation of large, volatile molecules and cyclics [21]. Polysilazanes

are quite similar to polycarbosilanes except that nitrogen replaces carbon in the backbone. Consequently, it is an important type of precursors for Si_3N_4 and Si-C-N ceramics.

Polysiloxanes and polysilsesquioxanes have Si-O bonds in the backbone, but the difference is that the latter contain cages or rings in their molecular structures, which can improve the ceramic yield (Figure 1.2). The reason is that these 3-dimensional structures could slow down the kinetics of reversion reactions by hindering the liberation of volatile molecules that are responsible for weight loss during pyrolysis, thus more materials can be kept in the final product [21]. Both of these families are capable of forming oxide ceramics, such as SiO_2, Si-C-O and Si-C-N-O ceramics, depending on the processing atmosphere.

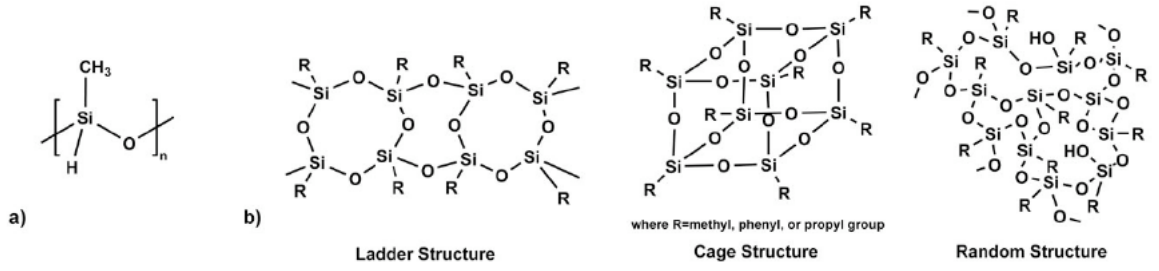

Figure 1.2: Structures of a) polyhydridomethylsiloxane and b) polysilsesquioxane [18].

Based on their kinetic theory, Wynne *et al* [21] proposed that linear-ring polymers and branched-ring polymers would have high ceramic yield due to their ring structures. However, recent improvements in precursor's crosslinking ability have led to the use of linear polysiloxane polymers on the processing of ceramic matrix coatings [19, 22]. An

efficient catalyst is used to foster the in-situ crosslinking at lower temperature (below 150°C) prior to pyrolysis, forming networked 3-dimensional structures that are able to hinder reversion reactions during pyrolysis leading to high ceramic yield. This study also makes use of this preceramic polymer for the fabrication of ceramic matrix coatings, and more technical details are included in Section 4.1.

1.2.3 Processing and Pyrolysis of Preceramic Polymers

The chemical processing route of converting preceramic polymers into ceramics can be summarized into three main steps described by Riedel *et al* [2] as follows:

1. The synthesis of oligomers or polymers from low molecular compounds (precursors), which consist of structural elements as desired in the final product.
2. Chemical or thermal cross-linking of the as-synthesized precursors in order to obtain high molecular compounds convertible into ceramics with high yields.
3. Pyrolysis of the cross-linked polymer providing the desired ceramic material, accompanied by the formation of gaseous reaction products.

Among the three steps above, the first one is usually done by commercial companies, which are now able to provide a large number of ceramic precursors. For researches focused on the ceramic product end, this step looks trivial, however, a comprehensive investigation on the selection of preceramic precursors is crucial in terms of getting a high ceramic yield, desired final composition and expected microstructure and properties. Table 1.1 has already shown some good examples of the relation between different starting materials and their products. It is clear that there are usually multiple options to produce the same ceramic product. Similar polymers might just differ from

each other by replacing side groups, however, small side groups (methyl, ethyl groups) tend to result in lower ceramic yields in inert atmosphere, while large side groups (phenyl, vinyl groups) would result in higher ceramic yields due to better carbon retention [23]. The processing temperature and atmosphere also have significant impact on the final composition and related properties of pyrolytic ceramics. For instance, in a precursor containing carbon element, carbon will mostly remain in the material after being pyrolyzed in inert atmosphere and bond to Si, N or other elements to form non-oxide ceramics, however, it will leave just small amount of residue in the product if pyrolyzed in oxidizing environment, becoming Si-C-O type ceramics. Recently, Torrey *et al* [18, 22] conducted detailed thermal analysis on polysilsesquioxane and polysiloxane polymers in order to determine the best precursor and optimal experiment settings for producing Si-C-O ceramics. This study revealed that in an oxidizing atmosphere, siloxanes with small side groups (hydrogen, methyl groups) had advantages over the compared silsesquioxane polymers due to higher ceramic yield, easy availability and low cost.

During crosslinking, the precursors further condense themselves by rearranging molecular chains in closer packing and starting to form chemical bonds between chains. In the presence of an appropriate catalyst, precursors could be cured at temperatures as low as 100-200°C. This is accompanied by the transformation of the precursor from 2-dimensional linear structure to 3-dimensional network structure. Most preceramic polymers are thermoset materials and can be liquid or solid at room temperature—depending on molecular weight and chemistry. As the crosslinking density increases, liquid polymers transform to solid state to get ready for the following pyrolysis.

In the last step, the amorphous intermediate polymers (after crosslinking) need to be converted to mono- or multi-phased ceramics, and this requires pyrolysis. Terminologically, pyrolysis is different from sintering. In the processing of PDCs, pyrolysis happens first—in the temperature range of 450°C up to 1500°C. It is the decomposition process of the cured precursor, in which organic groups escape in the form of gases, such as H_2, CH_4, CO and H_2O, inorganic atoms receive enough heat to overcome their activation energy, atomic diffusion starts to dominate the movement, covalent bonding between the remained elements starts to form, and therefore the pyrolytic product is further densified comparing to the previous stage. This process completes the conversion from polymer to ceramics [24]. Further heat treatment at higher temperatures (1200-2000°C), i.e. sintering, can be used to densify and alter microstructures. In this range, the material receives enough energy for crystallization and grain growth and nanostructures could thus be formed [25]. At this stage, composition, pore structure and morphology can be tailored by variables like temperature profile, heating rate and reactive/inert atmosphere [18]. Depending on specific applications, not all intermediate polymers need to be fully converted into polycrystalline ceramic materials by sintering. Some multicomponent intermediates will not crystallize until elevated temperatures (>1700°C), but instead, they can be directly used as amorphous materials. Torrey *et al* [26] developed a ceramic composite material based on polysiloxanes, in which the ceramic matrix (-Si-O-) is only pyrolyzed at 800°C, an intermediate temperature resulting in amorphous ceramics, which exhibits satisfactory oxidation protection for steels.

1.2.4 Advantages and Disadvantages of Using Preceramic Polymers

The formation of high temperature ceramics via polymer precursor pyrolysis route is an extension of of the approach used for carbon based materials. The advantage that polymer science has brought to ceramic processing is the versatility of different polymer starting materials, which result in various types of ceramic products, and the ease of tailoring features of pyrolyzed ceramics by modifying polymer's chemistry or processing conditions. During pyrolysis, volatiles are produced, which usually are light molecules dissociated from side groups, such as H_2, H_2O, CH_4, and CO, The bulk of the backbone content gets densified and remains as a solid residue. Therefore, controlling the polymer chemistry directly affects ceramic yield and its final composition. Reactive or inert atmospheres could foster or hinder the interaction between the body being pyrolyzed and the environment, and processing conditions determine porosity, microstructure and grain morphology [23, 27-30].

Higher expectations for further optimization of ceramic properties and the development of new ceramic materials for novel applications also require novel fabrication techniques. Conventional powder processing method is not ideally suited for making high-purity advanced carbide and nitride ceramics and composites due to the limitations of powder processing: impurities in starting materials, inhomogeneity in the final constituents, etc. To overcome these handicaps, chemical vapor deposition (CVD), physical vapor deposition (PVD), sol-gel and polymer pyrolysis technologies have been utilized to make different material systems (Figure 1.3).

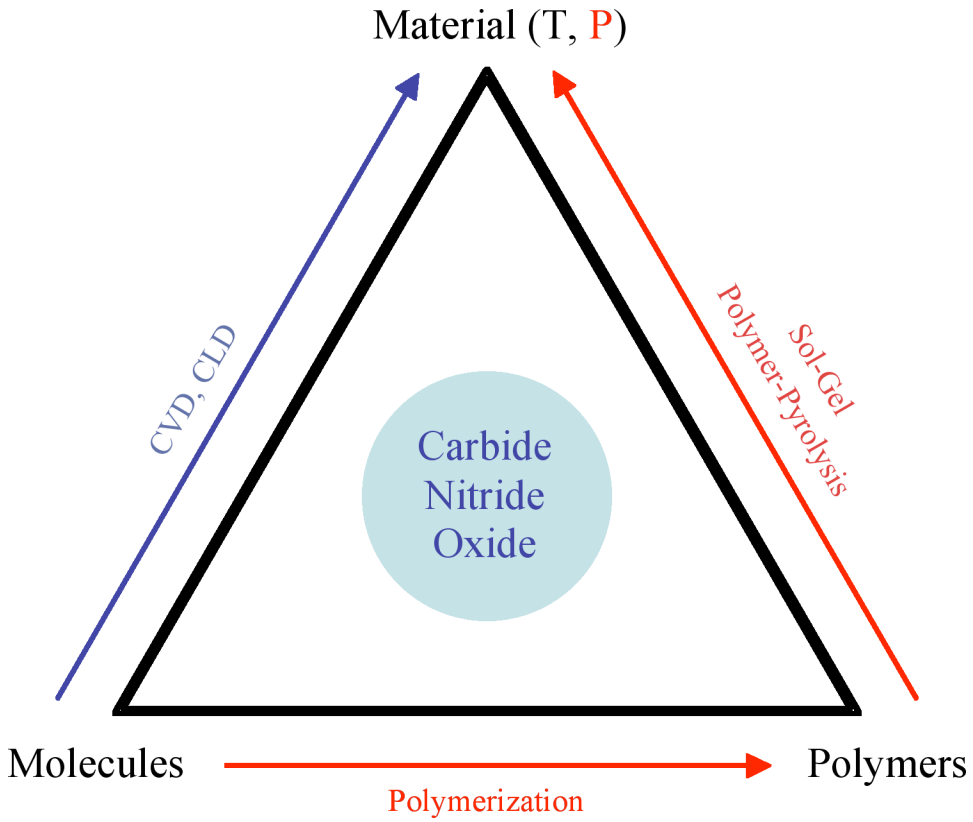

Figure 1.3: Routes for the conversion of precursors into ceramic materials [31].

CVD uses highly volatile compounds, which decompose and precipitate as metals, semi-conductors and oxide or non-oxide ceramics, but the fabrication is too expensive to be widely used in industries, where high performance but low cost is required. Sol-gel method is largely used for the production of oxide ceramics. In contrast, polymer pyrolysis method is capable of making both oxide and non-oxide ceramics. It can fabricate not only multicomponent amorphous materials, which are metastable up to high temperatures, but also nano-crystalline multiphase ceramic composites. Since

majority of the preceramic polymers are liquids at room temperature, they can be easily purified in order to effectively reduce the impurities in the final product and make novel materials by tailoring their composition. Moreover, due to the crosslinking-to-pyrolysis process, no additives are necessary to help sintering.

Another advantage of using polymer pyrolysis method is lowering the processing temperature vastly (800-1600°C). In contrast, covalently bonded non-oxide Si-based ceramics require much higher sintering temperature: 1700-2100°C.

One more significant advantage of the PDC route is that almost all the processing techniques that have been developed for thermosetting polymers (e.g. casting, injection molding, spin coating, dip coating, fiber drawing, infiltration into fiber performs, UV curing and laser curing) can be used to make complex green state components [19, 32-37].

Other advantages include the ability to add precursors and fillers together to make tailored composites and the unique nano-structures that are realized in the resultant ceramic [22, 38, 39].

The biggest disadvantage of using preceramic polymers is the large volumetric shrinkage when the polymer is converted to ceramics. This could be as high as 50-75%, accompanied by doubling the density of the pyrolyzed body from ~1g/cm^3 to greater than 2g/cm^3 [18]. Difficulty in densification is another drawback for PDCs. Typically, in a pressureless pyrolysis, it leaves large porosities partly because of the off-gassing process and the temperature is not high enough for further densification to take place. Greil [24] proposed an innovative method to address this problem, which is called Active Filler Controlled Pyrolysis and will be reviewed in Section 1.3.

1.2.5 Applications of Polymer Derived Ceramics

The advantage of using PDCs over conventionally processed ceramics has lead to a variety of applications, including multicomponent ceramic powders, bulk materials and advanced ceramic fibers [8, 21, 40, 41], ceramic binder and joining materials [15, 20, 42, 43], porous ceramics and foams [44-48], thermal and environmental barrier coatings [22, 26, 38, 49-51], ceramic matrix composites [20, 52-55], high temperature micro-electromechanical systems (MEMS) [33, 56-61]. It is believed that novel applications will continue to evolve as more and more promising material systems are being developed. In this section, several examples are briefly reviewed.

a. Polymer Derived Ceramic Coatings

Ceramic coatings play an important role in providing structural or environmental protection and functionality to a system. Commercially, expensive vapor phase techniques, like PVD and CVD, are used to deposit single or multi-elemental ceramic materials. In contrast, a large number of preceramic polymers are liquid so that low-cost alternatives such as dip-coating, spray-coating and spin-coating can be utilized to deposit polymers or their solutions onto substrates, which can then be converted to ceramic materials. And since the PDC approach is a liquid based technique, it is non-line of sight and able to coat complex shapes.

SiCN ceramic coatings have been produced in multiple ways. Zeigmeister [62] used spray-coating method to make 50 μm-thick SiCN ceramic coating on C/C/SiC substrate; a dense and nearly crack-free coating is achieved by repeating the procedure 4

times. Using a specially tailored ABSE polycarbosilazane solution as precursor for dip- and spray-coating techniques, Motz *et al* [63] coated complex-shaped samples with a ceramic-like coating (at higher temperatures) that has good corrosion and thermal stabilities; moreover, the high flexibility of ABSE film also allows the coating of flexible metal foils. SiCN membranes (200-500 nm thick) can be spin-coated onto a porous Si_3N_4 substrate for hot gas separation applications due to their high temperature stability [64]. Iwamoto *et al* [65] reported such a microporous amorphous membrane that exhibits hydrogen gas permeance of 1.3×10^{-8} mol/m^{2}s Pa at 573 K and the permeability ratio of H_2/N_2 at 141. SiCN coatings can be widely used in wear, erosion or corrosion protection applications [66] as well as microelectronic and optoelectronic devices [67].

SiCO ceramic coatings are attractive to researchers because they can be used as thermal or environmental barrier coatings against harsh environments at elevated temperatures. Fukushima *et al* [68] used transition metals as catalyst and alkoxysilane as precursor to produce SiCO coatings with a crack-free thickness of 0.2 mm after crosslinking; the material shows good flexibility and adhesion to types of plastic substrates due to the high-T^3-ratio structure at the sol stage. Polysiloxanes have a natural advantage of making SiCO ceramic materials because of the incorporation of bonded oxygen in the backbone of the polymer, which does not require inert gas environment sintering. Blum *et al* [19, 69-71] developed a family of linear polysiloxane material, which can be *in situ* crosslinked at low temperature (150°C) and highly converted to ceramics below 450°C. Its suitable viscosity to make slurries for the coating process and low cost (as a byproduct of the silicone industry) have made it an attractive precursor for this purpose. Torrey [18] used polyhydromethylsiloxane (PHMS) as matrix material to

make a type of composite coatings with a tunable thickness of 10-30 μm; active fillers were added to compensate for the shrinkage of the polymer so that low-porosity and crack-free coatings can be formed. It was found that the coating layer can be chemically bonded to the metallic substrates after heat treatment and provide good oxidation protection [26, 51].

Generally speaking, the production of such polymer derived ceramic coatings will suffer from either large shrinkage or porosity. In order to achieve thick, dense and crack-free coatings, multiple deposition steps or usage of filler particles is required. The latter method will be introduced in Section 1.3.

b. Ceramic Matrix Composites (CMC) and Binders

Almost all major Si-based polymers have been used as matrix materials to make composites, including polycarbosilane, polysiloxane and polysilazane. Typically, they are infiltrated (multiple times if necessary) into fiber prepregs or pre-sintered porous ceramics and cured, providing reinforcement and extra protection to the fiber material from severe degradations at elevated temperatures [34, 72-76].

Scheffler *et al* [77] reported a novel approach to form novel ceramic/carbon nanotube composite materials using poly(methylphenylsilsesquioxane) as starting material and nickel particles as the catalyst. In their filler-loaded samples, percolating turbostratic carbon network is formed at 700°C, which leads to significantly higher electrical conductivity. The crosslinked polymer matrix has pores as catalytic microreactors for the formation of multiwall carbon nanotubes (hereinafter CNTs) and SiC/SiO_2 nanowires in them. It was concluded that controlling the catalyst particle

distribution and the generation of transient porosity are the key factors in synthesizing homogeneously distributed CNTs within the PDC matrix. Further development of using similar catalyst-assisted pyrolysis method has shown results of fabricating different nanostructures with different materials. Yang *et al* [78] used polysilazane to synthesize ultra-long single crystalline Si_3N_4 nanobelts, which are 50-100 μm in thickness and 400-1000 μm in width and the formation of these nanobelts is attributed to the anisotropy growth in the early stage. Three years later, they successfully synthesized amorphous SiCN powders containing in-situ formed Si_3N_4 nanowires and nanobelts that are uniformly dispersed within the powder matrix. The novel powders could be used to fabricate nanowire/nanobelt-reinforced ceramic nanocomposites [79].

Using polymer precursors as binders during sintering is an interesting alternative of traditional organic binders, since preceramic polymers would not be completely burnt off during the course but instead converted to ceramics. Yajima *et al* [14, 15] did pioneering work of using polycarbosilane and borodiphenylsiloxane as binders to produce high purity SiC and Si_3N_4 sintered bodies, which have high mechanical strength but can be sintered at significantly lower temperature (1000-1400°C). Wan *et al* [80] showed that, through a prepyrolysis-binding-pyrolysis route, higher density, lower volume shrinkage during consolidation and larger viable material size can be achieved in making SiCN amorphous ceramics and Si_3N_4/SiC nanocomposites, comparing with regular one-step pyrolysis method. Polymer/metal powder composites can also be formed as shown by Seyferth *et al* [81]; in this case, the preceramic polymer serves as a binder for the metal powder in the shaping step and then is consumed during pyrolysis to form the final ceramic part. In order to form mullite, Suttor *et al* [82], Michalet *et al* [54] and

Bernardo *et al* [83] independently reported their work on the novel synthesis of mullite using polysiloxanes; they were able to achieve homogeneous, stoichiometric mullite with low shrinkage and low processing temperature.

c. Spacecraft Thermal Protection System Components

CMC materials are quite attractive for aerospace applications due to their desired mechanical properties, ability to form near-net-shape geometries, tailorable characteristics and lightweight. Preceramic polymers and polymer/filler material systems are currently being investigated to revolutionize the design of both existing and future material components used on space shuttle and astronaut's equipments. Starfire Systems, Inc. is developing a preceramic polymer to be used as a first-aid kit for the thermal protection of ceramics on the wings of NASA space shuttles. The polymer can be directly applied onto damaged parts of the thermal protection shield in space and the pyrolysis takes place *in situ* during the re-entry into atmosphere so that pyrolyzed ceramic residue seals the damaged parts preventing further degradation. By using PDCs, Starfire company claims 33% minimum weight reduction versus metal parts, thermal stability up to 2000°C, tensile strength up to 310 MPa and corrosion resistance [84]. Recently, Andrews Space, Inc. investigated a preceramic-polymer/filler material system to be applied onto Nextel^{TM} thermal resistant fabric, which is part of the ballute design in the Thermal Protection System (hereinafter TPS) for the next generation of NASA space vehicle. This ballute design provides protection for the payload from extreme thermal loads during re-entry and requires non-rigid structure to optimize its packing volume during launch. For a system with a 4,400 kg payload, the appropriate combination of

polymer and fillers has a potential weight saving of 500 kg over a traditional rigid design and 100 kg over flexible designs, which amount to 56% and 23% weight savings respectively [85].

d. Micro-electromechanical Systems (MEMS)

Currently, the most widely used MEMS devices come from electronics industry utilizing silicon-based materials. However, due to the nature of silicon—low fracture toughness (~0.7 $MPa.m^{1/2}$), low softening temperature (600°C) and high reactivity with oxygen and water, silicon has very limited use as a structural material. Hence, there is a need of materials for high-temperature (1000°C) applications of MEMS devices that can either operate in elevated-temperature and harsh environments. Applications include sensors for gas turbine engines, micro power generation systems, etc. Both SiCO and SiCN materials are candidates for these applications due to their superior mechanical properties, especially strength and ability to stand thermal shock [57]. Table 1.2 compares a set of properties among several Si-based materials. As can be seen from this table, SiCN is comparable to SiC and Si_3N_4 as a type of high temperature structural ceramic and much more superior than the rest two in resisting thermal shock.

Table 1.2: Properties of SiCN as compared to other Si-based materials [57].

Property	SiCN	SiC	Si_3N_4
Density [g/cm^3]	2.35	3.17	3.19
E Modulus [GPa]	80-225	405	314
Poisson's ratio	0.17	0.14	0.24
CTE [$\times 10^{-6}/K$]	~3	3.8	2.5
Hardness [GPa]	25	30	28
Strength [MPa]	500-1200	418	700

Toughness [MPa.m$^{1/2}$]	3.5	4-6	5-8
Thermal shock FOM	1100-5000	270	890

A polysiloxane was used to make SiCO micro gears (~0.5 mm in diameter), reported by Harshe *et al* [86]. Similarly, Bertsch et al [87, 88] demonstrated a micro turbine made by combining microstereolithography and thick resist UV lithography methods. Raj's research group focused on the fabrication of MEMS structures using SiCN and they have reported a series of functional MEMS devices, such as micro gear, cantilever beam [58], electrostatic actuator, pressure sensor membrane, combustion chamber [33], lateral thermal actuators, micro-grippers [56], micro glow plug [59], and sensor-igniter [89].

Generally, there are two methods that can be used to build MEMS structures: microcasting and photopolymerization, both of which are schematically shown in Figure 1.4. Detailed discussion of these two methods can be found in references [33, 58].

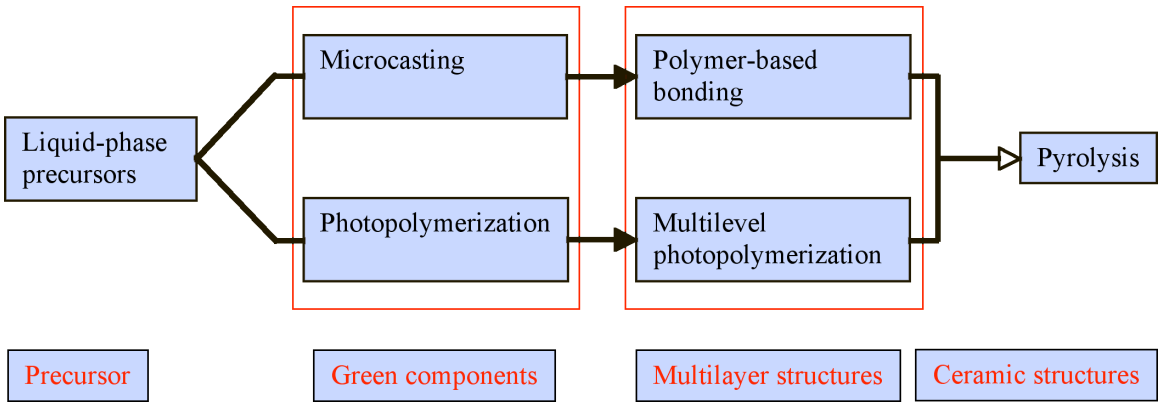

Figure 1.4: Schematic of ceramic MEMS fabrication procedures [57].

e. Ceramic Foams/Porous Ceramics

Applications of cellular ceramics include both structural and functional materials: thermal insulation (at high temperatures in aerospace applications), liquid metal filtration, impact absorption, catalyst supports, and lightweight structures [90-94]. Generally, cellular ceramics possess promising properties, such as low density, low thermal conductivity, low dielectric constant, high thermal shock resistance, high specific strength and high chemical resistance [31]. Both macro-cellular (cell size ranging 100-800 μm) and micro-cellular (cell size ranging 1-100 μm) ceramic foams can be produced, but the process is different.

Usually, macro-cellular ceramic foams are made by using the polymer precursor's natural foaming ability during crosslinking. A novel processing method for producing SiCO foams, reported by Colombo *et al* [95, 96], involves the foaming of a homogeneous solution comprised of a thermosetting silicone resin with or without polyurethane precursors. The green body is pyrolyzed at 1000-1200°C in nitrogen, resulting in bulk densities 0.15-0.60 g/cm^3 (7-28% relative density), and both open and closed macro-cellular foams can be made. The foam has a low thermal expansion coefficient (CTE) of 3.5×10^{-6} K^{-1} and high dimensional stability. Open macro-cellular foams can be further modified with filler powders for electrical conductivity or magnetic properties [93, 97].

For micro-cellular ceramic foams, sacrificial pore formers, for instance PMMA spherical micro beads, are used to create artificial micro pores—these beads are burned

out in air at 250-350°C before pyrolysis. Open porosity can be achieved with bulk densities 0.3-0.6 g/cm^3 (15-30% relative density). Using this method, the compressive strength is 2 to 10 times higher than that of macro-cellular foams of similar density and composition and cell size distribution is more homogeneous [98].

A recent review paper by Colombo summarized main fabrication methods of making cellular ceramics, their mechanical properties and potential applications [99]. Kim *et al* [45, 100-103] reported a series of their work on the processing of both open- and close-cell ceramic foams of mullite, SiC and SiCO, and their mechanical properties.

f. Polymer Derived Ceramic Fibers

The first commercially available PDC fiber is NICALON^{TM} β-SiC continuous fibers as a result of the pioneering work conducted by Yajima in the 1970s [8, 11, 13]. Processing temperature was lowered hundreds of degrees without compromising properties (heat resistance up to 1300°C; 1700°C for HI-NICALON) by utilizing the polymer precursor route. Now it is used as reinforcement in CMCs for applications like hot parts of gas turbines for power generation and aircrafts, where high strength, high elasticity and high thermal resistance are required.

Besides SiC, there exist other types of fibers like Si_3N_4, BN and B_4C that could offer different chemical and environmental compatibilities. Compared to graphite fibers, these fibers have better oxidation resistance; Si_3N_4 and especially BN are superior in dielectric properties, for which glass and Al_2O_3 fibers are even less desirable [21]. Regarding quaternary systems, SiBCN fibers can be synthesized by the pyrolysis of polyborosilazane after melt-spinning [104-106] and they exhibit outstanding durability at

elevated temperatures where carbide fibers could not stand. A potential application for SiBCN fibers is hot engine parts.

The recent development in the preparation of ceramic fibers via polymer precursor route is reviewed by Miele *et al* [107], and Motz and Bordia [108].

1.3 Active Filler Controlled Pyrolysis

1.3.1 Derivation of the Model

In the early development of PDCs, starting from late 1970s till early 1990s, only low-dimensional products, such as ceramic fibers and coatings, had found practical applications. Dense bulk components were hard to produce directly from organosilicon polymers due to their extremely high volume shrinkage (50% or greater) and significant density increase during the polymer-ceramic conversion—typical preceramic polymers have a density of approximately 1 g/cm^3 and pyrolytic ceramics about 2-3 g/cm^3 (SiO_2, 2.2-2.6 g/cm^3; Si_3N_4 and SiC, 3.0-3.2 g/cm^3) [24]. Extensive cracks and pores would form if structural changes in the polymer-derived phase cannot be relaxed by viscous flow or diffusion processes, therefore, destroy the integrity of the pyrolyzed/sintered body. Even coatings, a type of low-dimensional products, suffer from severe cracking or delamination during pyrolysis when constrained on the substrate. Greil and Seibold [109] defined the total linear shrinkage of a polymer body, ε^P, by

$$\varepsilon^P = 1 - \left(\frac{\alpha^P \beta^P}{1 - V_v} \right)^{1/3} \tag{1.3.1}$$

where V_V is the residual fraction of pores or voids in the ceramic residue after pyrolysis/sintering, α^P is the ceramic yield as defined in (1.2.3) and β^P is the density ratio of polymer to its pyrolyzed product shown in (1.3.2).

$$\beta^P = \frac{density_{polymer\_precursor}}{density_{pyrolyzed\_ceramic}} \tag{1.3.2}$$

The equation assumes isotropic dimensional changes and only when micro-structural relaxation is unconstrained, transient porosity could possibly be eliminated by viscous flow or diffusive material transport, reducing V_V to zero in (1.3.1).

To address the problem of significant shrinkage, if the polymer matrix is filled with inert fillers like SiC, B_4C, Si_3N_4 or BN, the shrinkage of the matrix is reduced due to the filler volume effect. However, if reactive filler particles are used, they react with decomposition products of the polymer phase or a reactive pyrolysis atmosphere forming new compounds, expand in volume, and thus compensate for the shrinkage of the polymer during pyrolysis. In this way, near-net-shape conversion of ceramic body could be achieved. This innovative approach is called active filler controlled pyrolysis (AFCOP) [24, 25, 53, 109]. Figure 1.5 schematically illustrates the concept of this method. “Shrinkage” and “Porosity” in (A) are two extreme cases in polymer-ceramic conversion, but in reality one finds both.

The basic principle for the AFCOP method is discussed in detail in reference [24] and is briefly summarized below.

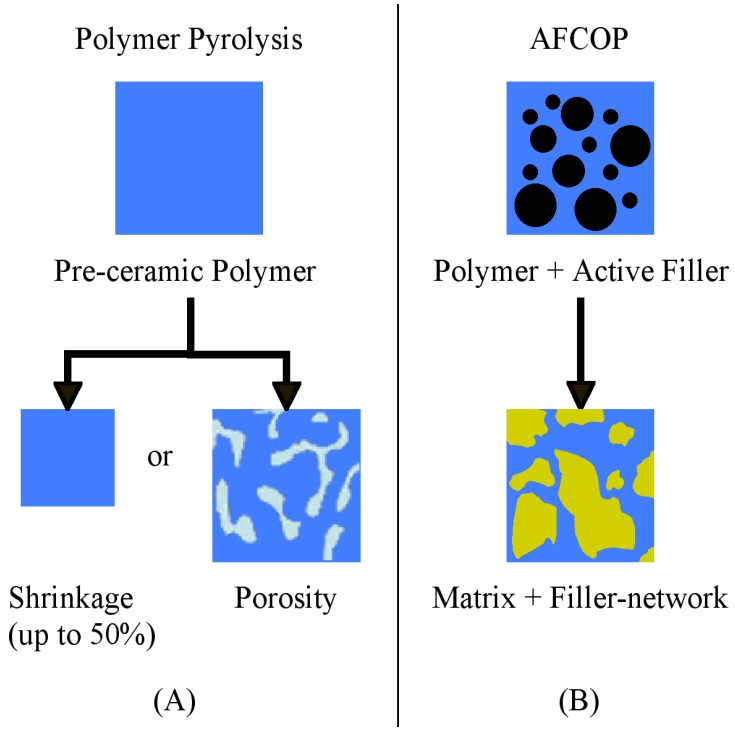

Figure 1.5: Schematic comparison of microstructural changes between (A) Polymer Pyrolysis and (B) AFCOP [24].

Common active fillers, or expansion agents, are elemental metals or intermetallics (T). They react with solid or gaseous decomposition products of the polymer (P), e.g. carbon (K) or hydrocarbon species (G), or pyrolysis atmosphere to form new filler product phase(s) (M), which could be carbides, nitrides or oxides depending on the reactant. In parrallel, preceramic polymer turns into ceramic matrix (C) after pyrolysis. Therefore, the resultant product is a composite material.

$$P(s,l) + T(s) \xrightarrow{\Delta} C(s) + M(s) + G'(g) \tag{1.3.3}$$

The linear expansion value of active fillers, ε^{EA}, is defined by

$$\varepsilon^{EA} = 1 - \left(\alpha^{EA}\beta^{EA}\right)^{1/3} \tag{1.3.4}$$

in which α^{EA} is weight change of active filler phase during pyrolysis and β^{EA} is density ratio of active filler to filler reaction product as shown in (1.3.5) and (1.3.6) respectively.

$$\alpha^{EA} = \frac{mass_{reaction\_product}}{mass_{\exp ansion\_agent}} \tag{1.3.5}$$

$$\beta^{EA} = \frac{density_{\exp ansion\_agent}}{density_{reaction\_product}} \tag{1.3.6}$$

Note that if active filler expands during reaction, the filler expansion characteristics ($\alpha^{EA}\beta^{EA}$) would be greater than unity. In fact, with increasing $\alpha^{EA}\beta^{EA}$ value, the filler volume fraction required to achieve zero-shrinkage pyrolysis declines drastically [109]. Then the total linear shrinkage of a polymer-active filler system, ε^{paf}, can be expressed as

$$\varepsilon^{paf} = \left(\frac{V_T^* - V_T}{V_T^*}\right)\varepsilon^P + V_T\varepsilon^{EA} \tag{1.3.7}$$

in which V_T is the filler loading volume fraction and V_T^* is the critical filler volume fraction in the starting mixture, which determines the maximum particle packing of the reacted filler phase in the pyrolyzed product. Therefore, let the system linear shrinkage be zero, so Equation (1.3.7) transforms to

$$V_T = V_T^*\left\{1 - V_T^*\left(\frac{\varepsilon^{EA}}{\varepsilon^P}\right)\right\}^{-1} \text{ or } \frac{V_T}{V_T^*} = \left\{1 - \frac{V_T^*}{\varepsilon^P}\left[1 - \left(\alpha^{EA}\beta^{EA}\right)^{1/3}\right]\right\}^{-1} \tag{1.3.8}$$

Equation (1.3.8) is the governing equation for calculation of the necessary amount of active filler phase to obtain zero-shrinkage pyrolyzed PDCs. It is essentially a function of the characteristics of both polymer and active filler. In a polymer-active filler system, the active filler particles may change their geometry due to grain growth and fill up excess interparticle volume—caused by polymer shrinkage—with their reaction product.

Assuming a hard spherical shape of the filler particles, the critical filler volume fraction, V_T^*, therefore, can be replaced by the maximum particle density of free filler powder [110], $V_T^{\max}$, for which a typical value of a high-yield polysiloxane with sub-micron filler particles is 0.5 [111]. Note that: this equation assumes that the active filler is fully reacted during pyrolysis, which however might not be the case in reality. For instance, the formation of the oxide outer layer on filler particles would strongly impede their further oxidation during pyrolysis, leaving the core of filler particles unreacted and the volume compensation effect inadequate. Hence, the actual volume fraction of active filler required for zero-shrinkage pyrolysis could be higher than calculated value from Equation (1.3.8) depending on the degree of the reaction. Thus, Equation (1.3.8) is the starting point to calculate the minimum amount of active fillers necessary for zero shrinkage pyrolysis.

1.3.2 Factors Effecting the Transformation Ratio of Filler Particles

In order to increase the transformation ratio of reacted to unreacted active filler particles, two factors could be considered: reduction of the filler particle size and increased reactive gas pressure in the pore channel network. An analysis of this process is also provided in reference [24].

Generally during the pyrolysis process, as temperature increases, polymer starts to decompose (typically 400-800°C) and causes the formation of transient porosity. These pores form an open channel system, which allows both reactive gas molecules from the atmosphere and volatile reactive gas products of polymer decomposition to reach filler particles as shown in Figure 1.6 (Shrinking-core Model). As temperature continues to

increase (800-1000°C and above), filler particles reach their onset temperature of reactions (carburization, nitridation, oxidation, etc); new reaction products gradually fill up the pores that just formed, so when transient porosity is eliminated by filler expansion, it is possible that the whole piece of material can be fully densified without significant volume change.

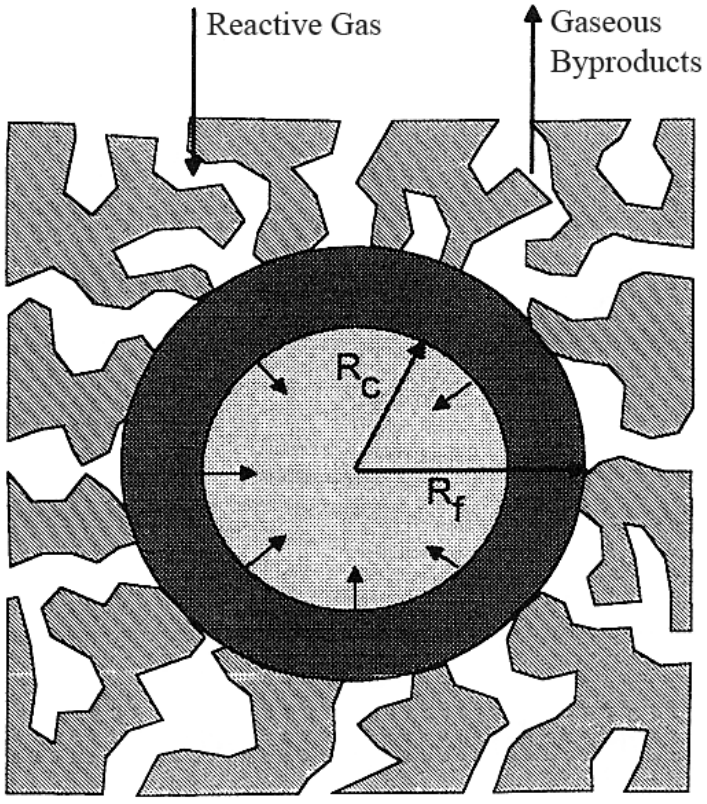

Figure 1.6: Shrinking-core model of filler particle reactions (R_f is starting particle radius, R_c is unreacted core radius at time t) [24].

In the "Shrinking-core Model", the reaction of active filler particles with pyrolysis atmosphere is preferred, since it is shown to result in faster kinetics and more complete

reaction. The total time for complete conversion of a filler particle in a polymer matrix with a reactive gas is proportional to the filler radius, as shown in (1.3.9).

$$t_{total} = \frac{\rho_f R_f}{bC_{gas}}\left(\frac{1}{3k_g} + \frac{R}{6D} + \frac{1}{k_s}\right) \tag{1.3.9}$$

in which ρ_f is the density of the filler, R_f is the initial filler radius, R is the filler radius at time t, b is the number of moles of filler reacting, C_{gas} is the concentration of the gaseous reactant, D_g is the diffusion coefficient of the gaseous reactant, k_g is the mass transfer coefficient between the reactant gas and solid particle, and k_s is the rate constant for the surface reaction. Therefore, decreasing the particle size would lead to shorter reaction time; in other words, a higher fraction of filler particles can be transformed in a given time, resulting in reduced overall shrinkage of the system. This effect was observed by Greil [24] for his work on a 40 vol% $CrSi_2$-filled polysilsesquioxane system pyrolyzed in nitrogen atmosphere and it shows that when particle size is small enough, in this case <5 μm, zero-shrinkage pyrolysis is experimentally achievable (see Figure 1.7).

Secondly, the transformation ratio of reacted to unreacted active filler particles can be further improved by higher reactive gas pressures due to an increased chemical driving force for the filler reaction, as seen in (1.3.10).

$$\Delta G_{P_1} - \Delta G_{P_0} = \int_0^1 \frac{RT}{P} dP = RT \ln \frac{P_1}{P_0} \tag{1.3.10}$$

where P_1 is the higher partial pressure compared to the reference pressure P_0. So that the equation has a positive value, which means the system with a higher applied pressure has greater Gibbs free energy, leading to faster reactions. This is because due to the higher pressure, the mean free path length of gas molecules in the sample is reduced, resulting in

faster diffusional transport and better conversion of filler particles. Upon high enough temperature, open pores gradually turn into closed pores, so that transient porosity is mostly eliminated and the reaction reaches complete.

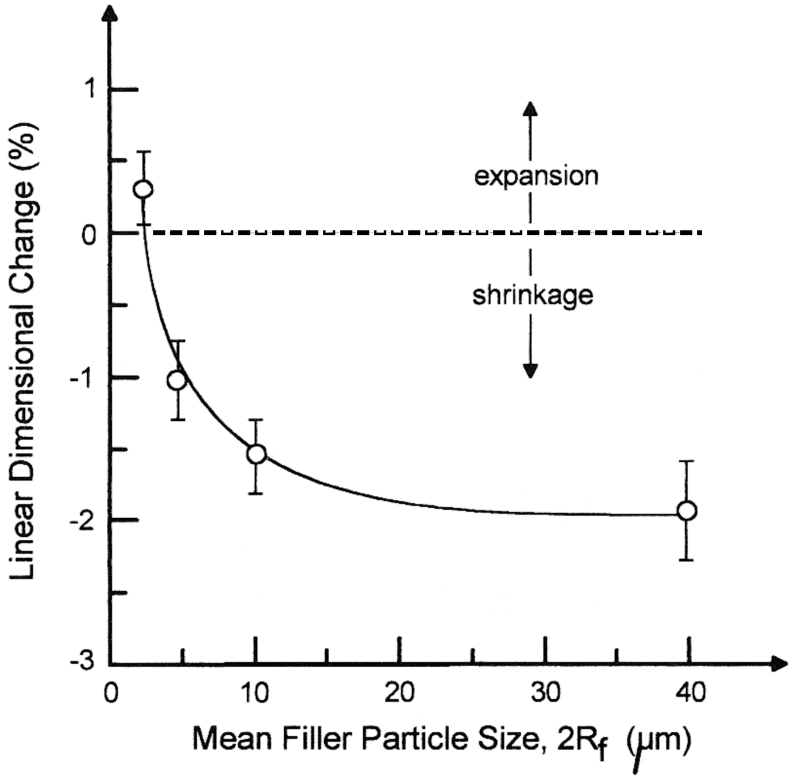

Figure 1.7: Effect of active filler ($CrSi_2$, 40 vol%) particle size on linear shrinkage of the system after pyrolysis at 1400℃ in N_2 [24].

1.4 Processing of Ceramic Matrix Composite Coatings

Many techniques can be used to deposit metal or ceramic coatings onto different substrates, including PVD, CVD, ion implantation, pack coating, electroplating, plasma spraying, hot isostatic pressing, diffusion bonding and sol-gel coating [112]. Except sol-gel coating, all other aforementioned methods usually require high temperature or high-

energy consumption, and could achieve coating thickness from nanometer to millimeter scale. However, they are not feasible in depositing ceramic coatings derived from polymer precursors, which are in liquid state.

Sol-gel coating process utilizes dip-, spin-, spray-coating or painting methods to apply slurries onto a substrate at room temperature, and they can be easily adapted to the processing of preceramic polymers, which was introduced in Section 1.2.3.

In order to make CMC coatings, there are four main steps, summarized by Torrey [18] as follows:

1. Preparation of the preceramic polymer slurry

   It typically consists of three components: preceramic polymer (with or without catalyst), filler particles and solvent. Catalyst may be used to accelerate the crosslinking rate of the polymer. Solvent is added to adjust the viscosity of the slurry, which is crucial in controlling the coating thickness. The solvent must not react with the rest of the materials and should be easy to remove from the system by evaporation.

2. Application of the slurry to the substrate

   As discussed previously in this section, several coating methods can be used to apply slurries onto substrates. The selection of different methods is based on desired coating thickness, surface roughness and geometry complexity. In this study, dip-coating method is used since it can be applied in a controlled manner to flat substrates at ambient temperature.

3. Drying and/or crosslinking of the slurry

Solvent in the "wet" film needs to be removed before the preceramic polymer can be crosslinked. This process usually is quick, since a 2-D coating itself would create a large surface area for the volatile solvent to evaporate. Crosslinking process not only enables polymer molecules to condense and solidify, but also initiate the formation of its 3-D ceramic matrix, within which particle reinforcement phase is distributed uniformly.

4. Thermal pyrolysis to obtain a ceramic coating

Only upon pyrolysis, the polymer phase would convert to amorphous or crystalline ceramic phases, depending on desired properties. Filler particles, if reactive with the pyrolysis atmosphere, start to form products, such as carbides, nitrides, oxides or their combination. The bulk of the coating is further densified in this process. This step completes the processing of such CMC coatings.

1.5 Coating Thickness Control: Landau-Levich Model

1.5.1 Critical Coating Thickness: Experimental Observations

Stackpoole's research [20] on $TiSi_2/TiB_2$-filled poly(ureasilazane) systems has shown that when making ceramic coatings via the AFCOP method, there exists a critical thickness, under which the coating layer is crack free after pyrolysis, but above which cracking and spallation of the coating can be observed. The formation of cracks in such coating systems can be attributed to three main reasons: the mismatch of thermal expansion coefficient (CTE) between the film and the substrate, unrelaxed stresses built up in the coating body during pyrolysis and the friction parameter, k, which is related to

the shear strength of the film-substrate interface and inversely proportional to the slip distance during pyrolysis at the free edge of the coating [113].

In this study, the tendency of coatings to crack due to constrained pyrolysis is considered and efforts are made to ensure that coating thickness is well controlled in order to achieve satisfactory coating quality. Figure 1.8 exhibits the change of critical coating thickness values as a function of the volume fraction of filler particles, V_f, in a $TiSi_2$-filled system. It is obvious to note that for any given V_f value there is a critical coating thickness, and as V_f increases, the critical coating thickness also increases because the average linear shrinkage of the system decreases. For example, at $V_f = 30\%$, the critical coating thickness is ~15μm and increases to ~25μm when $V_f = 40\%$.

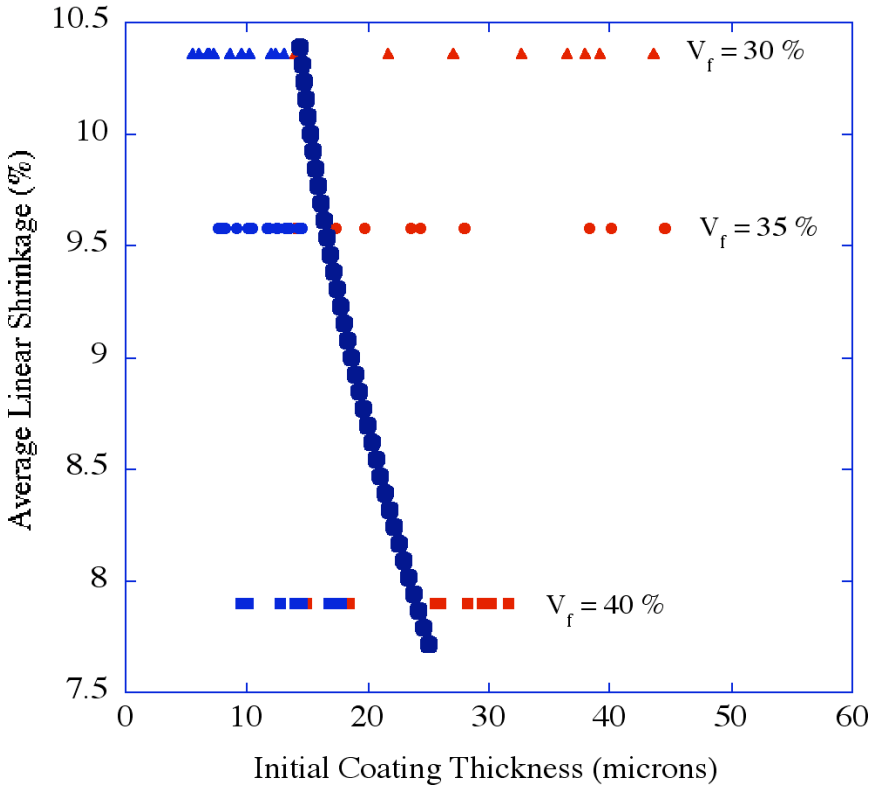

Figure 1.8: The critical thickness of a $TiSi_2$-filled material system with different filler volume fractions (blue dots: crack-free; red dots: cracks form) [20].

The empirical relationship derived from this study for one specific material system has become the motivation of generalizing the scenario and developing a general model that can be applied to other systems.

1.5.2 The Landau-Levich Relationship

By virtue of its simplicity, dip coating is used as the method to coat substrates in this study. The Landau-Levich relationship is a well-established model to predict the thickness of liquid films remained on flat substrates after dip coating.

From a physics point of view, the liquid is entrained and set to motion in the vicinity of a moving plate. This motion is based on two reasons: first, transfer of a momentum from the plate to the viscous liquid; second, the effect of gravity that causes the liquid to drain down simultaneously [114]. Several forces get involved in such a scenario: gravity, viscous stress, surface tension and capillary force—it produces a meniscus near the plate. However, film thickness remains unknown, although it is of great interest to many practical standpoints. The first discussion about this problem was published in a 1942 paper [115], but then corrected by Levich in his book, *Physicochemical Hydrodynamics,* in 1962 [114].

The theory subdivides the liquid surface into two main regions: the entrainment region where the liquid is directly entrained by the motion of the plate to form a adhering layer, a film; and the static meniscus region, away from the film, where its shape stays undistorted by the motion of the plate. Where these two regions meet is called the

transition region or the matching region (see Figure 1.9). Different equations are used to mathematically describe the liquid surface in these two main regions respectively. However, the idea is that they should share the same boundary conditions in the matching region, so that curvature of the liquid surface expressed by the separate equations can be matched in this region. Based on this logic, film thickness can be derived.

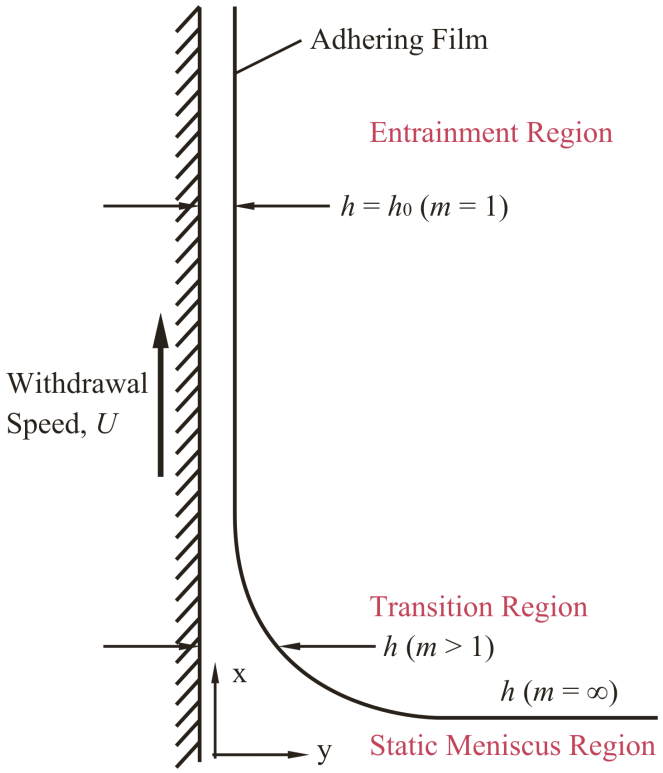

Figure 1.9: Diagram of the dip-coating process. Liquid surface is subdivided into "entrainment region" and "static meniscus region" with a "transition region" in between. h_0 is the film of constant thickness and m is a numerical factor.

In the static meniscus region, the shape of a liquid surface is given by

$$\frac{\frac{d^2h}{dx^2}}{\left[1+\left(\frac{dh}{dx}\right)^2\right]^{3/2}} = \frac{\rho g x}{\sigma} \tag{1.5.1}$$

in which h is film thickness, x is upward vertical direction along the plate, ρ is liquid density, g is gravitational acceleration, and σ is surface tension. The integral of the above equation yields solutions that hold true for the entrainment region too, so that curvature and shape of the liquid surface at this transition region can be matched. Far away from the transition region, i.e. for large x, the assumed conditions are:

$$h \to 0 \tag{1.5.2}$$

$$\frac{dh}{dx} \to 0 \tag{1.5.3}$$

Substituting them in Equation (1.5.1), the following results are obtained:

$$x \to \sqrt{2}\left(\frac{\sigma}{\rho g}\right)^{1/2} \tag{1.5.4}$$

$$\frac{d^2h}{dx^2} \to \sqrt{2}\left(\frac{\rho g}{\sigma}\right)^{1/2} \tag{1.5.5}$$

The value of x, given by Equation (1.5.4), is representative of the end of the transition region. In the entrainment region, a simplified form (with quadratic terms omitted) of the Navier-Stokes equation for steady-state motion (1.5.6) is integrated with respect to speed U at a constant x to obtain a constant flux, Q, over the plate width (1.5.7).

$$\frac{\sigma}{\rho}\cdot\frac{d^3h}{dx^3} + \frac{\mu}{\rho}\cdot\frac{\partial^2 U}{\partial y^2} + g = 0 \tag{1.5.6}$$

$$Q = Uh + \left(\rho g + \sigma \frac{d^3 h}{dx^3}\right)\frac{h^3}{3\mu} \tag{1.5.7}$$

where μ is dynamic viscosity of the liquid, U is plate withdrawal speed, and y is another Cartesian coordinate axis across the film thickness direction (see Figure 1.9). By substituting boundary conditions into (1.5.7), an equation for the constant thickness, h_0, can be obtained and is given by Equation (1.5.8).

Several other authors have tried to modify this original equation [116-119], since it was well known that Landau-Levich equation would overestimate the film thickness. Each modification made some improvement by focusing on certain parameters, such as the effect of high capillary numbers [117], however, none of them greatly differs from the original approximation, so Landau-Levich equation still has a very solid base to be used to predict the thickness of dip-coated films, especially when capillary number (defined in Equation (1.5.9)) is close to zero.

Currently, the most widely accepted form of this equation is derived after some numerical corrections by White and Tallmadge [116],

$$h_0 = \left(\frac{\mu U}{\rho g}\right)^{1/2} f\left(\frac{\mu U}{\sigma}\right) \tag{1.5.8}$$

where the function $f\left(\frac{\mu U}{\sigma}\right)$ takes the form

$$f\left(\frac{\mu U}{\sigma}\right) \approx 0.944\left(\frac{\mu U}{\sigma}\right)^{1/6} \text{ for capillary number } \left(\frac{\mu U}{\sigma}\right) << 1 \tag{1.5.9}$$

$$f\left(\frac{\mu U}{\sigma}\right) \approx 1 \qquad \text{for capillary number } \left(\frac{\mu U}{\sigma}\right) >> 1 \tag{1.5.10}$$

The feasibility of (1.5.10) was questioned when capillary number was large, because the effect of gravitational drainage down the plate is not negligible any more compared with surface tension [116]. Part of this study is going to show that gravitational drainage has a siginificant impact on predicting film thickness even when capillary number is much smaller than unity.

1.6 Ultimate Shear Strength of a Ceramic-Metal Interface

Ceramics, including CMC, are usually used with structural materials, such as metals and alloys, as composites in high temperature applications—refer to Section 1.2.5 for examples. The direct bonding between ceramic and metal creates an interface, for which it is important to understand its failure mechanisms so that material's processing and properties can be optimized. In such circumstances, the substantially different mechanical features of these two classes of materials (CTE, elasticity, etc.) usually lead to the formation of unrelaxed stresses that would induce failures initiated at the interface.

Agrawal and Raj [120, 121] developed a technique and analysis to evaluate the shear strength of a ceramic-metal interface. In their model, a thin film (in nanometer scale) of silica ceramic was deposited onto two types of metal substrates: copper and nickel. By plastically deforming the metal in tension, cracks transverse to the tension direction start to appear on the ceramic film and the strain at this instant is a measure of the tensile fracture strength of the film. As the strain on the ceramic film increases, the crack density increases until it reaches a saturation value. The shear strength of the ceramic-metal interface governs the saturation crack spacing and thus can be experimentally determined.

In such a tension test, two types of fracture should be primarily considered due to tensile and shear stresses at the interface: Mode I Opening and Mode II In-plane Shear (see Figure 1.10). Mode I fracture happens when a tensile normal traction is applied to the interface; if a shear traction is applied, Mode II fracture takes place.

Due to the roughness of the interface, it is essentially a combination of Mode I and Mode II fractures for the fracture at the ceramic-metal inteface. Figure 1.11 illustrates how local tensile stresses would be generated in the non-planar part of the interface, which in general is under shear stress caused by the tension force acted on the substrate.

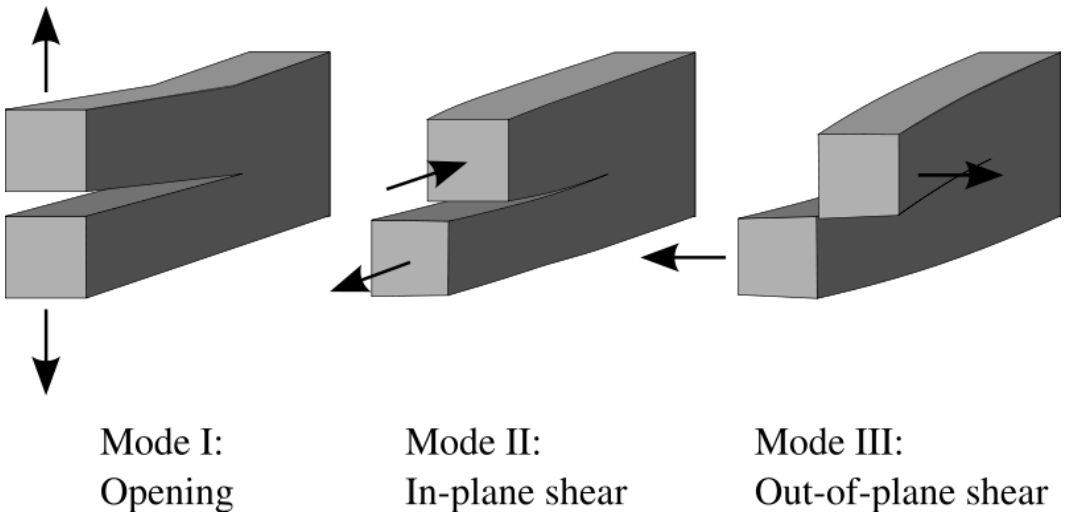

Figure 1.10: Diagram of three types of fracture.

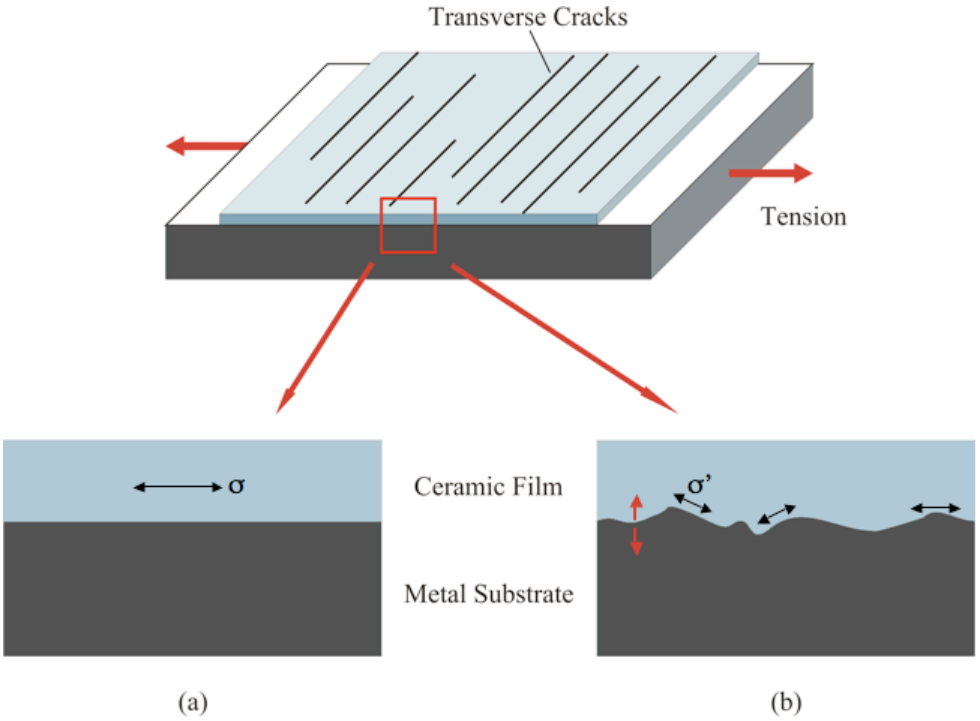

Figure 1.11: Diagram of ceramic film deposited on a metal substrate in tension. Transverse cracks appear. (a) Mode II fracture: an atomically flat interface with uniform through-thickness principal stress, σ; (b) Mode I + II fracture: local tensile stresses and shear yielding.

However, when the film thickness is controlled critically small, Mode I fracture would become unfavorable so that deformation largely takes place in Mode II. There are two criteria for Mode I fracture to satisfy:

1. Local tensile load must be greater than the bond strength of the ceramic-metal interface;
2. There is enough strain energy for the fracture to propagate at the interface, otherwise, Mode I will be suppressed by shear yielding. And the criterion for interfacial crack delamination is given by Equation (1.6.1).

$$\hat{\sigma} \geq \left\{ \frac{2\gamma_c E_1}{\left(1-\nu_1^2\right)\delta} \right\}^{1/2} \qquad (1.6.1)$$

In the above equation [122], $\hat{\sigma}$ is the peak stress in the film and assumed to be equal to the ideal tensile strength of the ceramic, γ_c is the fracture energy for mixed mode loading at the interface, E_1 and ν_1 are elastic modulus and Poisson's ratio respectively for the ceramic, and δ is the film thickness. Agrawal and Raj [121] claimed that the second criterion could not be met in a system with thin films, since not enough strain energy can be stored for the propagation of an interfacial crack in Mode I. Therefore, shear-yielding properties of the interface can be measured using this method.

There are two more assumptions made in this model. First, the plastic strain in the metal, which is experimentally determined, is equal to the elastic strain in the ceramic film. Therefore, the in-plane stress in the film is known from Equation 1.6.2. Second, this in-plane stress is assumed to be uniform throughout the thickness of the film and cannot exceed its ideal tensile strength.

$$\hat{\sigma} = \varepsilon_f E_1 \tag{1.6.2}$$

In Equation 1.6.2, when the fracture strain (ε_f) is applied, the in-plane stress reaches its peak value, namely the tensile strength of the ceramic. This critical strain is defined in Figure 1.12.

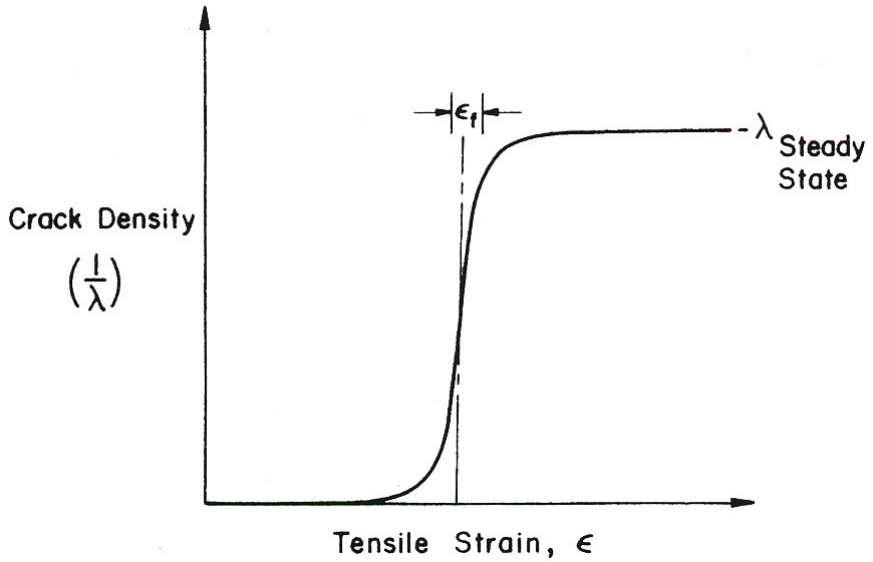

Figure 1.12: Definition of the fracture strain, ε_f, as a function of crack density, which will eventually reach a steady state [121].

Once the in-plane stress is obtained, the shear stress at the interface can be derived through the equation of equilibrium (see Equation 1.6.3) near the edge of a crack in the film [121].

$$\sigma = \frac{1}{\delta}\int_0^{\lambda/2} \tau dx \tag{1.6.3}$$

Then, the shear strength of the interface can be obtained as in (1.6.4) or (1.6.5)—the only difference is that the maximum crack spacing, λ_{max}, can be replaced with the average value of steady state crack spacing, λ_{avg}, using a numerical factor 1.5 (maximum to minimum crack spacing ratio is 2).

$$\hat{\tau} = \frac{\pi\delta}{\lambda_{\max}}\hat{\sigma} \tag{1.6.4}$$

$$\hat{\tau} = \frac{\pi\delta}{1.5\lambda_{avg}}\hat{\sigma} \tag{1.6.5}$$

Using this model, Agrawal and Raj determined the shear strengths of copper-silica and nickel-silica interfaces to be 0.9 GPa and 1.4 GPa respectively. The authors also claimed that the margin of error in this technique is estimated to be less than 20%.

1.7 Open Issues and Challenges

Due to the versatility of available polymer precursors, including those synthesized from research labs, there is a wide variety of possibilities of processing them into ceramic materials for different purposes.

As discussed before, PDCs have significant potential to be used as thermal and environmental barrier coatings (hereafter TBC and EBC respectively) and applied in high temperature or harsh environments. Unlike traditional TBC, there is no alloy (for instance, NiCoCrAlY) bond coat layer to accommodate the thermal expansion mismatch between metal substrate and ceramic top coat in a PDC coating system. Therefore, one of the challenges is to produce PDC coatings with strong ceramic-metal bonds so that it could survive static or cyclic heating and cooling at elevated temperatures. Alternatively, new types of bond coat materials might be introduced into such a system, and its processing method and the optimal combination with PDC coatings need to be developed.

There are other open issues and challenges coming from both science and engineering sides. For example, being able to accurately control coating thickness is one of the most important factors to ensure the quality of the PDC coatings. A few past studies in similar fields presented empirical correlations between processing parameters and resultant coating thickness, but none of them have established quantitative models

that can be generalized to become applicable in different material systems. In addition, suitable characterization techniques for measuring mechanical properties of such CMC coatings need to be established. For the relatively thick coatings in micron-scale that are needed for TBC/EBC applications, some traditional methods like impulse excitation (elastic modulus measurement) and double cantilever beam setup (interfacial toughness measurement) cannot yield reliable results [18]. Therefore, new techniques with *in situ* measurement abilities, such as Atomic Force Microscopy (AFM) and Scanning Thermal Microscopy (SThM), are in demand.

Another open issue, which can have significant applications, is the development of coating systems for nontraditional substrates: flexible substrates and ceramic fiber fabrics. The progress in this field will open up lots of new directions in PDC research, however, there is still a long way to go before reaching that.

CHAPTER II

SCOPE OF THIS WORK

The focus of this research is to develop a novel class of nanoscale reinforced ceramic matrix composite coatings for high temperature (600-1000°C) corrosion and oxidation protection of metallic components. One of the intended applications is the next generation coal-fired power plant. Currently, Fe- and Ni-based super alloys used in coal-fired environments do not possess the requisite corrosion and oxidation resistance for the next generation of advanced power systems. For instance, power plants operating under ultra supercritical conditions, which include three significant factors: higher operating temperature (up to 650°C), higher pressure (34.5 MPa) and oxy-fuel combustion. This would enable the plant to raise its thermal efficiency, decrease the emission of air pollutants such as SO_x, NO_x and CO, and sequester exhaust CO_2 easily. However, higher steam temperatures lead to higher metal temperatures, which results in an accelerated material degradation from severe fireside, coal-ash corrosion and steamside oxidation [123-126], and premature failure of boiler components like tubes in waterwalls, reheater, superheater, etc. Coating the metallic components with corrosion, oxidation and erosion resistant nanoparticle-reinforced ceramic matrix composites is an economical and immediate solution to this problem.

Although this research largely arises from an important industrial need, the basic science behind it is equally important. As a result, this research will be focused on obtaining a fundamental understanding of the processing and properties of corrosion and oxidation resistant coatings for Fe- and Ni-based super alloys in coal-fired environments

using nanoscale reinforced polymer derived ceramic matrix composites. Specifically, this final goal will be accomplished by fulfilling the following objectives:

a. Identification of suitable polymer/active filler systems.
b. Optimization of processing procedure and slurry rheology.
c. Investigation of the fundamental of controlling the thickness of dip-coated films made from complex non-Newtonian slurries.
d. Investigation on effects of processing variables and nanostructures on coating's structural, thermal and mechanical properties.
e. Investigation of the incorporation of PDC bond coat layer to the existing coating system and its effectiveness in improving bond strength.
f. Computer aided simulation in testing and predicting mechanical properties of the ceramic coating and ceramic-metal interface.
g. Study of the effectiveness and performance of coatings as protective layer to the underlying alloy substrates.

In addition to this main project, two related short-term investigations have also been conducted. The first one is the evaluation of the effectiveness of PDC composite coatings as corrosion resistant coatings for highly acidic solutions. The second one is the development of a coating system for ceramic fibers. Important results from these projects will also be discussed.

CHAPTER III

MATERIALS AND EXPERIMENTAL TECHNIQUES

3.1 Materials

3.1.1 Preceramic Polymers

To make filler-reinforced polymer derived ceramic matrix composite coatings, Torrey [18] conducted a comprehensive survey on the selection of preceramic polymers including a variety of silsesquioxanes and a linear siloxane polymer, and finally chose polyhydromethylsiloxane (PHMS) as the optimal polymer precursor. The criteria used for the selection of the polymer are presented in Section 4.1. Using these selection criteria and Torrey's results on commercial siloxanes, PHMS was selected for this study also. PHMS (HMS-992) was purchased from Gelest, Inc. (Morrisville, PA, USA) and its molecular structure was shown in Figure 1.2. Some of its physical properties are summarized in Table 3.1.

Table 3.1: Physical properties of polyhydromethylsiloxane.

Boiling Point [°C]	>205	Melting Point [°C]	<-60
Density [g/cm^3]	0.99	Molecular Weight	1800-2100
Viscosity [cSt*]	25-35	Solubility in Water	Insoluble

* cSt stands for centistokes, a kinematic viscosity unit, which is equivalent to [mm^2 s^{-1}]. Kinematic viscosity can be obtained by $Kinematic\_Viscosity = \frac{Dynamic\_Viscosity}{Density}$.

3.1.2 Expansion Agents

Preliminarily, six intermetallic active filler powders were investigated as potential expansion agents and they are $TiSi_2$, $CrSi_2$, $ZrSi_2$, Ti_3Al, TiAl and $TiAl_3$. The first three belong to the disilicide family, while the latter three are in the aluminide family. Only the suitable fillers that meet the requirements for the proposed application are going to be studied in the further parts of this research. $CrSi_2$ and $ZrSi_2$ (average particle size 1-5μm) were supplied by Atlantic Equipment Engineers (Bergenfield, NJ, USA). Micron size Ti_3Al, TiAl and $TiAl_3$ were obtained from Alfa Aesar (Ward Hill, MA, USA). Submicron powders of $TiSi_2$, $CrSi_2$, $ZrSi_2$ and TiAl were purchased from Accumet Materials, Corp. (Ossining, NY, USA). All powders, except Ti_3Al, were attrition milled for 10 hours in isopropyl alcohol prior to use, using a teflon-coated steel drum and 5mm Yttria-stabilized Zirconia (YSZ) milling media (Union Process, Akron, OH, USA). The milling process primarily aims to remove oxide layer on the particle surface and possibly reduce particle size [20].

3.2 Experimental Techniques

3.2.1 Thermal Analysis: TGA, DTA, Dilatometry

Thermo Gravimetric Analysis (TGA) was used to determine the weight gain of active fillers during oxidation process upon heating. Differential Thermal Analysis (DTA) measures the temperature difference between a sample and an alumina reference material during heating processes. This technique is able to provide temperature specific information about exo- or endothermic reactions that take place, for example, the onset

temperature of filler's oxidation. Simultaneous TG/DTA (STA 409A, Netzsch GmbH, Selb, Germany) experiments were performed on all six active fillers at various heating rates and atmospheres in order to determine the best pyrolysis temperature and heating profile for the coating system. Typical heating rates simulating real pyrolysis process in TGA were 1, 2 and 5°C/min. Isothermal temperature used in such tests was within the range of 800-1000°C with 0-2 hours' holding time. The effect of different atmospheres (air and oxygen) on the kinetics of oxidation of the filler particles was also studied.

A dilatometer (DIL 402C, Netzsch GmbH, Selb, Germany) was used to measure the dimensional change of PHMS from room to pyrolysis temperature. The uniaxial shrinkage of a crosslinked pellet sample was measured from room temperature to 800°C at 2°C/min in air. The result of this test is of importance for a desired near-net-shape pyrolysis.

3.2.2 Microstructural Characterization: SEM

Scanning Electron Microscopy (SEM) was used to image the top surface and cross-sectional microstructures of the coatings. It was carried out on a JSM-7000F (JEOL-USA, Inc., Peabody, MA, USA) in both secondary electron and backscattered electron modes. The cross-sectional specimens were first infiltrated with a low viscosity adhesive (M-Bond 610, Vishay Micro-Measurements, Malvern, PA, USA), sectioned using an ISOMET low speed diamond saw (Buehler Ltd, Lake Bluff, IL, USA), and then mounted in low-shrinkage epoxy (EpoThin®, Buehler Ltd.) between microscope glass slides. They were polished first with silicon carbide sand papers (240, 400, and 600 grits) and to a one-micron finish by using diamond suspension. They were finally polished with

0.05μm colloidal alumina. Samples were cleaned by sonication and sputter coated with platinum prior to imaging.

3.2.3 Physical Characterization: Particle Size, Coating Thickness

In order to study particle size distribution in the starting active fillers and the effectiveness of attrition milling in reducing particle size, a laser particle-sizing instrument (Saturn Digisizer® 5200, Micromeritics Instrument Corp., Norcross, GA, USA) was utilized. This method is based on static light scattering and Mie theory to generate light scattering patterns of tested particles of a specific size in liquid suspension. High-definition CCD is used to capture high-resolution image of the scattering pattern, resulting in a measuring capability of 1000 to 0.1 μm [127]. Particles were first sonicated in isopropyl alcohol to remove agglomerates and then diluted to reach good dispersion before taking measurements. The particle size distribution of both as-received and attrition-milled powders was measured.

Nondestructive coating thickness measurements were carried out on a white-light-interferometer profiling system (WYKO NT3300, Veeco Metrology, Inc., Tucson, AZ, USA). It determines the profile of an object using interferometry instead of a stylus, therefore, "wet" coating samples (un-crosslinked polymer) can be measured. To obtain coating thickness information, a sharp edge was artificially introduced using a razor blade in the middle part of a coating sample transverse to the dip-coating direction, so that the height difference in an area scan near the edge represents the average coating thickness. This method is also able to provide surface morphology information of a sample by 2-D mapping.

3.2.4 Crystalline Phase & Compositional Characterization: XRD, EDS

X-ray Diffraction (Bruker D8 FOCUS, Bruker AXS Inc., Madison, WI, USA) was used to study crystalline phases in raw filler powders and the formation of new phases in both filler particles and polymer matrix due to oxidation and pyrolysis. A Cu-Kα radiation source was used and scans were carried out between the 2θ value of 10-90° with a step size of 0.2 degree. The phase evolution in the PHMS+$ZrSi_2$ coating system as a function of temperature was characterized using powder samples crosslinked at 100°C, and pyrolyzed at 400, 600, 800, 1000, 1200 and 1400°C. Powder samples were ground to <75 μm by pestle and mortar before measurements.

Quantitative Energy Dispersive x-ray Spectroscopy (EDS), coupled with SEM, was used to study the composition spectrum of the coatings. It is especially of interest to map its elemental contents across the coating-substrate interface, where Thermally-Grown-Oxide (TGO) diffusion layer is formed. Low voltage (5-10 keV) and medium probe current were used for the identification of lighter elements.

3.2.5 Rheological Characterization: Viscometry

To understand their rheological properties, viscosity measurements of various slurries (different fillers, compositions, etc) were taken in a Haake VT550 rotational viscometer (Thermo Fisher Scientific, Inc., Waltham, MA, USA) with an SV-2P type of sensor and SVP type of cup. Tests were all at constant room temperature (~20°C), and rotational speed was between 10-300 revolution-per-minute. Different testing modes were used: constant, continuously increasing and stepwise increasing shear rate. They

were aimed to reveal the non-Newtonian nature of complex slurries used in this study: a mixture of intermetallic powder (active fillers), linear Si-based polymer (PHMS) and organic solvent (n-Octane). Viscosity of the slurry has a direct impact on coating thickness control, which makes this investigation a crucial part of the study.

3.2.6 Mechanical Characterization: Hardness, Elastic Modulus, Interfacial Strength

Nano-indentation method has been shown to be a valid method of measuring mechanical properties of this type of ceramic coatings on metal substrates [18]. Hardness and elastic modulus of the coatings can be determined by using a Berkovich diamond indenter attached to Atomic Force Microscopy (AFM). Indents were made on the top surface of the coating with indentation depth less than 10% of coating thickness according to Bückle's rule (there was also study showed that <1% is necessary to obtain the elastic response from coating layer alone [128]). Measurements can be carried out as a function of temperature (from room temperature to 500°C) in conjunction with a Scanning Thermal Microscopy (SThM) setup. Samples pyrolyzed at different temperatures (e.g. 600°C and 800°C) were tested. This study is being conducted in collaboration with professor Tomar's research group at the University of Notre Dame, Notre Dame, IN, USA.

A universal testing machine (Instron 4505, Instron Corporation, Norwood, MA, USA) was utilized to perform tension tests on the coatings to determine the ultimate shear strength of the ceramic-metal interface. At a very slow rate (0.05 mm/s), samples were pulled uniaxially in tension to a series of strains that corresponded to the onset of cracking and saturation crack density. Crack spacing at different strains was then

statistically evaluated using SEM images. The calculation of ultimate shear strength of the interface was done following the Agrawal-Raj model (see Section 1.6) for thin films and a new model for thick films, which was established in this study (see Section 5.2.2).

3.2.7 Finite Element Analysis: ANSYS

ANSYS, a commercial finite element analysis software, was used to build simulation models of the ceramic-metal interface in order to study stress distribution in thick films. The simulation yielded insight into the criteria and assumptions needed for the calculation of the ultimate shear strength and provided a foundation for the thick-film model. The studied object, a unit cell in ANSYS, in cross-sectional view is presented in Figure 3.1. Symmetric boundary condition is used on the left side of the unit cell, whose length is half of that of crack spacing. Bottom of the substrate is fixed, but top surface of the coating is free. Tension force is acted on the substrate in the x-direction. The right side of the coating is a free edge, and this crack surface is traction free. As a consequence, the coating layer can only deform due to the shear stress transferred from the interface. A close-up view of the mesh network around the interface is illustrated in Figure 3.2. Area near interface is built with fine size triangle and square meshes, while area away from the interface is filled with larger size of square meshes. Mechanical properties of the meshes were assigned based on real experimental data, e.g., elastic modulus. Effects of different factors, such as crack spacing, coating thickness, elastic modulus and strain, on the stress distribution in the coating were studied by running simulations under tailored conditions. More technical details and results are included in

Section 5.2.2. The numerical simulation has been conducted in collaboration with doctor Haixia Shang at the University of Washington.

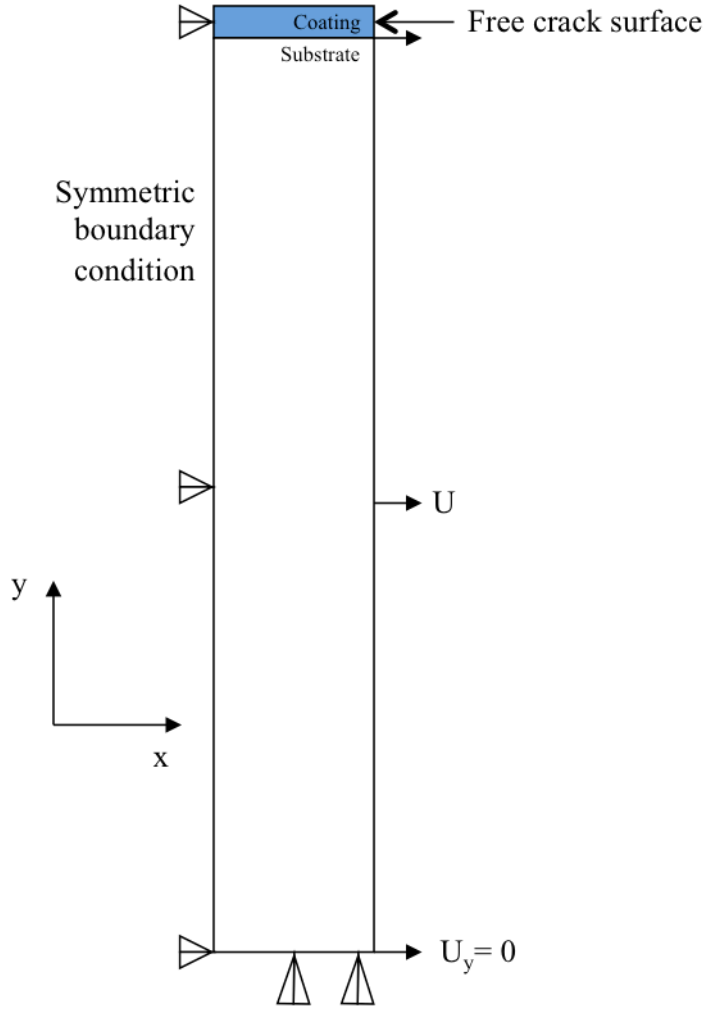

Figure 3.1: The establishment of a unit cell in ANSYS: the cross-sectional geometry of the ceramic-metal interface.

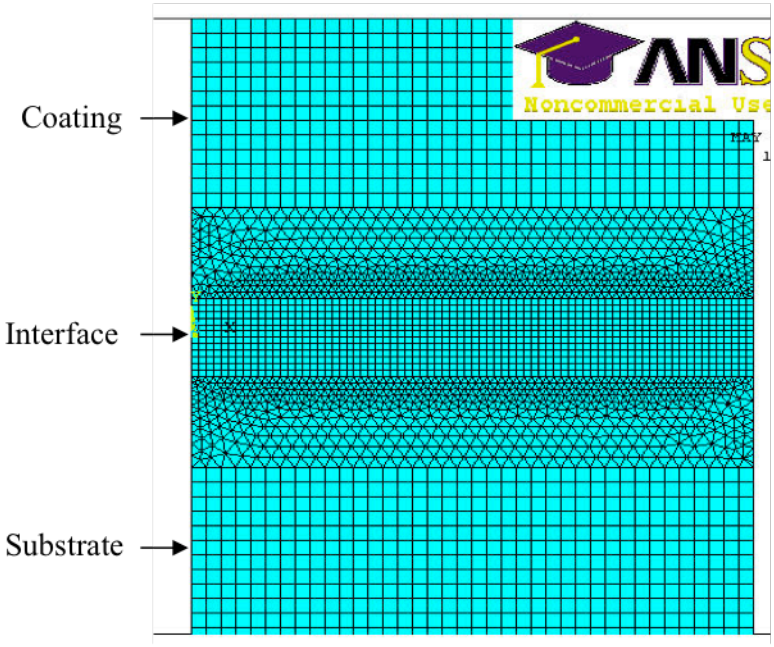

Figure 3.2: A close-up view of the mesh built around the ceramic-metal interface in ANSYS.

CHAPTER IV

PROCESSING OF COMPOSITE COATINGS

4.1 Selection of the Preceramic Polymer

Criteria of selecting a suitable preceramic polymer for the processing of CMC coatings are briefly summarized below [18]:

1. Ceramic yield upon pyrolysis is high (75% or more), which minimizes volume shrinkage due to densification;
2. Pyrolysis temperature is lower than the maximum service temperature of the coated substrate, which is typically 700-1100°C for different grades of stainless steel—this ensures that the substrate does not degrade during the coating processing;
3. Upon pyrolysis, desirable phases should be formed for specified applications. For example, oxide ceramic from both filler and matrix phases is desired for high temperature oxidation and corrosion resistant applications;
4. Polymer is in liquid state or solid state that is easy to dissolve in organic solvent for easy application to the substrate by dip or spin coating, painting, or spraying;
5. A suitable viscosity can be easily achieved and tailored for the coating processing method selected.

Based on the criteria listed above, polyhydromethylsiloxane (PHMS) is chosen as the preceramic polymer for this study. The advantages of using PHMS as polymer precursor include the following: high ceramic yield (α^P>85% when pyrolyzed in air), low

pyrolysis temperature (fully converted <700°C), liquid state at room temperature (ideal for dip coating), in-situ crosslinking (150°C in humid air), and ability to form amorphous SiCO matrix. Figure 4.1 exhibits the weight change, as a function of temperature during pyrolysis, of PHMS and a few other commercial siloxane polymers in air using TGA. As can be seen, PHMS-OH shows the lowest weight loss, which is complete by 700°C.

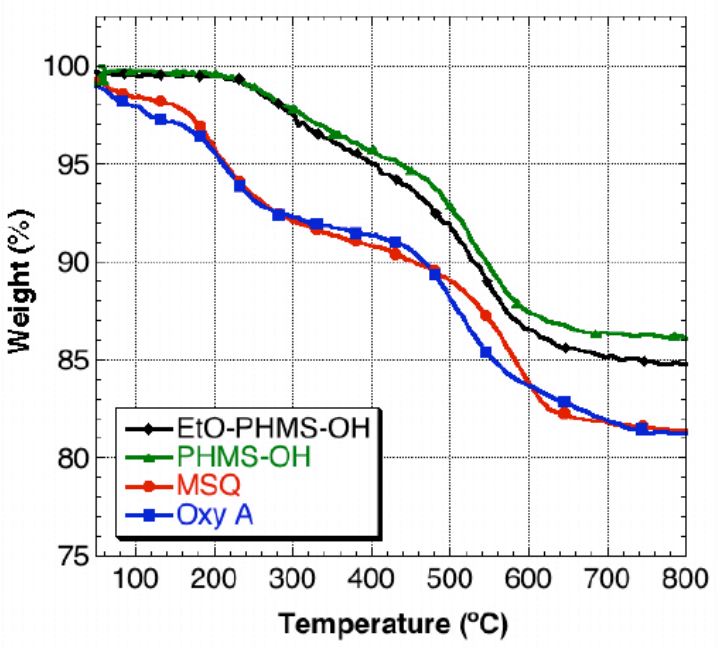

Figure 4.1: Comparison of the weight loss of commercial polymers, MSQ and Oxy A, with PHMS derivatives, EtO-PHMS-OH and PHMS-OH [18]. *MSQ: methyl-silsesquioxane, Oxy A: Oxycarbide A silsesquioxane.*

Dilatometric analysis was performed on the polymer, PHMS, to determine its linear shrinkage (ε^P) upon pyrolysis, so that the filler loading volume fraction required

for zero-shrinkage pyrolysis can be determined by Equation (1.3.8). The total linear shrinkage was found to be 23% when the polymer was heated to 800°C (Figure 4.2).

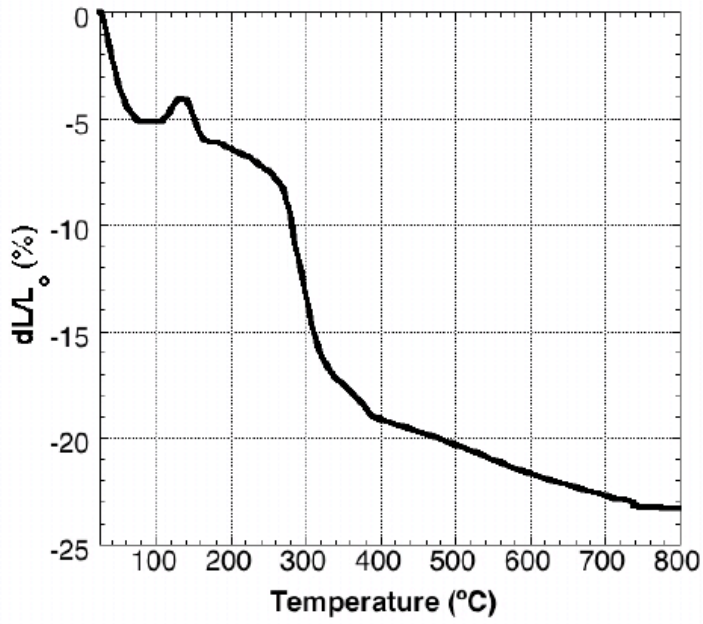

Figure 4.2: Dilatometric measurement on linear shrinkage of PHMS in air [18].

Kinetic study on PHMS has shown that several important reactions occur during crosslinking and pyrolysis [129-131]. Hydrolysis and condensation reactions mainly occur at low temperatures (~150°C) in humid air, and pyrolysis can be achieved around 800°C, resulting in an amorphous SiCO 3-dimensional network. It takes PHMS three major steps to complete pyrolysis, which are schematically depicted in Figure 4.3.

It is worth noting that, when pyrolyzed in air, PHMS tends to form SiCO ceramic with only Si-O and Si-C bonds, but not Si-Si or C-O bonds. The free carbon content has been shown to form turbostratic carbon at high temperatures (1450°C) [23, 132].

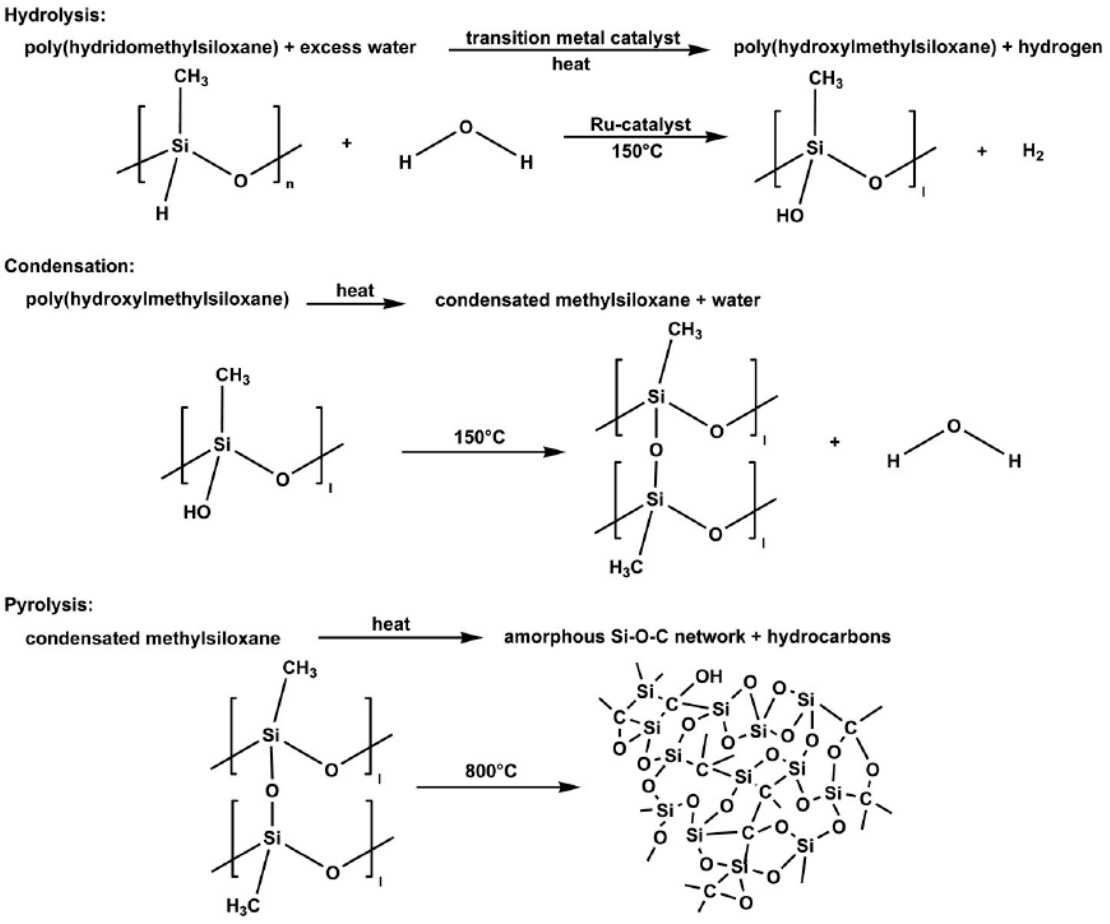

Figure 4.3: Schematic of the hydrolysis, condensation and pyrolysis reactions between PHMS and air [18].

4.2 Selection of Expansion Agents

Six commercially available powders were preliminarily investigated in this study as expansion agent candidates, all of which were reactive intermetallics compounds: $TiSi_2$, $CrSi_2$, $ZrSi_2$, Ti_3Al, TiAl, and $TiAl_3$. Following criteria were considered when evaluating the feasibility of using these compounds as active fillers in this research.

1. Filler particles can be easily dispersed in the mixture of preceramic polymer and organic solvent, and kept as a stable suspension for a reasonable time period;
2. Fast oxidation kinetics in the intermediate temperature range (<1000°C);
3. Availability of nano-scale to sub-micron scale average particle size, which allows fast and high degree of conversion from intermetallics to oxide ceramic phases;
4. Desired oxidation products with the needed oxidation and corrosion resistant properties;
5. Significant volume expansion on conversion from the intermetallics to the oxides.

Thermo Gravimetric Analysis (TGA) and Differential Thermal Analysis (DTA) were used to determine the fillers' weight gain and temperature of conversion to oxides. Table 4.1 summarizes density and formula weight of each filler and their oxide products, which is used to calculate $\alpha^{EA}\beta^{EA}$ (filler expansion characteristics) values. As shown in Section 1.3, a high value of $\alpha^{EA}\beta^{EA}$ leads to high specific volume change. In Table 4.1, all six of these fillers are attractive expansion agents ($\alpha^{EA}\beta^{EA}>1$) and their needed volume fraction (VF) for zero shrinkage pyrolysis has also been calculated.

Table 4.1: Selection of active fillers based on volume expansion.

Filler	Filler Density	Filler Mass	Oxides /Products	Oxide Density	Oxide Mass	α^{EA}	β^{EA}	$\alpha\beta^{EA}$	Volume Fraction*

$TiSi_2$	4.02	104.04	TiO_2+2SiO_2	3.00	200.04	1.923	1.340	2.577	0.2768
$CrSi_2$	4.91	108.17	$0.5Cr_2O_3+2SiO_2$	3.16	196.17	1.814	1.554	2.819	0.2636
$ZrSi_2$	4.88	147.40	ZrO_2+2SiO_2	3.56	243.40	1.651	1.371	2.264	0.2975
$TiAl_3$	3.4	128.81	$TiO_2+1.5Al_2O_3$	4.05	232.81	1.807	0.840	1.518	0.3775
TiAl	3.8	74.85	$TiO_2+0.5Al_2O_3$	4.10	130.85	1.748	0.927	1.620	0.3625
Ti_3Al	4.1	170.58	$3TiO_2+0.5Al_2O_3$	4.14	290.58	1.703	0.990	1.687	0.3536

*Volume Fraction needed for zero-shrinkage (Equation 1.3.8).

Note that VF is in the range of about 25% to 35%, so it is possible to make (filler + polymer) slurries with this VF of the filler. In this perspective, all six of these fillers are also feasible expansion agents for this study.

4.2.1 Disilicides: $TiSi_2$, $CrSi_2$ and $ZrSi_2$

$TiSi_2$, $CrSi_2$ and $ZrSi_2$ belong to the disilicide family. They have been chosen mainly because of the desired oxides they can form upon reaction and the large specific volume change. $TiSi_2$ has already been shown to be a very promising filler for the PHMS coating system [18]. $CrSi_2$ is desirable since Cr is a typical additive element in stainless steel for corrosion protection. Finally, $ZrSi_2$ is expected to form ZrO_2 and zircon phase, $ZrSiO_4$, both of which are excellent high temperature materials. The average particle size of as-received powders is in the 1-5 micron size range. They were attrition milled in isopropyl alcohol solvent for at least 10 hours prior to oxidation kinetics studies in order to remove their protective oxide layer, decrease particle size, and increase powders' reactivity [20].

$TiSi_2$ was heated up to 800°C, while $CrSi_2$ to 1000°C. Two heating rates—1°C/min and 5°C/min—were used for both of them to examine the effect of this variable on the extent of oxidation. Tests were conducted in air and the weight gain was continuously monitored. Figure 4.4 and 4.5 show that better oxidation of filler particles

can be achieved using finer particles in both cases. For $TiSi_2$, the weight gain increases from ~36% to ~60% at 800°C, when particle size is reduced to 0.3-0.9μm by attrition milling (Figure 4.4). The needed weight gain for complete conversion of $TiSi_2$ is 92.3%, which implies that the oxidation of $TiSi_2$ powder is incomplete up to this temperature. Meanwhile, the oxidation kinetics of $CrSi_2$ is poor without milling up to 800°C, and the weight gain is only about 2%, however, it increases to ~37% after attrition milling (Figure 4.5). Again, 37% is much less than the theoretically calculated weight gain of 81.3% for complete conversion.

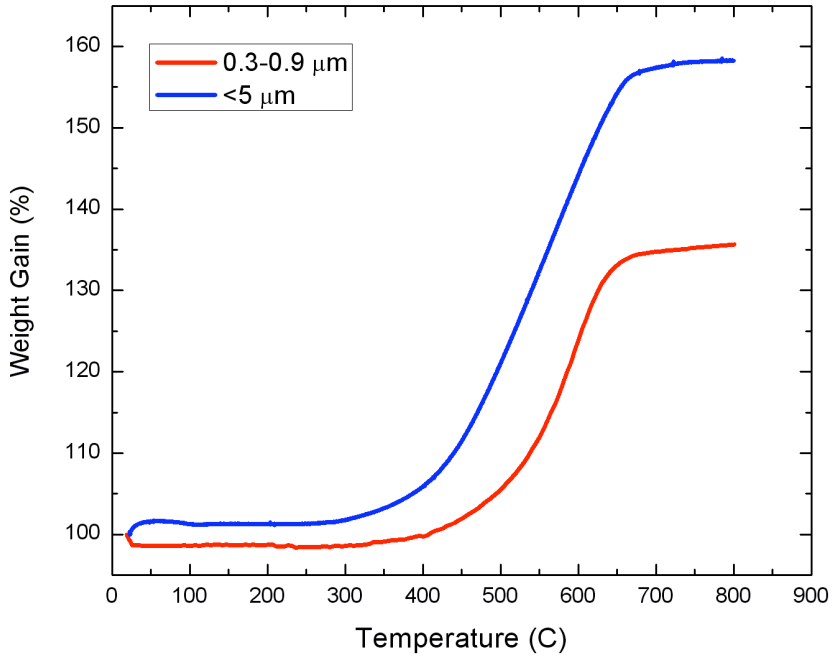

Figure 4.4: Oxidation of $TiSi_2$ in air: milled (0.3-0.9 μm) vs. unmilled (1-5 μm).

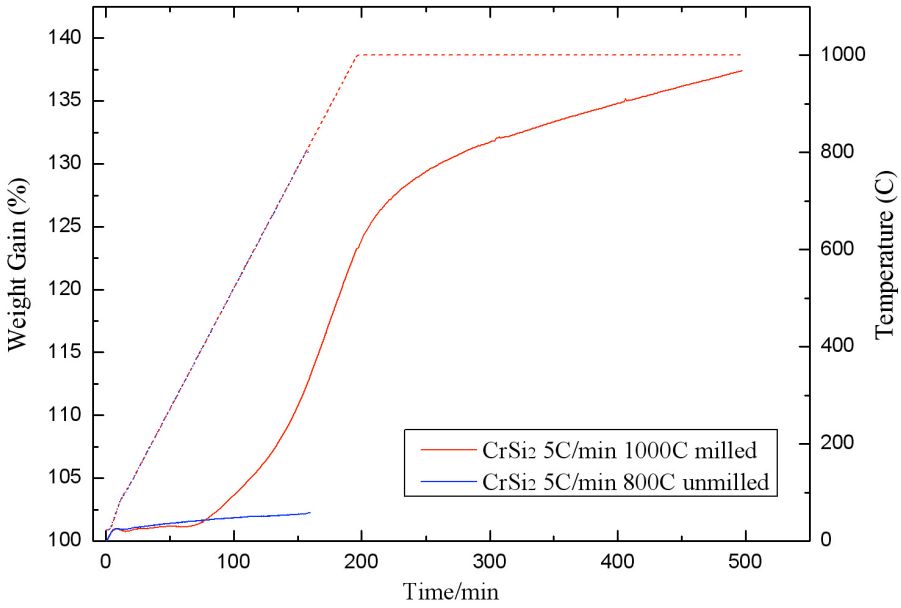

Figure 4.5: Oxidation of $CrSi_2$ in air: milled vs. unmilled.

In Figure 4.5, it is of interest to note that there is a two-hour hold at the isothermal temperature of 1000°C. Since the weight continues to increase even during the hold time, it is clear that this heat treatment is not sufficient to completely convert the milled powders. Samsonov and Lavernko have shown that the oxidation of $CrSi_2$ is very limited at temperatures below 1000°C and the oxidation kinetics is significantly faster at higher temperatures [133]. However, in this research, processing temperature is limited to be below 1000°C (because of the substrate), therefore, higher temperatures were not investigated. One possibility to increase the conversion at lower temperature is to use higher partial pressure of oxygen. Oxidation studies under oxygen were conducted, and found out that the weight gain is greater than 50% at 1000°C, as shown in Figure 4.6.

Both tests used the same experimental settings (heating rate 5°C/min; isothermal temperature 1000°C; isothermal time 5 hours; inert balance gas 50ml/min). The active gas flow was kept at 25 ml/min for air and oxygen respectively. This direct comparison shows an increased oxide yield of ~15% (from 37% to 52%) under higher oxygen partial pressure.

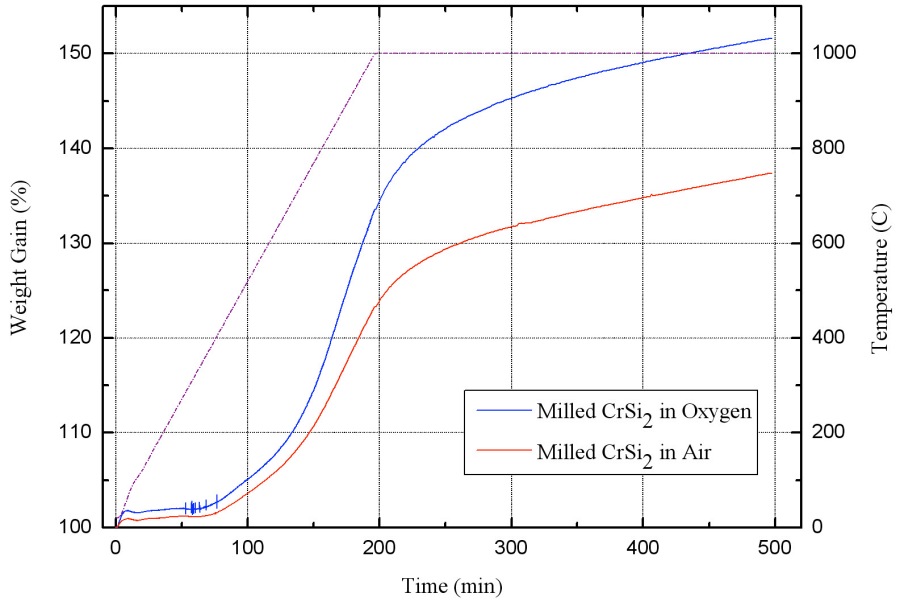

Figure 4.6: Effect of oxygen partial pressure on the conversion of $CrSi_2$.

It is clear that neither $TiSi_2$ nor $CrSi_2$ powders were fully oxidized in the investigated temperature range. Since generally finer particles yield higher oxidation conversion, the difficulty in oxidizing as-received powders of both compounds can be mainly attributed to three reasons: first, the relatively large particle size, which leads to

relatively small surface area available for chemical reactions; second, the existing oxide outer layer on particles, which strongly impedes further oxidation of the interior; and third, during heating, the silicon oxide phase forms at early stages of oxidation and impedes the diffusion of oxygen atoms. Therefore, attrition milling had to be used to break down the oxide layer and reduce particle size. Its effectiveness in reducing the particle size can easily be measured by a light scattering method. Figure 4.7 compares the average particle size of $CrSi_2$ before and after attrition milling. As shown, the milling process drastically reduced its particle size from an average of ~80 μm to ~0.8 μm.

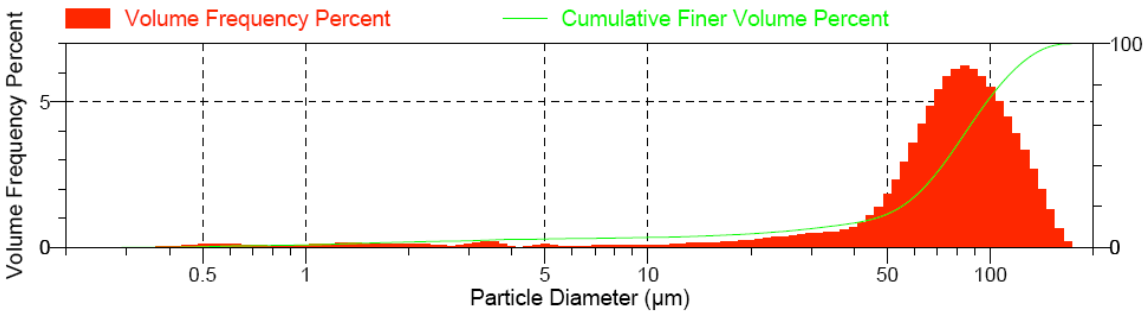

(a) Before milling

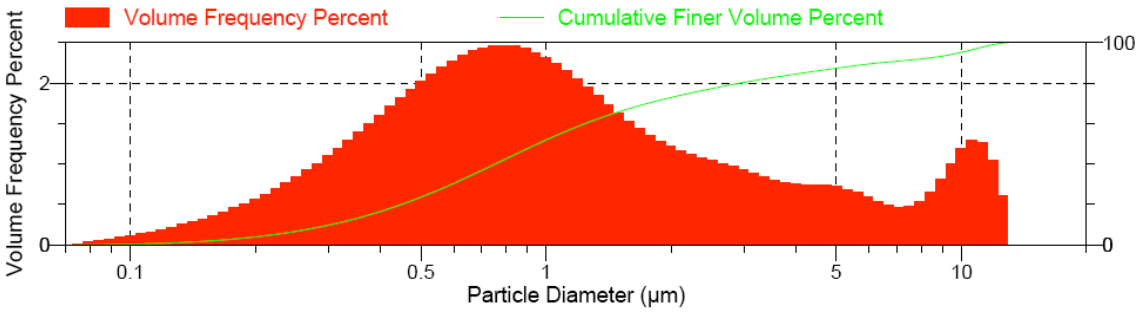

(b) After milling

Figure 4.7: Particle size distribution analysis of $CrSi_2$ powders using a light scattering method.

Gebwein *et al* [134] used $ZrSi_2$ as one of the active fillers to fabricate mullite-zirconia ceramics in a similar method as in this research. $ZrSi_2$ is an attractive filler material since its oxidation product, zirconia, is an outstanding oxidation resistant material and it is able to associate with SiO_2 to form a stable zircon phase ($ZrSiO_4$) at high temperatures. Besides, $ZrSi_2$ compound itself is also highly oxidation resistant within intermediate temperature regime, so even if some $ZrSi_2$ is left un-oxidized or partially oxidized, $ZrSi_2$ phase in the coating is still functional in terms of oxidation protection. $ZrSi_2$ was received as submicron powder and Figure 4.8 shows its oxidation behavior in oxygen atmosphere with a ~50% weight gain at 1000°C. Comparing to its calculated weight gain of 65.1% for complete oxidation, this result is satisfactory. Using oxygen atmosphere instead of air for higher oxygen partial pressure has certainly promoted the oxidation process.

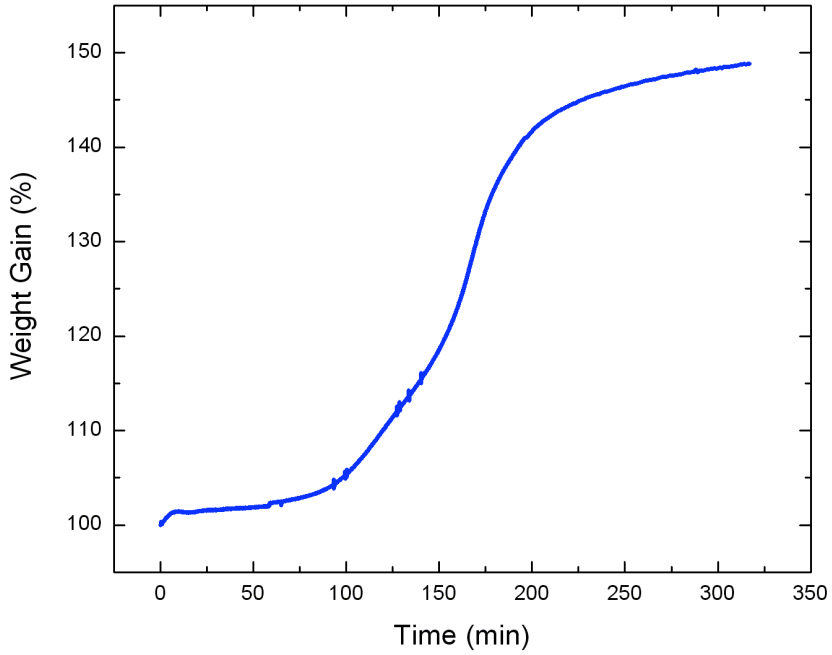

Figure 4.8: Weight gain due to oxidation of $ZrSi_2$ in oxygen (max. temperature =1000°C)

4.2.2 Aluminides: Ti_3Al, TiAl and $TiAl_3$

These three compounds can essentially be considered as Ti-Al alloys with 3:1, 1:1 and 1:3 atomic ratios of Ti:Al. According to previous study [135], it is known that Ti-Al intermetallics can be easily oxidized above 800°C, because a continuous Al_2O_3 protective scale is hard to form in a Ti-based alloy. Instead, a multi-layered structure composed of TiO_2 and Al_2O_3 is formed. However, the Ti-Al alloys become more oxidation resistant as the Al content increases. Al content of approximately 70 atomic percent, is sufficient to form a continuous layer of passivating Al_2O_3 [135-137]. This concentration is just about the composition of $TiAl_3$. In other words, Ti_3Al and TiAl should oxidize easily due to a relatively low aluminum content but $TiAl_3$ would be more resistant to oxidation.

Following these considerations, a heat treatment was designed for these alloys, which used air environment, a heating rate of 5°C/min and a maximum temperature of 900°C. This isothermal temperature was held for 2 hours. The results of their weight gains are compared in Figure 4.9.

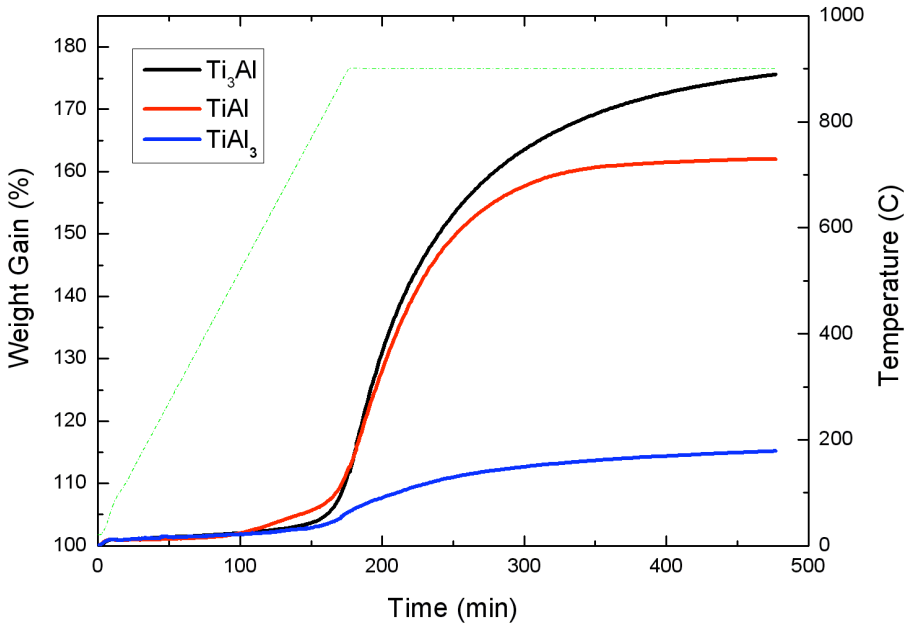

Figure 4.9: Oxidation kinetics of three types of Ti-Al intermetallics.

Sample powders were received with an average particle size of < 10 microns for Ti_3Al, and < 44 microns for TiAl and $TiAl_3$. Figure 4.8 clearly shows that in aluminides particle size is not the primary factor in determining their degree of oxidation, but aluminum content is. As the aluminum content increases in Ti-Al alloy, the degree of oxidation and weight gains decrease. From this observation, it can be concluded that Ti_3Al and TiAl were completely or almost completely oxidized under the chosen

experimental conditions. For Ti_3Al, the observed weight gain (75%) reaches theoretical value; for TiAl, its weight gain is 93% of the theoretically calculated weight gain. Finally, the poor oxidation kinetics of $TiAl_3$ under such experimental conditions implies that this compound is not suitable for further investigation.

4.2.3 Summary

In summary, Table 4.2 below categorizes the six active fillers into two families: disilicide and aluminide. By decreasing particle size via attrition milling ("Before" and "After" the milling process in the table), enhanced experimental weight gains for most of the fillers were observed. Milling breaks down fillers' average particle sizes to submicron- or nano-scale. However, Ti_3Al, is quite reactive in the particle size range of 1-10 μm, so milling is not needed. Heating conditions vary for different fillers due to their different oxidation properties; generally, higher oxidation temperature and higher oxygen partial pressure were used for more oxidation resistant materials, such as $ZrSi_2$. Disilicides show outstanding expansion potential with $\alpha^{EA}\beta^{EA}$ numbers larger than 2, however, this potential is not realized due to the incomplete oxidation at the relatively low processing temperature of this study. Based on their thermal properties, aluminides are promising by virtue of their ease in oxidation and the performance of alumina as an oxidation protective layer. However, as will be shown later, aluminide slurries are unstable and additional research is required to develop methods to stabilize their dispersion.

Table 4.2: Optimized oxidation conditions and results for the investigated active fillers.

	APS (μm)*		$\alpha^{EA}\beta^{EA}$	Theo. WG (%)**	Experimental WG		Oxidation Temp. (C)	Atmosphere
	Before	After			Before	After		
$TiSi_2$	--	0.3	2.58	92.3	~36	~60	800	Air
$CrSi_2$	~100	0.8	2.82	81.3	~2	~52	1000	O_2
$ZrSi_2$	~1	--	2.26	65.1	~50	--	1000	O_2
Ti_3Al	< 10	--	1.69	70.3	~75	--	900	Air
TiAl	~44	0.8	1.62	74.8	--	~62	900	Air
$TiAl_3$	~44	0.8	1.52	80.7	~14	~57	900	O_2

*APS: average particle size in micrometer. **WG: normalized weight gain in percentage.

4.3 Selection of Alloy Substrates

Coal-fired power plants running under ultra supercritical conditions—operating temperature 650°C and pressure 34.5 MPa, require outstanding properties for the utilized super alloys. They not only need to be mechanically strong enough to operate at higher temperature and pressure, but also have to withstand accelerated corrosion and oxidation from steam and coal ashes. After a careful literature survey, two representative alloys were chosen for this study: the Fe-based stainless steel super 304H, and the Ni-based super alloy Inconel 617. Their compositions are listed in Table 4.3 below.

Table 4.3: Nominal composition (in wt.%) of selected alloys.

	C	Cr	Ni	Mn	Si	Mo	Fe	Other 1	Other 2
Super 304H	0.10	18-20	8-10.5	2.0	0.75	-	Bal	S-0.03	N-0.1
SS 304	0.08	18-20	8-10.5	2.0	0.75	-	Bal	S-0.03	N-0.1
Inconel 617	0.08	21.6	53.6	0.1	0.1	9.5	0.9	Co-12.5	Al-1.2

Super 304H is a type of austenitic steel primarily used in the finishing stages of superheater and reheater tubing, where oxidation resistance and fireside corrosion become important in addition to creep strength. As for Inconel 617, its high chromium content enables it to serve in highly corrosive environments at the temperature of 650°C and higher, and it is especially good for coal-fired boiler tubing [138-141]. At 20°C, the linear coefficient of thermal expansion (CTE) are 17.3μm/m-°C and 11.6μm/m-°C for Super 304H and Inconel 617 respectively [142, 143].

Due to the availability and price of the super 304H alloy, an alternative material is actually used in experiments. The *AISI 304 Material Report (Austenitic Stainless Steel)*, from Startrite Designs Limited Co., concludes that alloy 304 is a standard 18Cr-8Ni stainless steel and 304H is a modification of 304, in which the carbon content is H—"higher" and controlled to a range of 0.04-0.10 to provide improved high temperature strength to parts exposed to temperatures above 800°F. As a result, SS 304 is considered to be a good substitute for this study since its price is much lower and its composition is also listed in Table 4.3.

Both types of alloy sheets were cut into small pieces of test coupons with unified dimensions of 30mm×10mm×1.2mm for dip coating. An Electro-Discharge Machining (EDM) tool was used to cut the material with a precise control of size without causing any warpage around edges. Each sample was then wet ground using deionized water with SiC sand papers up to 600-grit in order to create fresh surfaces, on which oxidation is minimized.

4.4 Control of Coating Thickness

4.4.1 Apparent Viscosity of Non-Newtonian Liquids

In Section 1.5.1, it was stated that the coating thickness needed to be controlled since it was an important factor in making crack free coatings. In Section 1.5.2, the Landau-Levich model was presented, which can be used to predict the thickness of dip-coated films. However, it only applies when the entrained slurry is Newtonian, therefore, it is crucial to understand the rheological nature of slurries used in this study, which consist of viscous preceramic polymer liquid (PHMS), organic solvent (n-Octane) and sub-micron scale solid particles ($TiSi_2$, etc.).

Rheological measurements were carried out on a rotary viscometer at room temperature to examine slurry's viscosity. The sample slurry studied in this part was a $ZrSi_2$-filled PHMS system diluted with n-Octane and its detailed composition can be found in Table 4.5, which is a representative composition for dip coating.

In testing, shear rate was increased in a stepwise manner as a function of time and every flat segment stands for a 30-second shear stress measurement under a constant shear rate (Figure 4.10.a), which would generate a data point in Figure 4.10.b. By re-plotting shear stress as a function of shear rate, its nonlinear increase was observed (Figure 4.10.c). Therefore, this type of slurries has shear-thinning property as opposed to Newtonian liquid, what Torrey [18] had assumed in a previous study. This phenomenon is largely attributed to the structural nature of PHMS, a linear polymer—when more and more molecular branches are aligned in the direction of applied stress, resistance from polymer molecules becomes less and less so that viscosity of the slurry is lowered.

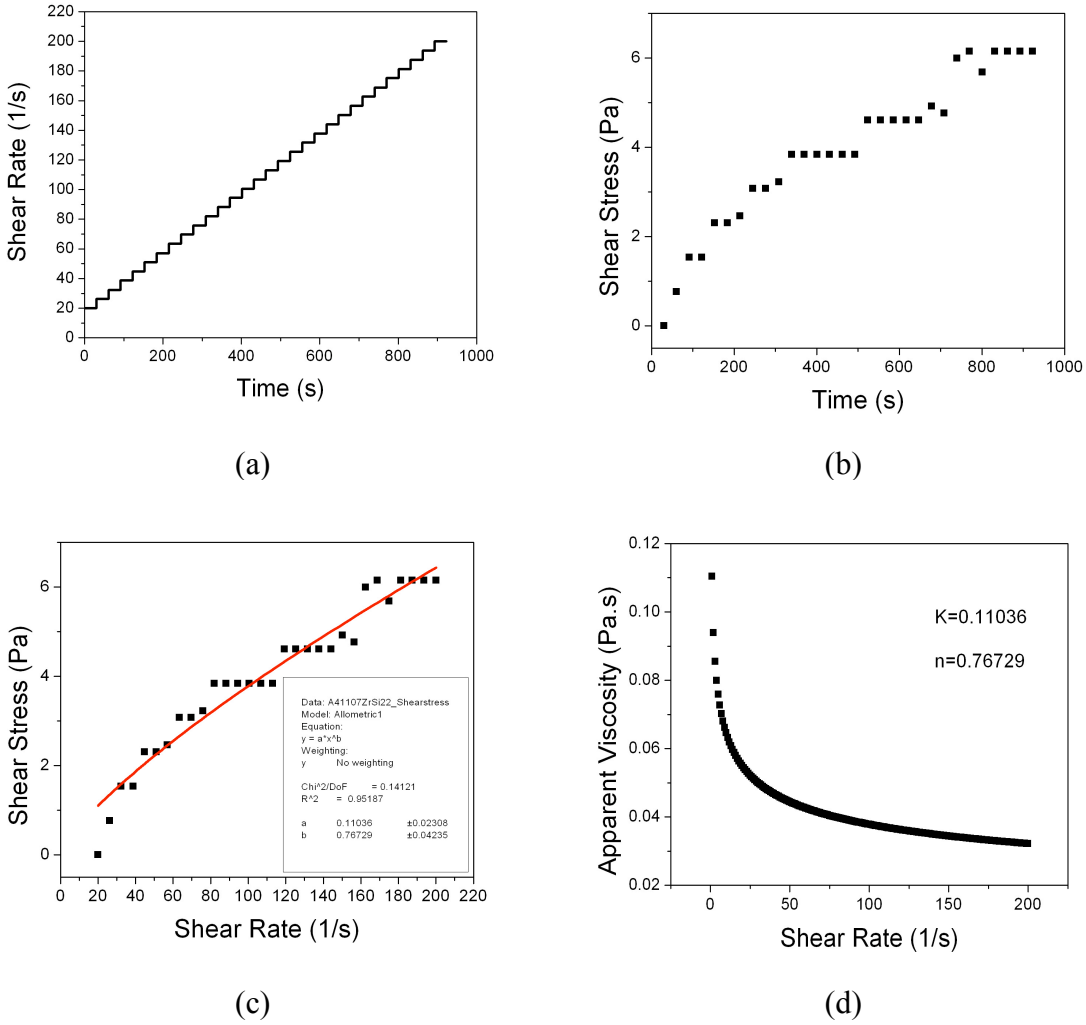

Figure 4.10: Viscometric measurements on $ZrSi_2$-filled PHMS (3:5) slurry. (a) shear rate as a function of time; (b) corresponding shear stress as a function of time; (c) a plot of shear stress vs. shear rate with a power law curve fitting superimposed (Equation 4.4.1); (d) calculated apparent viscosity as a function of shear rate (Equation 4.4.2).

The shear-thinning behavior of studied slurry can be described and fitted using a power law relationship. In Figure 4.10.c, the red curve indicates the fitting result using Equation 4.4.1.

$$\tau = K \cdot \dot{\gamma}^{n} \tag{4.4.1}$$

in which τ is shear stress, K is flow consistency index, $\dot{\gamma}$ is shear rate, and n is exponent. Best fit for the experimental data is obtained by $K = 0.11036$ and $n = 0.76729$. Apparent viscosity (μ_{app}) in power law model is defined by Equation 4.4.2 so that a numerical relation (Equation 4.4.3) between apparent viscosity and shear rate is established for this type of slurry and plotted in Figure 4.10.d.

$$\mu_{app} = K \cdot \dot{\gamma}^{n-1} \tag{4.4.2}$$

$$\mu_{app} = 0.11 \cdot \dot{\gamma}^{-0.23} \tag{4.4.3}$$

According to Equation 4.4.2, any liquid, whose exponent $n = 1$, is a Newtonian liquid with constant viscosity. However, when $n < 1$ as in this case, the liquid becomes non-Newtonian and shear thinning—viscosity decreases as shear rate increases (Figure 4.10.d).

4.4.2 Modification of Landau-Levich Model for Non-Newtonian Liquids

Due to the shear thinning nature of these slurries, there is no single viscosity value can be used to directly predict coating thickness in Landau-Levich model. In fact, there are similar models to work for non-Newtonian power law liquids [144, 145], but their complexity makes them difficult to be practically useful. Thus, the simplicity of Landau-Levich model motivated further investigation in seeking for some modification to adapt it to shear-thinning systems. Apparently, to find correct viscosity values that correspond to different withdrawal speeds is the key issue.

One of the assumptions made in Landau-Levich equation is that when vertically dragging a plate out of liquid at a constant speed, gravity, surface tension and viscous

force of the liquid are all dominant in the transition region near stagnation point (Figure 4.11). Stagnation point is a point on the entrained liquid profile with surface speed zero and divides the movement of the liquid into two directions: above here, liquid moves upwards due to the viscous force and surface tension; below here, liquid is too "heavy" and goes back to the bath.

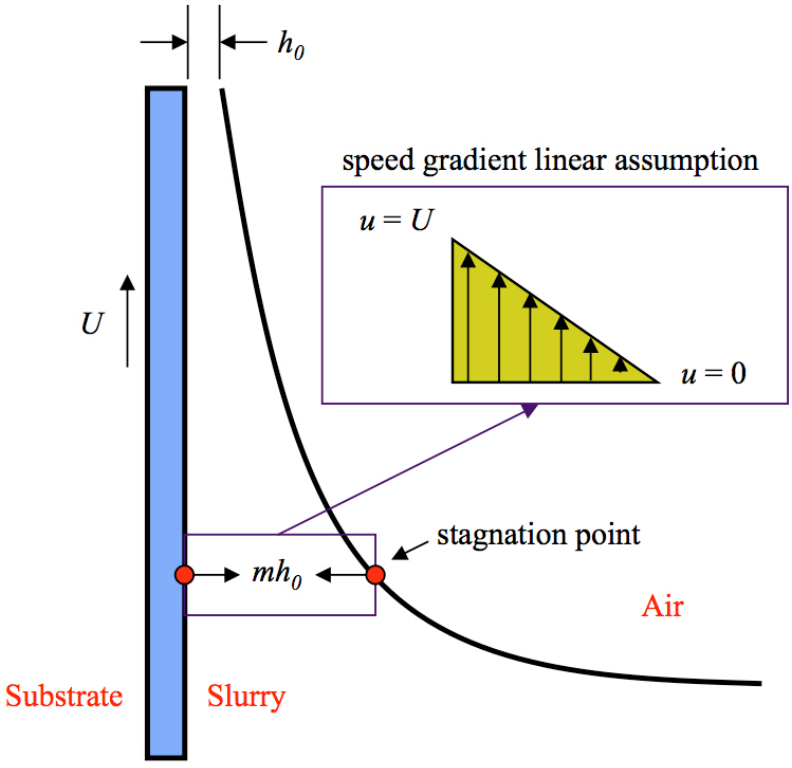

Figure 4.11: Profile of a liquid film adhering to a vertical moving surface.

Drawing an imaginary line (essentially a plane in 3D) from the stagnation point normal to the substrate surface, it divides the body of entrained liquid into two parts, above which it is being adhered to form a film on the substrate. This line is defined as

"stagnation line" here. We assume that the speed decreases linearly from maximum (at the substrate/film interface) to zero (at the film/air interface) so that a single shear rate can be obtained on the stagnation line. This is comparable to the diametric direction of a cylindrical rotor-cup type of viscometer setup. The velocity gradient of the slurry in the gap between rotor and cup is exactly the same as the assumed profile on the stagnation line. Therefore, shear rate and viscosity measurement in these two scenarios can be correlated with each other. If liquid's shear rate around stagnation line is known, its apparent viscosity value can be calculated by making use of Equation 4.4.3, whose form was experimentally determined using the same slurry with the viscometer.

To proceed further, a few assumptions need to be made. The slurry, a particle suspension, is assumed to be homogeneous throughout the course of dip coating. The first layer of slurry is assumed to attach to the substrate perfectly and it rises at the same speed as the plate—withdrawal speed U. Speed at stagnation point drops to zero in a linear trend. The thickness of entrained slurry at the stagnation line is mh_0 (m, a numerical factor), with $m > 1$ due to the meniscus shape. h_0 is the uniform film thickness far away from transition region. Finally, it is assumed that there is no solvent evaporation during dip coating. With all these conditions, shear rate on the stagnation line can be expressed as follows,

$$\dot{\gamma} = \frac{\partial v_x}{\partial y} = \frac{U - 0}{m \cdot h_0} = \frac{U}{m \cdot h_0} \tag{4.4.4}$$

In an analysis of high-capillary-number Newtonian liquids, Groenveld [117] used $m = 3$ as the numerical factor to study Landau-Levich model. Slurry studied in this research has relatively small capillary number (Section 4.4.3) so that it is fair to assume

this numerical factor to be between 1 and 3. For simplicity, $m = 2$ is used in the following calculation and Equation 4.4.4 is transformed to

$$\dot{\gamma} = \frac{\partial v_x}{\partial y} = \frac{U}{2h_0} \tag{4.4.5}$$

The investigated withdrawal speed was in the range of 100-1000 mm/min. To obtain coating's "wet" thickness in green state, h_0, following rationale has been made.

Figure 4.12 demonstrates the evolution of coating thickness from "wet" stage to "dry" stage and then to crosslinked stage.

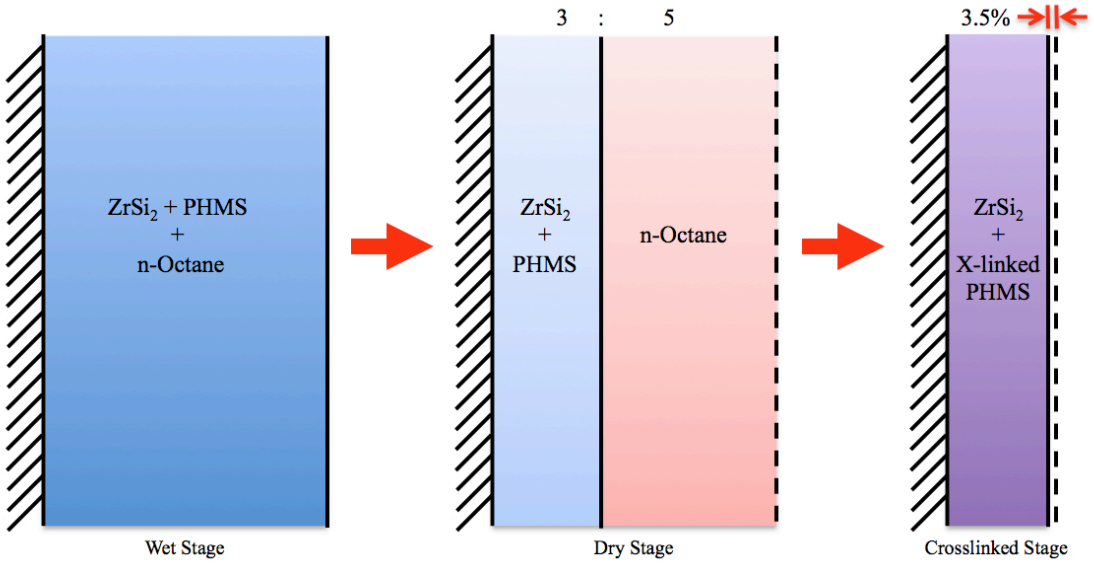

Figure 4.12: Schematic of coating thickness evolution after dip coating.

After being coated onto the substrate, film is physically constrained by the substrate geometry, thus any evaporation or shrinkage is only considered in the thickness direction. Film in wet stage keeps its original composition and thickness, namely h_0.

Since volume ratio between ($ZrSi_2$ + PHMS) and n-Octane is 3 : 5, coating thickness in dry stage shrinks to $3/8$ (37.5%) of its wet thickness when n-Octane solvent evaporates in air at room temperature, leaving dense ($ZrSi_2$ + PHMS). Then temperature is brought up to 150°C for crosslinking, during which PHMS has another 5% linear shrinkage (Figure 4.2) while filler particles are not significantly oxidized. Filler particles take up 30% volume fraction in the ($ZrSi_2$ + PHMS) mixture so that coating thickness reduction is 3.5% (see below, A is coating area) from dry stage to crosslinked stage.

$$\Delta h_{dry\to x-linked} = \frac{\left[A\cdot 30\% + A\cdot 70\%\cdot(1-5\%)\right]_{x-linked} - \left[A\cdot 100\%\right]_{dry}}{\left[A\cdot 100\%\right]_{dry}} = 0.965 - 1 = 0.035 \qquad (4.4.6)$$

Define that h_{CL} is the coating thickness after PHMS crosslinking at 150°C, a parameter that can be experimentally measured using either optical or stylus profilometer, since coating after crosslinking has become rigid enough to withstand scratches from stylus tip. Consequently, the following equation can be obtained to relate the cross-linked thickness to the wet thickness:

$$h_{CL} = h_0(comp.)\times 37.5\%\times 96.5\% = 0.362\cdot h_0(comp.) \qquad (4.4.7)$$

in which $h_0(comp.)$ is the wet coating thickness derived from the above compositional rationale and is based on experimental evidence. This number can be applied back into Equation (4.4.5) so that shear rate ($\dot{\gamma}$) and corresponding slurry viscosity (μ_{app}) can be calculated respectively. Once surface tension and slurry density are known, coating thickness predicted by Landau-Levich model can be obtained (Equation 4.4.8).

$$\mu_{app} = 0.11\cdot\left(\frac{U}{2\cdot\frac{h_{CL}}{0.362}}\right)^{-0.23} = 0.163\cdot\left(\frac{U}{h_{CL}}\right)^{-0.23} \qquad (4.4.8)$$

4.4.3 Experimental Results on Coating Thickness Control

Surface tension (σ) of the slurry was determined by a pendant drop method to be 35 mN/m for a volume ratio ($ZrSi_2$ + PHMS) : n-Octane = 3 : 5 type of slurry. And slurry density (ρ) was found to be 1.59 g/cc using the rule of mixture.

Four withdrawal speeds were used in the 100-1000 mm/min range: 100, 300, 700 and 1000 mm/min, resulting in four different thicknesses. Coating thickness of crosslinked samples were thus measured using a stylus profilometer and multiple measurements were performed on each sample to get average values. Rest of the calculation followed the method discussed in the previous section. Table 4.4 summarizes the results.

Table 4.4: Parameters used in the modification of Landau-Levich model with four withdrawal speeds ((ZrSi2 + PHMS) + n-Octane slurry).

U (mm/min)	100	300	700	1000
h_{CL} (μm) [Measured]	10.3	14.6	19.1	22.4
h_0*(comp.)* (μm) [Calculated using Eqn. 4.4.7]	28.9	40.9	53.6	62.8
$\dot{\gamma}$ (s^{-1}) [Calculated using Eqn. 4.4.5]	28.9	61.2	108.8	132.7
μ_{app} (Pa.s) [Calculated using Eqn. 4.4.3]	0.0505	0.0424	0.0371	0.0354
h_0*(L-L)* (μm) [Calculated using Eqn. 1.5.9]	25.4	47.0	75.6	92.9

The value of capillary number, $\left(\frac{\mu U}{\sigma}\right)$, determines if it is a negligible factor in the Landau-Levich equation and which form of the equation should be used (1.5.9 or 1.5.10). Consider the case that withdrawal speed is 100 mm/min, surface tension is 35 mN/m and apparent viscosity is 0.0505, capillary number is calculated to be 0.0024, which is << 1, hence Equation 1.5.9 should be applied. Also note from Figure 4.10.d that slurry's viscosity falls into a small range with a less than two-fold increase in the withdrawal speed range of 100-1000 mm/min.

In Figure 4.13, the measured cross-linked coating thickness (h_{CL}), the calculated "wet" thickness ($h_{0(comp.)}$), and the estimated "wet" thickness by Landau-Levich model ($h_{0(L\text{-}L)}$) are plotted as a function of the withdrawal speed. The Landau-Levich model predicts the coating thickness well at low withdrawal speeds but overestimates the coating thickness at high withdrawal speeds.

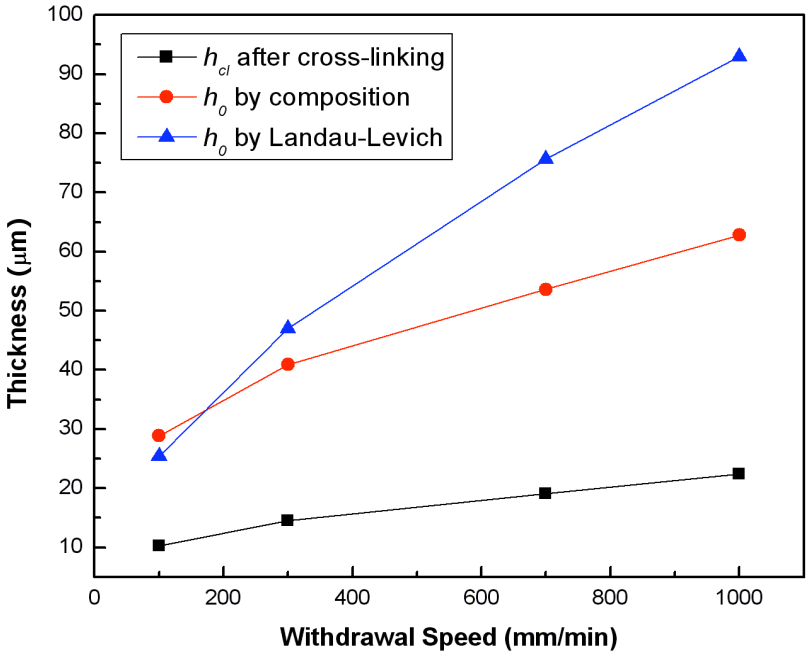

Figure 4.13: Comparison of wet coating thicknesses derived from compositional calculation and Landau-Levich prediction.

The overestimation of coating thickness by Landau-Levich model may be largely attributed to insufficient surface tension to stop extra slurry from draining down the plate for the case in which the film is dried vertically. In reality, volatile solvent evaporates quickly during the process of dip coating. If liquid film is thin enough, surface tension and viscous force are strong enough to hold slurry on the plate against gravity until it dries, resulting in no loss in adhered material. This drying process may take only seconds. However, when liquid film gets thicker as a function of increasing withdrawal speed, it takes much more time to complete evaporation of the solvent; surface tension is kept nearly the same, however, much heavier coating layer is adhered. Therefore, there is

enough time for extra slurry to slowly flow down the plate due to gravity and form a meniscus bump region at the bottom part. Then, in bulk part of the coating area, it reaches equilibrium state with reduced coating thickness that is measured in experiments.

One solution to this problem is to flip the substrate plate to a horizontal position immediately after it has been completely pulled out of the slurry. This allows for uniform coating thickness since no viscous liquid drains due to gravity and evaporation of the solvent in the horizontal configuration with coating material conserved. Experiments were carried out accordingly using the same slurry. The results are shown in Figure 4.14. As can be seen, the fit between the measured and the calculated "wet" thicknesses is much better for horizontal drying. For example, at the withdrawal speed of 700 mm/min, the gap between $h_0(comp.)$ and $h_0(L\text{-}L)$ is reduced in half—from ~22 μm to ~11 μm for the case of horizontal drying as opposed to vertical drying. Further improvements are still needed in this developing model to accurately predict coating thickness.

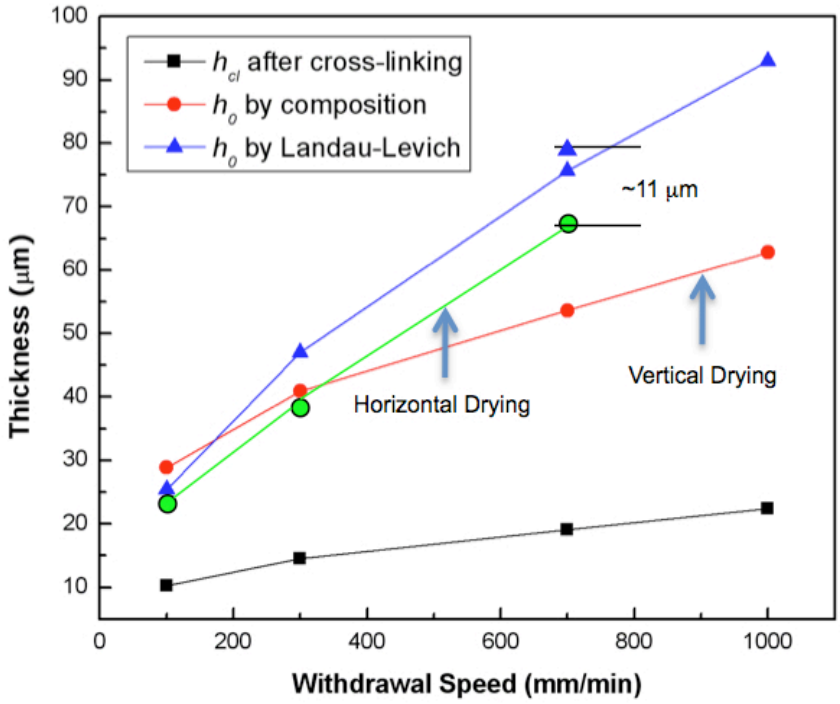

Figure 4.14: Comparison of horizontal drying and vertical drying in terms of improving coating thickness agreement with Landau-Levich model.

4.5 Optimized Processing Procedure of Coatings

After the first round of thermal analysis on all six active fillers, $TiAl_3$ was excluded due to its low reactivity in the interested temperature range. Rest five active fillers—$TiSi_2$, $CrSi_2$, $ZrSi_2$, Ti_3Al and TiAl—were chosen as expansion agent candidates for the next step. Torrey [18] has established an optimized processing procedure for the $TiSi_2$-filled PHMS system and it was used in preparing various filler slurries for this research (Figure 4.15).

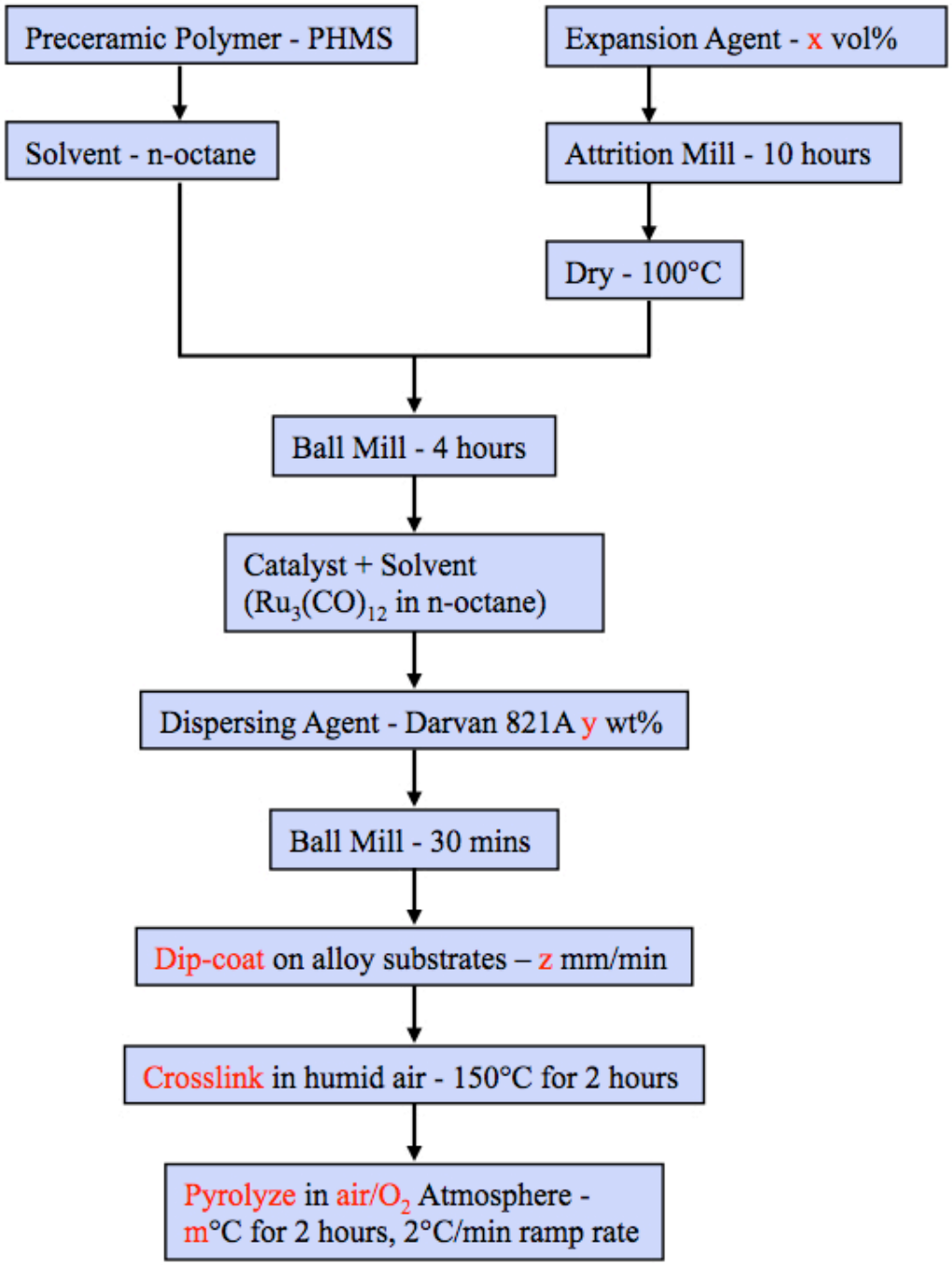

Figure 4.15: Flow chart of the processing of polymer derived ceramic matrix composite coatings.

Active fillers were attrition milled in isopropyl alcohol for 10 hours, dried at relatively low temperature (~100°C), and ground back to powders using mortar and pestle. Then, fillers were mixed with the required amount of PHMS and half of the required n-Octane solvent. The volume fraction of active fillers in filler/polymer mixture, which was required for zero-shrinkage pyrolysis, was calculated in Table 4.1; generally, disilicides were 30%, while aluminides were 40%. By virtue of its low boiling point (126°C) and low viscosity (~1 centiPoise), n-Octane was added to dilute the mixture to a suitable viscosity range for dip coating. A volume ratio of 3 : 5 between (filler + PHMS) and n-Octane was used for preparing all five systems. Detailed composition information regarding each type of slurry is summarized in Table 4.5.

Table 4.5: Slurry Composition for 20ml Samples.

Fillers	Vol% Fillers	Wt. Filler (g)	Wt. Polymer (g)	Wt. Ru (mg)	Vol. n-Octane (ml)	Vol. Ratio (slurry : n-Octane)
$TiSi_2$	30	9.05	5.25	2.63	12.50	3 : 5
$CrSi_2$	30	11.05	5.25	2.63	12.50	3 : 5
$ZrSi_2$	30	10.98	5.25	2.63	12.50	3 : 5
Ti_3Al	40	9.30	4.50	2.25	12.50	3 : 5
TiAl	40	11.40	4.50	2.25	12.50	3 : 5

The slurry was then ball-milled for 4 hours in order to mix all the reactants well and remove agglomerates from filler particles. 0.05 wt% of $Ru_3(CO)_{12}$ catalyst (to PHMS) was dissolved in the other half of n-Octane, and the solution was added to the slurry, which would be ball-milled for another 30 minutes or so prior to dip coating.

It was observed that the aluminides could not be properly dispersed in the polymeric slurry. Majority of the filler particles settled down quickly, resulting in an

inhomogeneous slurry. Therefore, dispersing agents were considered in order to make slurry suspension stable for a longer period of time. A common dispersing agent—Darvan 821A, an ammonium polyacrylate solution, was added (0.5-5 wt%) into Ti_3Al and TiAl filled slurries. Its working mechanism is to provide each filler particle with the same type of charge on their surfaces, so that the repulsive force would keep particles away from each other and the slurry is thus stably dispersed. Darvan 821A was gradually added to the slurry with 0.5 wt% increment up to 5 wt %, but in no case the dispersion was stable for more than one minute. This is too short a time for practically handling the slurry and making good-quality coatings. Due to this reason, the two aluminides—Ti_3Al and TiAl—were also eliminated from further research in this study.

A mechanical testing frame, Instron, was used to dip coat slurries onto alloy substrates (600-grit surface finish), either SS304 or Inconel 617. Dip coating took place under ambient conditions. Typical withdrawal speeds under investigation were 100, 300, 700 and 1000 mm/min respectively. Due to a long travelling distance (> 20 mm) for the Instron crossbar, it was assumed to move at a constant and accurate speed as programmed, although it would have a jump start from speed zero and creates a very limited region of non-uniform thickness in the beginning (< 1 mm). Several sets of samples were dip-coated with the same parameters at the same time.

Pyrolysis was performed in a tube furnace (CM-1200, CM Furnace Inc., Bloomfield, NJ, USA). Humid air was used for polymer's *in situ* crosslinking in the tube. The temperature profile had a 2°C/min ramp rate for both heating and cooling processes. Temperature was held constant at 150°C for 2 hours for crosslinking, and at 800°C for another 2 hours for the pyrolysis of PHMS and oxidation of active fillers. Pyrolysis

atmosphere includes air or pure oxygen at 1-2 Standard Cubic Feet per Hour (SCFH). This heating profile ensured that the pyrolytic ceramic matrix remained amorphous but fully converted, and filler particles could be highly oxidized.

4.6 Summary

This chapter started with criteria and strategies in selecting the right preceramic polymer and active filler combinations. PHMS was selected primarily due to its simplicity in processing, for instance, in-situ crosslinking ability, and its intermediate pyrolysis temperature (800°C) with desired SiCO amorphous structure. Among the six expansion agent candidates, all three aluminides were eventually excluded from the list due to reactivity or dispersing problems. Therefore, the focus of this research is on disilicide filled systems.

As for the processing of ceramic coatings, Landau-Levich model was modified to control coating thickness for non-Newtonian liquids, based on apparent viscosity measurements on the shear-thinning slurries used in this research. It was found that horizontal drying of the "wet" coating lead to a reasonable agreement in coating thickness between experimental data and the prediction from modified Landau-Levich model.

CHAPTER V

CHARACTERIZATION OF COMPOSITE COATINGS

5.1 Physical Characterization

This section includes results on the physical characterization of various coating systems. Surface morphology was studied using both optical profiler and SEM. Phase evolution and microstructural evolution of the coatings were examined from crosslinking stage (150°C) to pyrolysis stage (800-1400°C). EDS analysis on the interfacial composition of the coatings revealed the existence of direct chemical bonds between coating and substrate due to the formation of a TGO diffusion layer.

5.1.1 Coating Surface Morphology

The "green" coating soon after the completion of dip coating process is composed of filler particles and preceramic polymer molecules, since the solvent n-Octane evaporates rather quickly. At this stage, its surface morphology cannot be analyzed by regular methods that usually are destructive or contact style, because it is still not structurally stable without intensive polymer crosslinking. Therefore, an optical profiler for 2-D surface mapping and coating thickness measurement was used for this purpose. The information that can be acquired here is important in studying the development of shrinkage and porosity in the coating.

Experiments were carried out on a WYKO NT3300 white-light-interferometer profiling system at Washington Technology Center. Figure 5.1 shows a set of 30 vol%

$TiSi_2$-filled PHMS system on Inconel 617 substrates. Each sample was crosslinked at 150°C first, then a razor blade was used to artificially introduce a transverse (with respect to the dip-coating direction) crack in the middle of the coating area, so that the substrate can be visibly exposed. Profilometric scans were targeted in an area of 7.5 mm×2.5 mm around the crack. In the following graphs, the top parts with nearly uniform colors were the metal substrate, which were taken as height zero references assuming they were flat. Therefore, 2-D contour maps of the coatings were generated with a spectrum of colors, representing the relative height at each pixel.

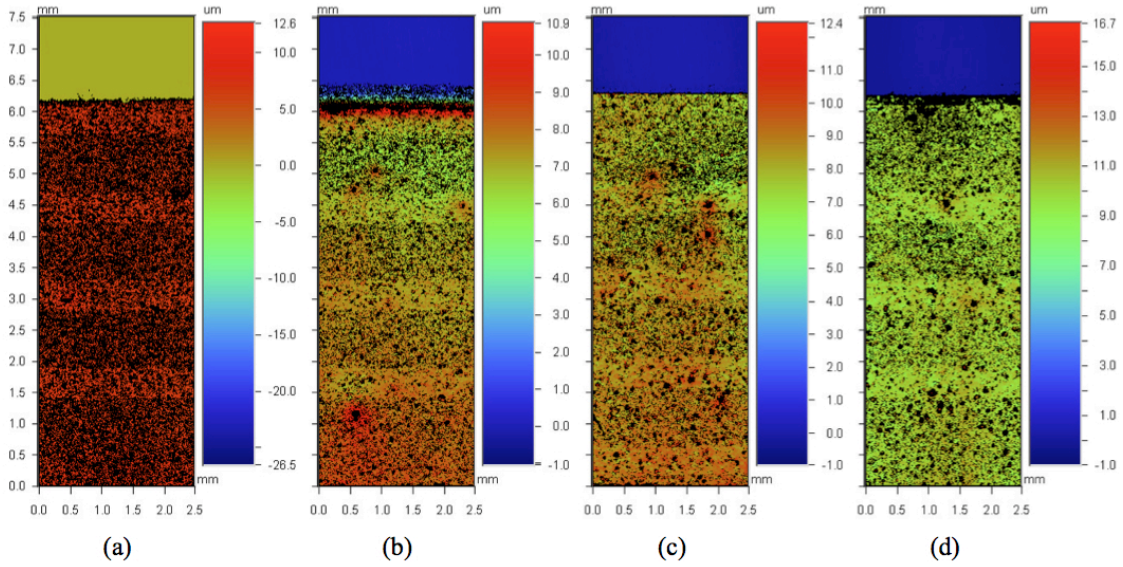

Figure 5.1: 30 vol% $TiSi_2$ + PHMS average coating thickness (crosslinking) by various withdrawal speeds. (a) 300 mm/min, 7.1 μm; (a) 500 mm/min, 8.5 μm; (a) 750 mm/min, 9.1 μm; (a) 1000 mm/min, 10.3 μm.

It can be observed that coating thickness increases as a function of withdrawal speed, which is in accordance with the modified Landau-Levich model presented in Section4.4. From 300 to 1000 mm/min, the average coating thickness increases from 7.1 to 10.3 μm. In general, coatings have uniform thickness as seen in their narrow color ranges; for samples withdrawn at 500 and 750 mm/min, thickness slightly increases from top to bottom, which is caused by gravity and can be widely observed in coatings prepared by similar methods. Their average surface roughness was arithmetically calculated to be ~3.2 μm—this is strongly affected by the particles in the coating. Moreover, in Figure 5.1, the black areas in the coatings are very likely to be the porosity formed during polymer crosslinking. Using a graphic analysis method (*ImageJ*, developed by National Institutes of Health), the coatings can be divided into a binary graph (Figure 5.2), so that the black phase representing pores can be counted individually and analyzed for their area fraction. Table 5.1 summarizes the average pore size and porosity data for coatings of different thicknesses.

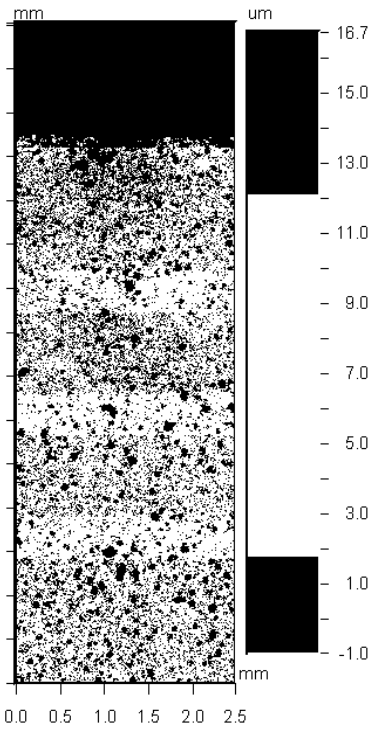

Figure 5.2: A binary graph of the 30 vol% $TiSi_2$ + PHMS coating (thickness: 10.3 μm).

Table 5.1: Coating thickness, roughness, pore size and volume porosity as a function of withdrawal speed in the 30 vol% $TiSi_2$ + PHMS coating system.

Withdrawal Speed (mm/min)	300	500	750	1000
Average Coating Thickness (μm)	7.1	8.5	9.1	10.3
Roughness Average (R_a) (μm)	3.32	2.60	2.91	3.61
Average Pore Size—Area (μm)	2.3	1.6	1.7	1.6
Average Pore Size—Diameter (μm)	0.86	0.71	0.74	0.71
2-D Porosity (%)	34.9	31.4	30.3	29.7
3-D Porosity (%)	20.6	17.6	16.7	16.2

Area fraction of the porosity is calculated to be constantly around 31.6%, which corresponds to 17.8% in volume, assuming pores are isotropic. This number is much smaller than Torrey's analysis [18], which assumed the volume fraction of porosity in the

same system after crosslinking was nearly 60% while polymer matrix took only 10%. Considering the linear shrinkage of PHMS is only 5% up to crosslinking, it is speculated that 60% porosity for such a system has been overestimated and porosity obtained from this study (17.8%) is more realistic. Furthermore, assuming that pores in the coatings have spherical shape, average pore size can be determined in diameter: 0.76 μm—this result is in good agreement with Torrey's conclusion of pore size in the size region of 0.10-1.0 μm.

It is important to note that pores, represented by the black areas in the 2-D contour mapping, didn't go through the whole thickness to the substrate surface. Instead, there was just not enough light reflected off those regions to form a light interference pattern, which was primarily due to coating's surface roughness.

5.1.2 Phase Evolution in Composite Coatings

Phase evolution in the 30 vol% $ZrSi_2$-filled PHMS system was studied using XRD as a function of pyrolysis temperature. This study was conducted on pyrolytic powders that were pyrolyzed and then ground to small size. The investigated temperatures include 100, 400, 600, 800, 1000, 1200 and 1400°C as shown in Figure 5.3.

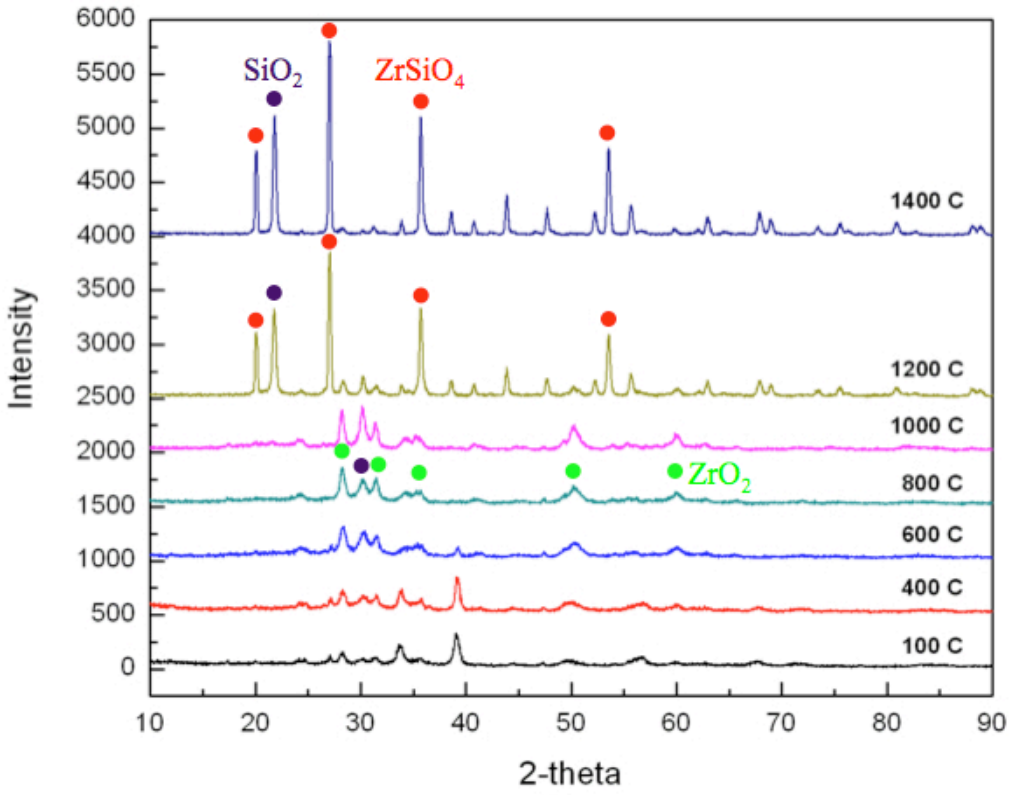

Figure 5.3: XRD of 30 vol% $ZrSi_2$ + PHMS system crosslinked at 100°C and pyrolyzed at 200° intervals from 400°C to 1400°C in air.

The system starts with only $ZrSi_2$ peaks below 400°C, because during the conversion from polymer to ceramic, PHMS remains amorphous until 1600°C [18]. When it reaches 600°C and above, PHMS is getting close to the completion of its pyrolysis, while $ZrSi_2$ particles start to be oxidized, therefore, $ZrSi_2$ peaks disappear but ZrO_2 (baddeleyite, monoclinic) and SiO_2 (stishovite, tetragonal) peaks appear at 800°C. The formation of ZrO_2 phase at this temperature would largely improve coating's stability and oxidation resistance. Between 600°C and 1000°C, the peaks of these two oxides

grow stronger, which implies the continuous oxidation of filler particles. However, when temperature is 1200°C and above, the monoclinic ZrO_2 phase reacts with surrounding SiO_2 phase to form a new tetragonal zircon, $ZrSiO_4$ phase. SiO_2 cristobalite (high temperature polymorph of quartz) phase also appears at this temperature. Since it is known that ceramic matrix derived from PHMS is still amorphous, this cristobalite phase must be the SiO_2 originally from $ZrSi_2$ particles, therefore, up to this point, the atomic ratio between zircon and cristobalite is 1 : 1. Even at a temperature as high as 1400°C, there is still evidence of residual $ZrSi_2$, indicating that filler particles were only partially oxidized. In summary, if the coating system is pyrolyzed at 800°C, the ceramic composite consists of crystalline filler phases (ZrO_2, SiO_2 and $ZrSi_2$) and amorphous SiCO matrix network.

5.1.3 Microstructural Evolution of Coatings

SEM was used to investigate the microstructure characteristics of different coating systems. The microstructural evolution of PHMS coating systems as a function of pyrolysis temperature was observed as well. This part of study gives a good insight into the homogeneity and the bonding condition of the coatings, which are important factors in evaluating coating's quality and performance.

Figure 5.4 and 5.5 show the ceramic-metal interface of $TiSi_2$-filled and $CrSi_2$-filled coating systems respectively. They were both pyrolyzed at 800°C in air. In both cases, the coating layer was well bonded to the substrate as a 0.5-1 μm thick diffusion layer can be observed at the ceramic-metal interface (Figure 5.6). EDS analysis shows an oxygen concentration jump in the diffusion layer, which is made of thermally grown

oxides with metal elements, such as Cr, diffuse in from one end and Si from the other. This is an evidence for the formation of direct chemical bonds between the two. At pyrolysis temperature of 800°C, no delamination or severe cracking in the ceramic coating has been observed in either material system. Filler particles were largely oxidized, while some of them left un-reacted cores inside as seen in a solid color comparing with lighter color outer shells. Very low close porosity exists in these coatings.

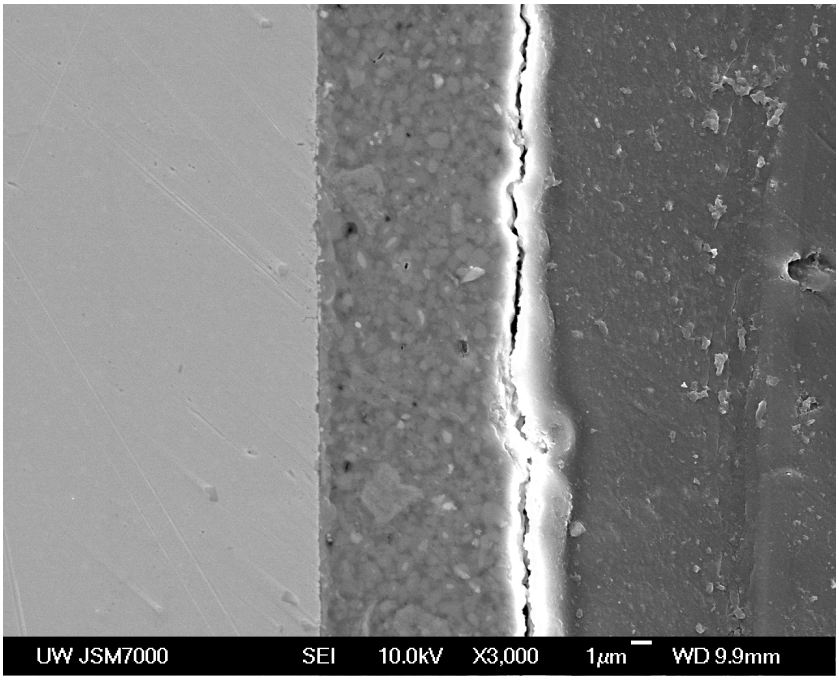

Figure 5.4 Cross-sectional view of the 30 vol% $TiSi_2$-filled PHMS coating system, pyrolyzed at 800°C in air.

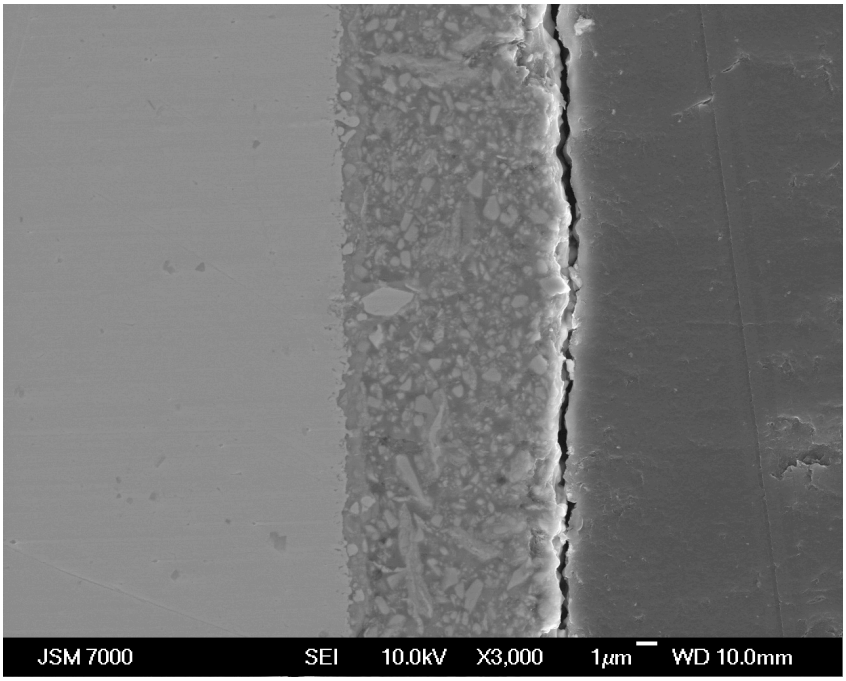

Figure 5.5: Cross-sectional view of the 30 vol% $CrSi_2$-filled PHMS coating system, pyrolyzed at 800°C in air.

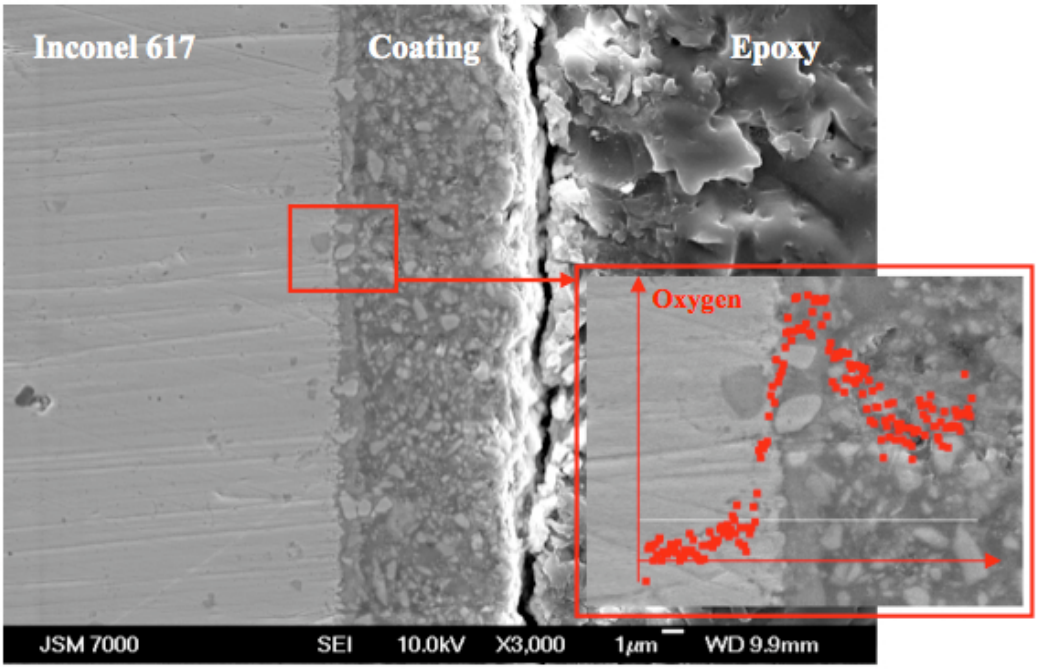

Figure 5.6: EDS study at the interface of 30 vol% $CrSi_2$-filled PHMS coating system, illustrating the formation of TGO diffusion layer.

Microstructural evolution of an example coating system (30 vol% $ZrSi_2$-filled PHMS) is demonstrated in Figure 5.7—5.10. Samples were prepared with different thickness by varying withdrawal speed during dip coating (100-1000 mm/min) and then pyrolyzed at 150, 600, 800 and 1000°C. In each of the following cross-section view, dark region on the left is epoxy applied onto the coating surface and light region is stainless steel 304 substrate. In Figure 5.7, samples were crosslinked, however, coating layer had been pulled off the substrate due to the shrinkage from epoxy, which indicated that molecular branches of PHMS reacted with each other and wrapped around filler particles forming a two-phase composite, but the chemical bonding between coating layer and substrate had not sufficiently formed. When pyrolysis temperature reached 600°C, the situation changed: as shown in Figure 5.8, coating layer bonded to the substrate, but no TGO diffusion layer could be observed at the interface. During this step of heat treatment, the coating layer shrank significantly in the thickness direction due to polymer pyrolysis. For 800°C pyrolyzed samples (Figure 5.9), the diffusion layer was present with a thickness of roughly 0.5 μm. This layer grew as temperature increased, since its thickness becomes about 1.5 to 2 μm at 1000°C (Figure 5.10). In general, porosity in the coating decreased drastically as densification process took place. These pores were mainly from the stacking gaps between filler particles, where polymer molecules could not fill up all the space. Throughout the whole temperature range of 150-1000°C, $ZrSi_2$ particles remained in two colors: light (oxides) and dark (disilicides), implying that they were only partially oxidized up to 1000°C, therefore, their function as expansion agents was limited.

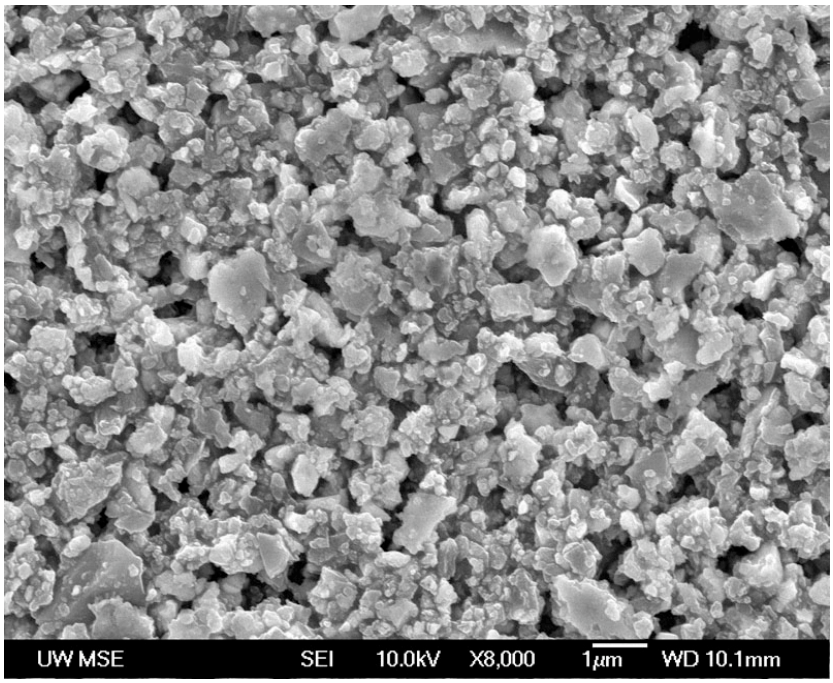

(a)

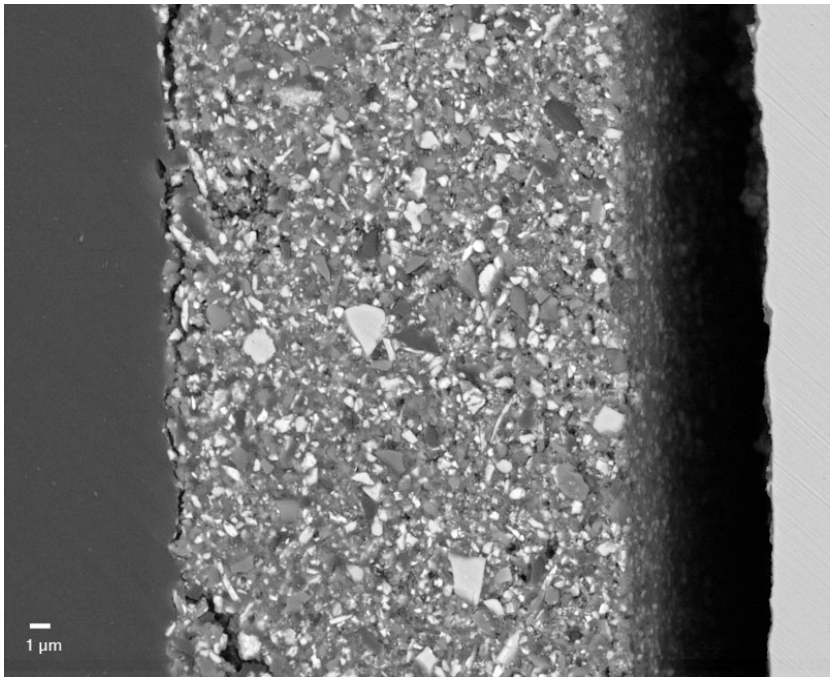

(b)

Figure 5.7: SEM image of microstructure of 30 vol% $ZrSi_2$-filled PHMS coating pyrolyzed in air at 150℃: (a) top view, (b) cross-section.

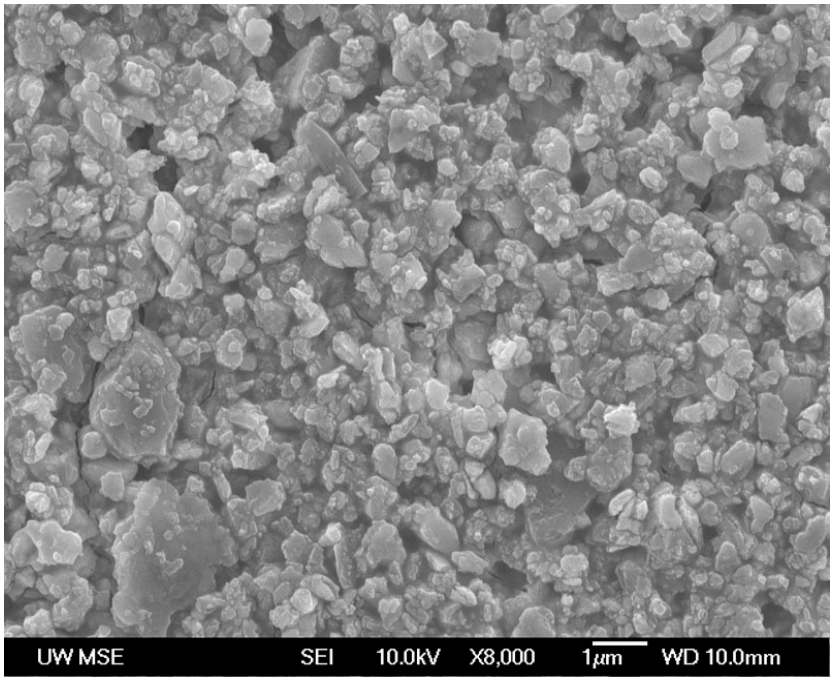

(a)

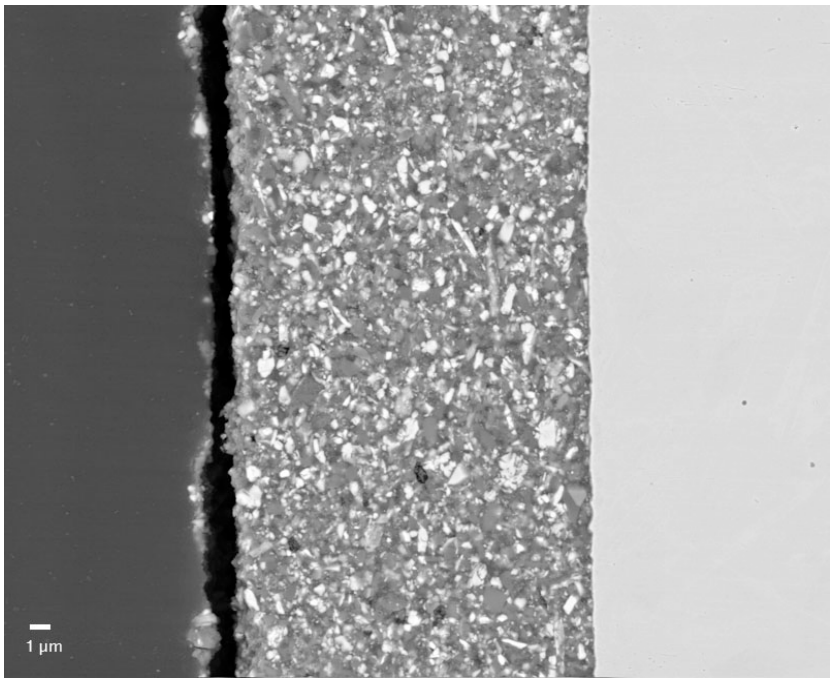

(b)

Figure 5.8: SEM image of microstructure of 30 vol% $ZrSi_2$-filled PHMS coating pyrolyzed in air at 600° C: (a) top view, (b) cross-section.

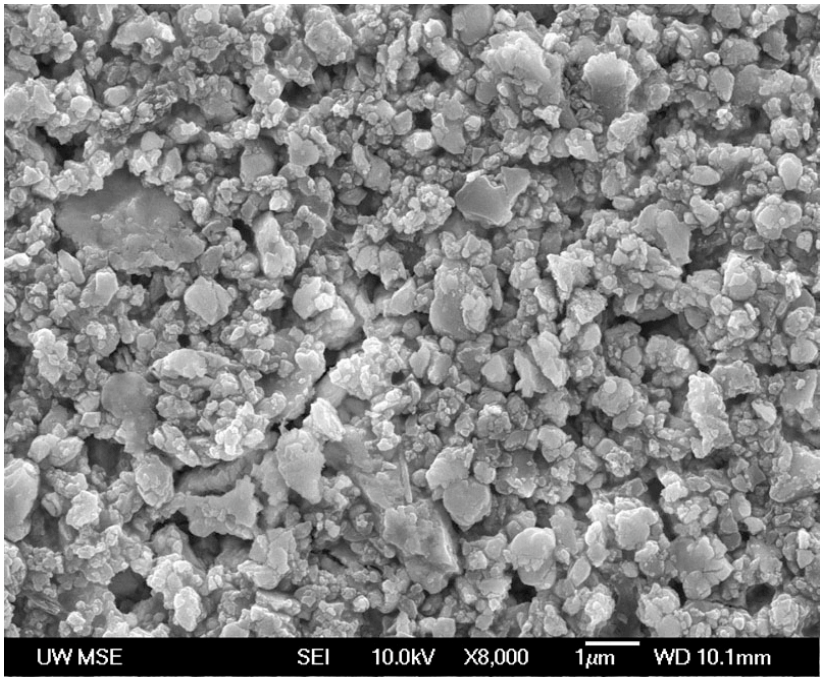

(a)

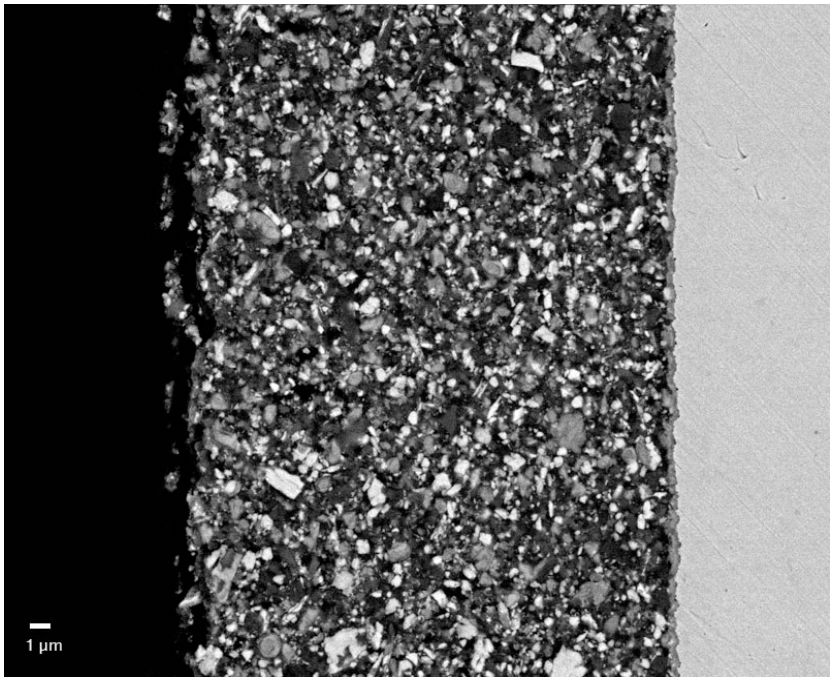

(b)

Figure 5.9: SEM image of microstructure of 30 vol% $ZrSi_2$-filled PHMS coating pyrolyzed in air at 800° C: (a) top view, (b) cross-section.

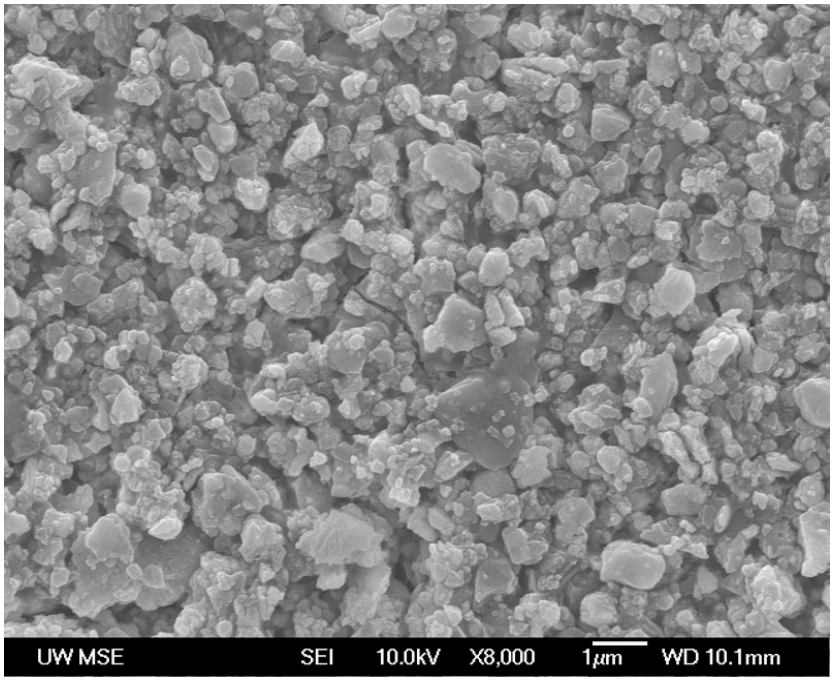

(a)

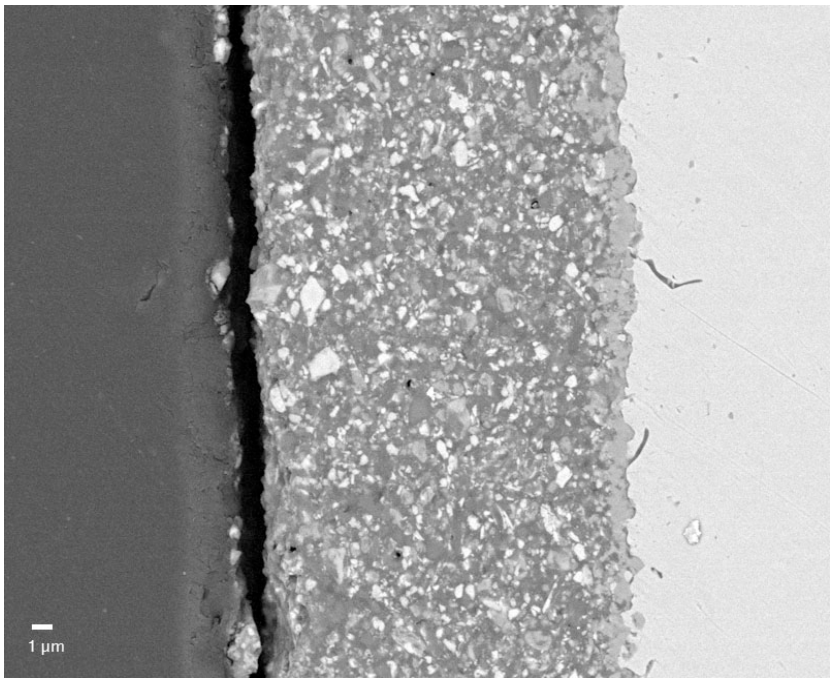

(b)

Figure 5.10: SEM image of microstructure of 30 vol% $ZrSi_2$-filled PHMS coating pyrolyzed in air at 1000°C: (a) top view, (b) cross-section.

SEM analysis also showed that it was desirable to control the TGO diffusion layer at a reasonable thickness, otherwise the top surface of metal substrates might lose their integrity and properties due to intensive elemental diffusion at higher temperatures or prolonged pyrolysis time (Figure 5.11. Note: light region on the left is steel substrate). As shown at 1000°C, part of the coating was either partially or completely debonded from the substrate. The diffusion layer appears to have stronger bonds with the composite coating rather than the steel substrate. Comparing with the result of EDS analysis on $CrSi_2$-filled PHMS coating system, Figure 5.12 demonstrates that in $ZrSi_2$-filled PHMS coating system the diffusion layer includes Cr from the substrate, Si and O from the ceramic matrix or the environment. Based on these results, there is an optimal pyrolysis temperature (around 800°C) for an optimal level of bonding between the (active filler + PHMS) coating and the metal substrate.

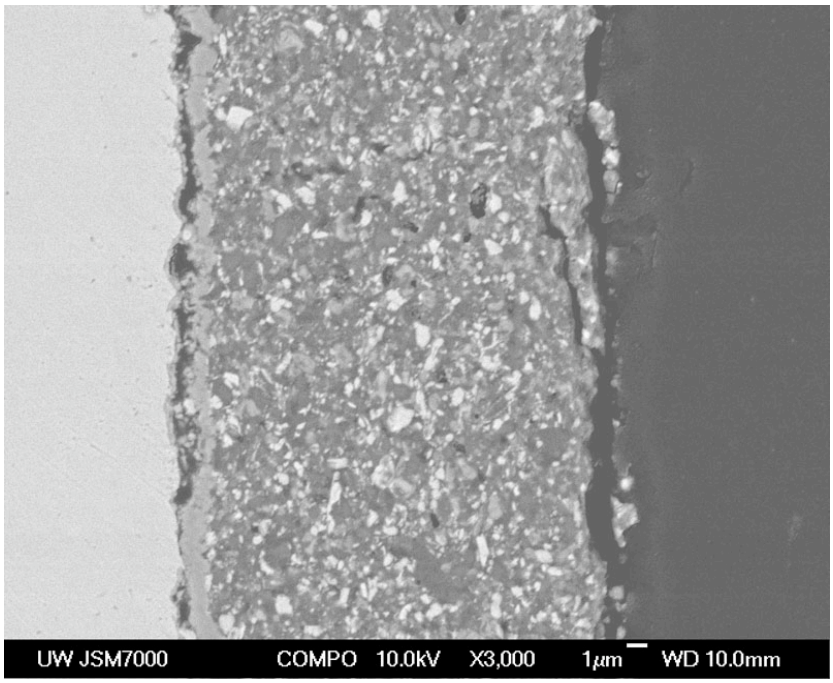

(a)

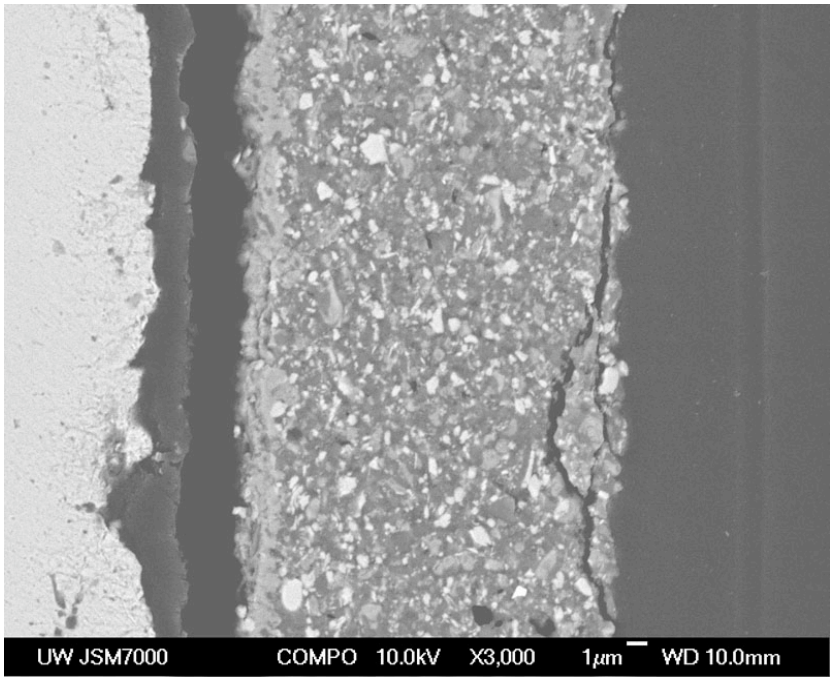

(b)

Figure 5.11: Diffusion layer causes weakness at the coating-substrate interface for samples pyrolyzed at 1000°C. Coatings debonded (a) partially; (b) completely.

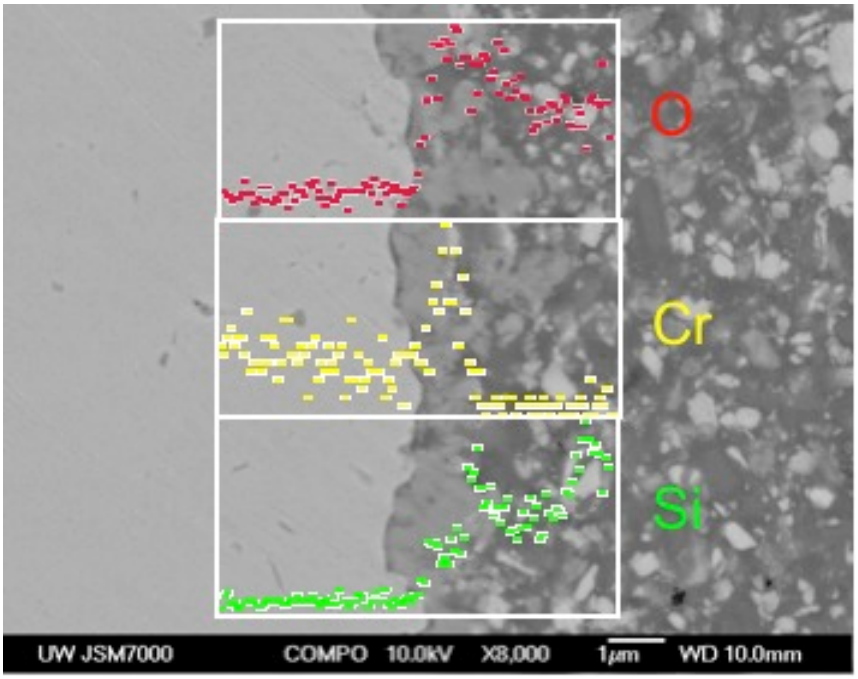

Figure 5.12: EDS study at the interface of 30 vol% $ZrSi_2$-filled PHMS coating system pyrolyzed at 1000℃. The interface layer is rich in elements like oxygen, chromium and silicon.

Coating thickness as a function of both pyrolysis temperature and withdrawal speed was measured in SEM and summarized in Table 5.2. It is interesting to note that the most significant reduction in the coating thickness (~20%) occurs between 150°C and 600°C due to polymer condensation and pyrolysis. The thickness remains stable from 600°C to 1000°C. The linear shrinkage of PHMS polymer in this temperature range has become very limited (~3%) and the total shrinkage of the coating is being compensated by the volume expansion from filler particles. As shown in Figure 5.13, all the coatings have experienced a slight thickness increase from 600°C to 1000°C.

Table 5.2: $ZrSi_2$ + PHMS coating thicknesses as temperature and withdrawal speed vary.

	100mm/min	300mm/min	700mm/min	1000mm/min
150°C	10.3	14.6	19.1	22.4
600°C	8.1	14.5	16.3	17.1
800°C	7.4	14.2	16.1	17.3
1000°C	7.8	14.0	16.4	17.8

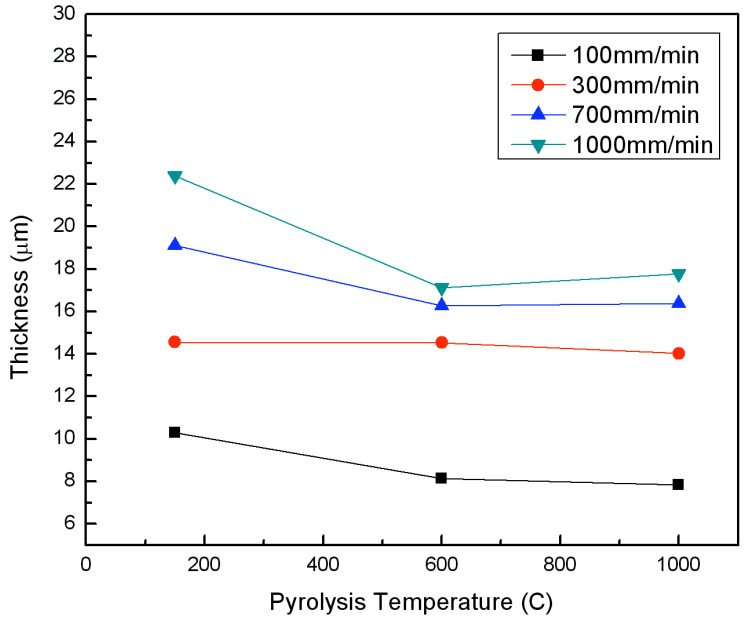

Figure 5.13: Trend of thickness change as a function of pyrolysis temperature in $ZrSi_2$-filled PHMS coating system.

5.3 Environmental Characterization

5.3.1 Oxidation Protection

The ability of the coatings to provide oxidation protection to both Inconel 617 and steel substrates was evaluated by conducting static oxidation tests in flowing air. In addition, to access the ability of the coatings to tolerate thermal stresses (due to thermal expansion

mismatch), cyclic oxidation tests were also conducted. The results are presented here. First, Figure 5.14 shows the weight gain, due to oxidation, of the bare Inconel 617 is compared to the weight gain for a coated substrate. A range of coatings that have been discussed above were investigated. These tests were conducted at 800 ^{0}C for 100 hours. The results are shown in Figure 5.14 where the weight gain of the bare sample has been compared to a range of coated samples

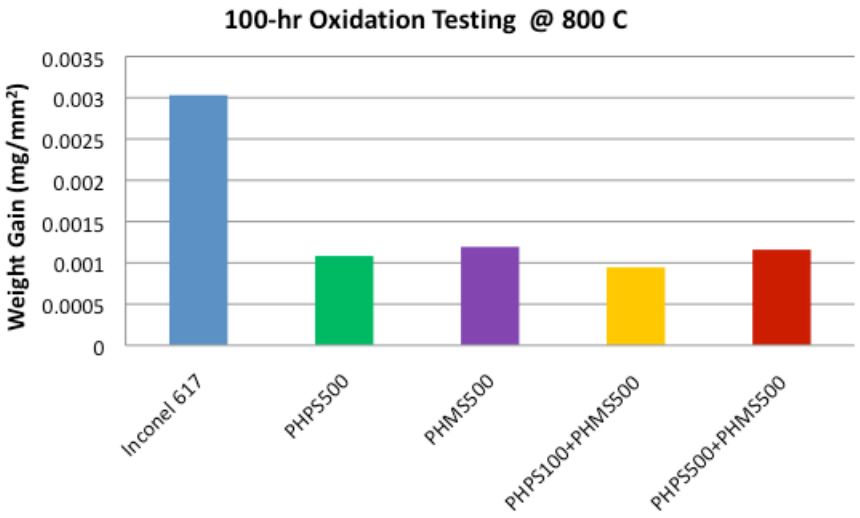

Figure 5.14: Effect of coating on the weight gain of Inconel 617 alloys (static oxidation test in flowing air for 100 hours at 800 ^{0}C). Note that all the coated systems have 2-3 lower weight gain indicating the oxidation protection provided by the coatings.

Similar studies were conducted on steel and once again the coatings provided excellent oxidation protection. Figure 5.15 is a micrograph of a coated steel sample that has been exposed to 800 ^{0}C for 100 hours. It is clear that the interface between the coating and the

metal remains free of an oxide layer indicating excellent oxidation protection to the steel samples.

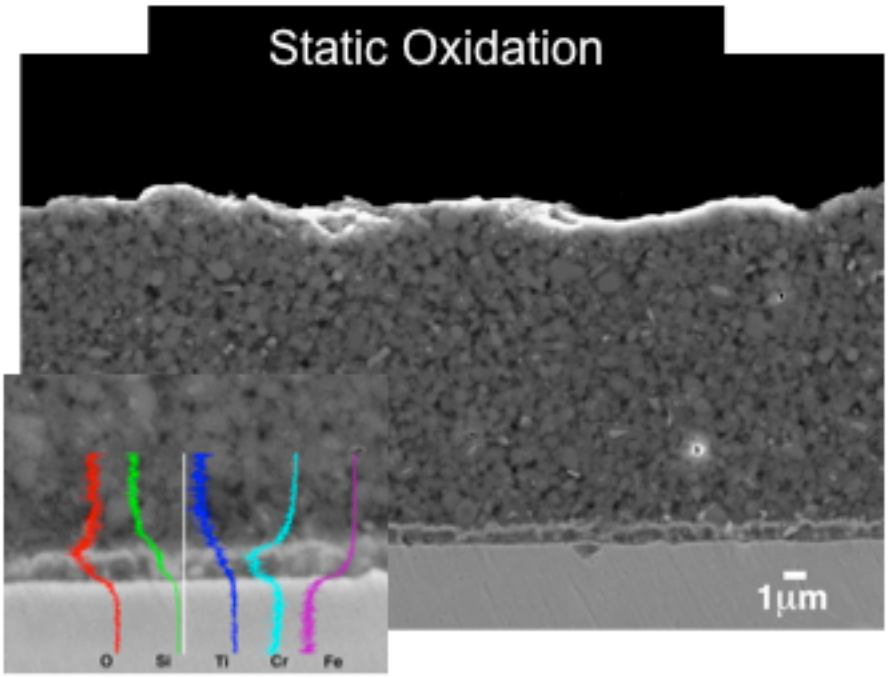

Figure 5.15: Effect of coating on the oxidation of steel (static oxidation test in flowing air for 100 hours at 800 ^{0}C). Note that there is no oxidation layer at the interface and the coating and substrate interface remains chemical and mechanically integral.

Finally, we conducted cyclic oxidation tests. In these the coated samples were cycled between from room temperature to 800 ^{0}C ten times. These tests were to ensure that the coatings do not delaminate (due to thermal expansion mismatch). The results of these are shown in Figure 5.16 for the steel substrates. The coating remains adherent to the substrates with no signs of delamination indicating that it is able to withstand the thermal stress due to thermal expansion mismatch.

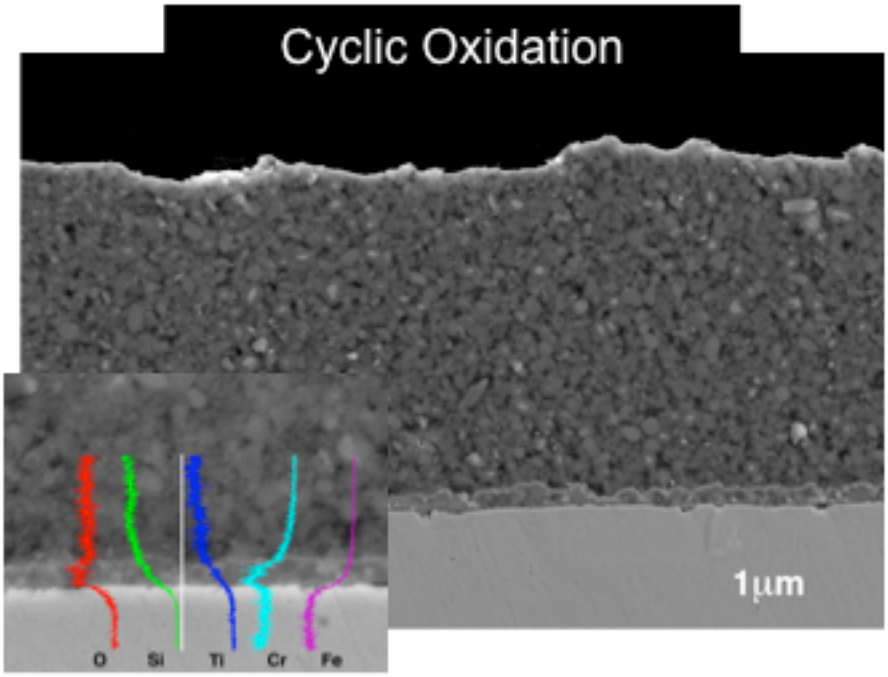

Figure 5.16: Effect of coating on the oxidation of steel (cyclic oxidation test in flowing air for cycling ten times between room temperature and 800 ^{0}C). Note that there is no oxidation layer at the interface and the coating and substrate interface remains chemical and mechanically integral with no signs of delamination.

5.4 Summary

We have shown that the coatings produced in this program have controllable thickness, microstructure and chemical composition. Optimally designed coatings have been shown to have good mechanical properties for the intended applications. Finally, these coatings provide excellent oxidation protection to both Inconel 617 and steel substrates under both static and cyclic conditions.

These coatings are now ready to be evaluated in service and for these we are seeking partners.

BIBLIOGRAPHY

1. Mitomo, M. and Y. Tajima, *Sintering, properties and applications of silicon-nitride and sialon ceramics.* Journal of the Ceramic Society of Japan, 1991. **99**(10): p. 1014-1025.
2. Riedel, R. and W. Dressler, *Chemical formation of ceramics.* Ceramics International, 1996. **22**(3): p. 233-239.
3. Kipping, F.S. and J.E. Sands, *XCIII.—Organic derivatives of silicon. Part XXV. Saturated and unsaturated silicohydrocarbons, Si4Ph8.* Journal of the Chemical Society, Transactions, 1921. **119**: p. 830-847.
4. Burkhard, C.A., *Polydimethylsilanes.* Journal of the AMerican Chemical Society, 1949. **71**(3): p. 963-964.
5. Chantrell, P.G. and E.P. Popper, *Inorganic Polymers and Ceramics*, in *Special Ceramics 1964*, E.P. Popper, Editor. 1965, Academic Press: London, UK. p. 87-103.
6. Verbeek, W., *Production of shaped articles of homogeneous mixtures of silicon carbide and nitride.* US Patent 3853567, 1974.
7. Winter, G., W. Verbeek, and M. Mansmann, *Production of shaped articles of silicon carbide and silicon nitride.* US Patent 3892583, 1975.
8. Yajima, S., et al., *Development of high tensile strength silicon carbide fiber using an organosilicon polymer precursor.* Nature, 1978. **273**(5663): p. 525-527.
9. Yajima, S., J. Hayashi, and K. Okamura, *Pyrolysis of a polyborodiphenylsiloxane.* Nature, 1977. **266**(5602): p. 521-522.
10. Yajima, S., J. Hayashi, and M. Omori, *Continuous silicon carbide fiber of high tensile strength.* Chemistry Letters, 1975(9): p. 931-934.
11. Yajima, S., et al., *Development of a silicon carbide fiber with high tensile strength.* Nature, 1976. **261**(5562): p. 683-685.
12. Yajima, S., K. Okamura, and J. Hayashi, *Structural analysis in continuous silicon carbide fiber of high tensile strength.* Chemistry Letters, 1975(12): p. 1209-1212.
13. Yajima, S., et al., *Synthesis of continuous SiC fibers with high tensile strength.* Journal of the American Ceramic Society, 1976. **59**(7-8): p. 324-327.
14. Yajima, S., T. Shishido, and M. Hamano, *SiC and Si3N4 sintered bodies with new borodiphenylsiloxane polymers as binder.* Nature, 1977. **266**(5602): p. 522-524.
15. Yajima, S., et al., *SiC sintered bodies with 3-dimensional polycarbosilane as binder.* Nature, 1976. **264**(5583): p. 238-239.
16. Rice, R.W., K.J. Wynne, and W.B. Fox, *Preparation of ceramics.* US Patent 4097294, 1978.
17. Walker, B.E., et al., *Preparation and properties of monolithic and composite ceramics produced by polymer pyrolysis.* American Ceramic Society Bulletin, 1983. **62**(8): p. 916-923.

18. Torrey, J.D., *Polymer derived ceramic composites as environmental barrier coatings on steel*, in *PhD Thesis. Materials Science and Engineering*. 2006, University of Washington: Seattle.
19. Blum, Y.D. and D.B. MacQueen, *Modifications of hydrosiloxane polymers for coating applications.* Surface Coatings International Part B-Coatings Transactions, 2001. **84**(1): p. 27-33.
20. Stackpoole, M.M., *Reactive processing and mechanical properties of polymer derived silicon nitride matrix composites and their use in coating and joining ceramics and ceramic matrix composites*, in *PhD Thesis. Materials Science and Engineering*. 2002, University of Washington: Seattle.
21. Wynne, K.J. and R.W. Rice, *Ceramics via polymer pyrolysis.* Annual Review of Materials Science, 1984. **14**: p. 297-334.
22. Torrey, J.D., et al., *Composite polymer derived ceramic system for oxidizing environments.* Journal of Materials Science, 2006. **41**(14): p. 4617-4622.
23. Bujalski, D.R., et al., *Stoichiometry control of SiOC ceramics by siloxane polymer functionality.* Journal of Materials Chemistry, 1998. **8**(6): p. 1427-1433.
24. Greil, P., *Active-filler-controlled pyrolysis of preceramic polymers.* Journal of the American Ceramic Society, 1995. **78**(4): p. 835-848.
25. Erny, T., et al., *Microstructure development of oxycarbide composites during Active-Filler-Controlled Polymer Pyrolysis.* Journal of the American Ceramic Society, 1993. **76**(1): p. 207-213.
26. Torrey, J.D. and R.K. Bordia, *Mechanical properties of polymer-derived ceramic composite coatings on steel.* Journal of the European Ceramic Society, 2008. **28**(1): p. 253-257.
27. Corriu, R.J.P., *Ceramics and nanostructures from molecular precursors.* Angewandte Chemie-International Edition, 2000. **39**(8): p. 1376-1398.
28. Mayer, J., et al., *Polymer-derived Si-based bulk ceramics Part II: microstructural characterization by electron spectroscopic imaging.* Journal of the European Ceramic Society, 1995. **15**(8): p. 717-727.
29. Pantano, C.G., A.K. Singh, and H.X. Zhang, *Silicon oxycarbide glasses.* Journal of Sol-Gel Science and Technology, 1999. **14**(1): p. 7-25.
30. Yu, S.H., et al., *Pyrolysis of titanium-metal-filled poly(siloxane) preceramic polymers - effect of atmosphere on pyrolysis product chemistry.* Journal of the American Ceramic Society, 1995. **78**(7): p. 1818-1824.
31. Riedel, R., et al., *Silicon-based polymer-derived ceramics: Synthesis properties and applications - A review.* Journal of the Ceramic Society of Japan, 2006. **114**(1330): p. 425-444.
32. Arkles, B., et al., *High density silicon dioxide coatings by UV and thermal processing.* Proceedings of Silicones in Coatings III, 2000.
33. Liew, L.A., et al., *Fabrication of SiCN MEMS by photopolymerization of pre-ceramic polymer.* Sensors and Actuators A-Physical, 2002. **95**(2-3): p. 120-134.
34. Radovanovic, E., et al., *Silicon oxycarbide glasses from silicone networks.* Journal of Non-Crystalline Solids, 1999. **248**(1): p. 37-48.
35. Shah, S.R. and R. Raj, *Mechanical properties of a fully dense polymer derived ceramic made by a novel pressure casting process.* Acta Materialia, 2002. **50**(16): p. 4093-4103.

36. Sieber, H., A. Kaindl, and P. Greil, *Biostructure derived ceramics.* Ceramic Engineering and Science Proceedings, 2000. **21**: p. 53-60.
37. Walter, S., et al., *Injection moulding of polysiloxane filler mixtures for oxycarbide ceramic composites.* Journal of the European Ceramic Society, 1996. **16**(4): p. 387-393.
38. Torrey, J.D. and R.K. Bordia, *Processing of polymer-derived ceramic composite coatings on steel.* Journal of the American Ceramic Society, 2008. **91**(1): p. 41-45.
39. Varga, T., et al., *Thermodynamically stable SixOyCz polymer-like amorphous ceramics.* Journal of the American Ceramic Society, 2007. **90**(10): p. 3213-3219.
40. Rice, R.W., *Ceramics from polymer pyrolysis, opportunities and needs--a materials perspective.* American Ceramic Society Bulletin, 1983. **62**(8): p. 889-892.
41. Riedel, R., et al., *Polymer-derived Si-based bulk ceramics Part I: preparation, processing and properties.* Journal of the European Ceramic Society, 1995. **15**(8): p. 703-715.
42. Lewinsohn, C.A., et al., *Silicon carbide-based materials for joining silicon carbide composites for fusion energy applications.* Journal of Nuclear Materials, 2002. **307**: p. 1232-1236.
43. Henager, C.H., et al., *Coatings and joining for SiC and SiC-composites for nuclear energy systems.* Journal of Nuclear Materials, 2007. **367**(Part B): p. 1139-1143.
44. Colombo, P., *Conventional and novel processing methods for cellular ceramics.* Philosophical Transactions of the Royal Society A-Mathematical Physical and Engineering Sciences, 2006. **364**(1838): p. 109-124.
45. Kim, Y.W., et al., *Fabrication of open-cell, microcellular silicon carbide ceramics by carbothermal reduction.* Journal of the American Ceramic Society, 2005. **88**(10): p. 2949-2951.
46. Rocha, R.M., et al., *SiOC ceramic foams synthesized from electron beam irradiated methylsilicone resin.* Journal of Materials Science, 2008. **43**(13): p. 4466-4474.
47. Vaklfahmetoglu, C. and P. Colombo, *A direct method for the fabrication of macro-porous SiOC ceramics from preceramic polymers.* Advanced Engineering Materials, 2008. **10**(3): p. 256-259.
48. Zeschky, J., et al., *Preceramic polymer derived cellular ceramics.* Composites Science and Technology, 2003. **63**(16): p. 2361-2370.
49. Raj, R., R. Riedel, and G.D. Soraru, *Introduction to the special topical issue on ultrahigh-temperature polymer-derived ceramics.* Journal of the American Ceramic Society, 2001. **84**(10): p. 2158-2159.
50. Suzuki, T., K. Inoue, I. Koshi and T. Isoda, *Ceramic coating from polysilazanes*, in *Advanced materials for future industries : needs and seeds : proceedings of the Second Japan International SAMPE Symposium and Exhibition, Nippon Convention Center, Chiba, Japan, December 11-14, 1991*, I.e.a. Kimpara, Editor. 1991, Society for the Advancement of Material and Process Engineering: Tokyo. p. 216-223.

51. Torrey, J.D. and R.K. Bordia, *Phase and microstructural evolution in polymer-derived composite systems and coatings.* Journal of Materials Research, 2007. **22**(7): p. 1959-1966.
52. Bill, J. and D. Heimann, *Polymer-derived ceramic coatings on C/C-SiC composites.* Journal of the European Ceramic Society, 1996. **16**(10): p. 1115-1120.
53. Greil, P., *Near net shape manufacturing of polymer derived ceramics.* Journal of the European Ceramic Society, 1998. **18**(13): p. 1905-1914.
54. Michalet, T., et al., *Elaboration of low shrinkage mullite by active filler controlled pyrolysis of siloxanes.* Journal of the European Ceramic Society, 2002. **22**(2): p. 143-152.
55. Soraru, G.D., et al., *Development of mullite-SiC nanocomposites by pyrolysis of filled polymethylsiloxane gels.* Journal of the European Ceramic Society, 2000. **20**(14-15): p. 2509-2517.
56. Liew, L.A., et al., *Processing and characterization of silicon carbon-nitride ceramics: application of electrical properties towards MEMS thermal actuators.* Sensors and Actuators A-Physical, 2003. **103**(1-2): p. 171-181.
57. Liew, L.A., et al., *Ceramic MEMS - New materials, innovative processing and future applications.* American Ceramic Society Bulletin, 2001. **80**(5): p. 25-30.
58. Liew, L.A., et al., *Fabrication of SiCN ceramic MEMS using injectable polymer-precursor technique.* Sensors and Actuators A-Physical, 2001. **89**(1-2): p. 64-70.
59. Liew, L.A., V.M. Bright, and R. Raj, *A novel micro glow plug fabricated from polymer-derived ceramics: in situ measurement of high-temperature properties and application to ultrahigh-temperature ignition.* Sensors and Actuators A-Physical, 2003. **104**(3): p. 246-262.
60. Liu, Y.P., et al., *Application of microforging to SiCN MEMS fabrication.* Sensors and Actuators A-Physical, 2002. **95**(2-3): p. 143-151.
61. Saravanan, R.A., et al., *Integration of ceramics research with the development of a microsystem.* Journal of the American Ceramic Society, 2003. **86**(7): p. 1217-1219.
62. Zeigmeister, U., *Development of a mechanical and oxidation protection for ceramic substrates*, in *Diploma Thesis. Department of Materials and Earth Sciences*. 2003, Darmstadt University of Technology: Darmstadt, Germany.
63. Motz, G., T. Kabelitz, and G. Ziegler, *Polymeric and ceramic-like SiCN coatings for protection of (light) metals against oxidation and corrosion*, in *Euro Ceramics VIII, Key Engineering Materials*, H. Mandal and L. Ovecoglu, Editors. 2004, Trans Tech Publications Ltd. p. 481-484.
64. Völger, K.W., *Ceramic Materials through a nonoxidic Sol-Gel process*, in *PhD Thesis. Department of Materials and Earth Sciences*. 2002, Darmstadt University of Technology: Darmstadt, Germany.
65. Iwamoto, Y., et al., *A hydrogen-permselective amorphous silica membrane derived from polysilazane.* Journal of the European Ceramic Society, 2005. **25**(2-3): p. 257-264.
66. Badzian, A., et al., *Silicon carbonitride: a rival to cubic boron nitride.* Diamond and Related Materials, 1998. **7**(10): p. 1519-1525.

67. Zhang, W., K. Zhang, and B. Wang, *Influence of temperature on the properties of SiCxNy:H films prepared by plasma-enhanced chemical vapour deposition.* Materials Science and Engineering B, 1994. **26**(2-3): p. 133-140.
68. Fukushima, M., et al., *Preparation of a transition metal containing polymethylsilsesquioxane hybrids and silicon oxycarbide ceramics - The fabrication of coating and self-supported films.* Journal of the Ceramic Society of Japan, 2005. **113**(1315): p. 210-215.
69. Blum, Y.D., *Hydroxysiloxane precursors for ceramic manufacture.* US Patent 5128494, 1992.
70. Blum, Y.D., S.M. Johnson, and M.I. Gusman, *Hydridosiloxanes as precursors to ceramic products.* US Patent 5635250, 1997.
71. Blum, Y.D. and G.A. McDermott, *Dehydrocoupling treatment and hydrosilylation of silicon-containing polymers, and compounds and articles produced thereby.* US Patent 5639844, 1997.
72. Galusek, D., R. Riedel, and M. Balog, *Polymer-derived Al2O3-SiC nanocomposites: preparation route vs. microstructure.* Fractography of Advanced Ceramics Ii, 2005. **290**: p. 121-128.
73. Goerke, O., E. Feike, and H. Schubert, *Spray winding, a novel one-step spray-technology to perform CMCs from preceramic polymers.* Journal of the European Ceramic Society, 2005. **25**(2-3): p. 181-185.
74. Gould, P.J., et al., *Thermophysical properties of ceramic-matrix composites produced by polymer pyrolysis.* Journal of Materials Science, 1995. **30**(18): p. 4507-4514.
75. Qi, G.J., et al., *Preparation of amorphous composites with polymer-derived silicon nitride matrix reinforced by three-dimensional silica fiber.* Journal of Non-Crystalline Solids, 2006. **352**(2): p. 189-192.
76. Ueno, K., S. Kose, and M. Kinoshita, *Toughness enhancement by polycarbosilane coating on SiC whiskers incorporated in Si3N4 matrix composite.* Journal of Materials Science, 1993. **28**(21): p. 5770-5774.
77. Scheffler, M., et al., *Nickel-catalyzed in situ formation of carbon nanotubes and turbostratic carbon in polymer-derived ceramics.* Materials Chemistry and Physics, 2004. **84**(1): p. 131-139.
78. Yang, W.Y., et al., *Synthesis of single-crystalline silicon nitride nanobelts via catalyst-assisted pyrolysis of a polysilazane.* Journal of the American Ceramic Society, 2005. **88**(2): p. 466-469.
79. Yang, W.Y., et al., *Synthesis of ceramic nanocomposite powders with in situ formation of nanowires/nanobelts.* Journal of the American Ceramic Society, 2008. **91**(4): p. 1312-1315.
80. Wan, J., M.J. Gasch, and A.K. Mukherjee, *Silicon carbonitride ceramics produced by pyrolysis of polymer ceramic precursor.* Journal of Materials Research, 2000. **15**(8): p. 1657-1660.
81. Seyferth, D., et al., *Preceramic polymers as reagents in the preparation of ceramics.* Journal of the American Ceramic Society, 1991. **74**(10): p. 2687-2689.
82. Suttor, D., H.J. Kleebe, and G. Ziegler, *Formation of mullite from filled siloxanes.* Journal of the American Ceramic Society, 1997. **80**(10): p. 2541-2548.

83. Bernardo, E., et al., *Novel mullite synthesis based on alumina nanoparticles and a preceramic polymer.* Journal of the American Ceramic Society, 2006. **89**(5): p. 1577-1583.
84. Starfire Systems Inc. *CMC Applications - Aerospace*. Available from: http://www.starfiresystems.com/ContentManager/index.cfm?Step=Display&ContentID=68.
85. Boulware, J., D. Andrews, and B. Bloudek. *Thermally protecting a reentry ballute with transient porosity*. in *AIAA SPACE 2007 Conference & Exposition*. 2007. Long Beach, California.
86. Harshe, R., C. Balan, and R. Riedel, *Amorphous Si(Al)OC ceramic from polysiloxanes: bulk ceramic processing, crystallization behavior and applications.* Journal of the European Ceramic Society, 2004. **24**(12): p. 3471-3482.
87. Bertsch, A., H. Lorenz, and P. Renaud, *3D microfabrication by combining microstereolithography and thick resist UV lithography.* Sensors and Actuators A-Physical, 1999. **73**(1-2): p. 14-23.
88. Bertsch, A., S. Jiguet, and P. Renaud, *Microfabrication of ceramic components by microstereolithography.* Journal of Micromechanics and Microengineering, 2004. **14**(2): p. 197-203.
89. Kong, J.S., et al., *A real time human-machine interface for an ultrahigh temperature MEMS sensor-igniter.* Sensors and Actuators A-Physical, 2003. **105**(1): p. 23-30.
90. Kim, Y.W., et al., *Fabrication of microcellular ceramics using gaseous carbon dioxide.* Journal of the American Ceramic Society, 2003. **86**(12): p. 2231-2233.
91. Scheffler, F., et al., *Zeolite covered polymer derived ceramic foams: novel hierarchical pore systems for sorption and catalysis.* Advances in Applied Ceramics, 2005. **104**(1): p. 43-48.
92. Zampieri, A., et al., *Zeolite coatings on microcellular ceramic foams: A novel route to microreactor and microseparator devices.* Advanced Materials, 2004. **16**(9-10): p. 819-+.
93. Colombo, P., et al., *Conductive ceramic foams from preceramic polymers.* Journal of the American Ceramic Society, 2001. **84**(10): p. 2265-2268.
94. Colombo, P., J.R. Hellmann, and D.L. Shelleman, *Thermal shock behavior of silicon oxycarbide foams.* Journal of the American Ceramic Society, 2002. **85**(9): p. 2306-2312.
95. Colombo, P. and J.R. Hellmann, *Ceramic foams from preceramic polymers.* Materials Research Innovations, 2002. **6**(5-6): p. 260-272.
96. Colombo, P., J.R. Hellmann, and D.L. Shelleman, *Mechanical properties of silicon oxycarbide ceramic foams.* Journal of the American Ceramic Society, 2001. **84**(10): p. 2245-2251.
97. Biasetto, L., et al., *Polymer-derived microcellular SiOC foams with magnetic functionality.* Journal of Materials Science, 2008. **43**(12): p. 4119-4126.
98. Colombo, P., E. Bernardo, and L. Biasetto, *Novel microcellular ceramics from a silicone resin.* Journal of the American Ceramic Society, 2004. **87**(1): p. 152-154.
99. Colombo, P., *Engineering porosity in polymer-derived ceramics.* Journal of the European Ceramic Society, 2008. **28**(7): p. 1389-1395.

100. Jang, D.H., et al., *Processing of highly porous, open-cell, microcellular silicon carbide ceramics by expansion method using expandable microspheres.* Journal of the Ceramic Society of Japan, 2006. **114**(1330): p. 549-553.
101. Kim, Y.W., H.D. Kim, and C.B. Park, *Processing of microcellular mullite.* Journal of the American Ceramic Society, 2005. **88**(12): p. 3311-3315.
102. Kim, Y.W., S.H. Kim, and C.B. Park, *Processing of closed-cell silicon oxycarbide foams from a preceramic polymer.* Journal of Materials Science, 2004. **39**(18): p. 5647-5652.
103. Kim, Y.W., et al., *Processing and mechanical properties of microcellular ceramics.* Science of Engineering Ceramics Iii, 2006. **317-318**: p. 899-903.
104. Baldus, P., M. Jansen, and D. Sporn, *Ceramic fibers for matrix composites in high-temperature engine applications.* Science, 1999. **285**(5428): p. 699-703.
105. Weisbarth, R. and M. Jansen, *SiBN3C Ceramic workpieces by pressureless pyrolysis without sintering aids: preparation, characterization and electrical properties.* Journal of Materials Chemistry, 2003. **13**(12): p. 2975-2978.
106. Bernard, S., et al., *Preparation of high-temperature stable Si-B-C-N fibers from tailored single source polyborosilazanes.* Journal of the European Ceramic Society, 2005. **25**(2-3): p. 251-256.
107. Miele, P., et al., *Recent developments in polymer-derived ceramic fibers (PDCFs): Preparation, properties and applications - A review.* Soft Materials, 2006. **4**(2-4): p. 249-286.
108. Motz, G. and R. Bordia, *Processing, structure and properties of ceramic fibers*, in *Handbook of textile fiber structure: Natural, regenerated, inorganic and specialist fibers (Volume 2)*, S. Eichhorn, et al., Editors. 2009, Woodhead Publishing Limited: Abington, Cambridge, UK.
109. Greil, P. and M. Seibold, *Modeling of dimensional changes during polymer ceramic conversion for bulk component fabrication.* Journal of Materials Science, 1992. **27**(4): p. 1053-1060.
110. Kitaoka, T. and Y. Seki, *A consideration on the packing of ultrafine particles.* Journal of the Ceramic Society of Japan, 1988. **96**(5): p. 585-589.
111. Schwartz, K.B. and D.J. Rowcliffe, *Modeling density contributions in preceramic polymer ceramic powder systems.* Journal of the American Ceramic Society, 1986. **69**(5): p. C106-C108.
112. Sidky, P.S. and M.G. Hocking, *Review of inorganic coatings and coating processes for reducing wear and corrosion.* British Corrosion Journal, 1999. **34**(3): p. 171-183.
113. Bordia, R.K. and A. Jagota, *Crack growth and damage in constrained sintering films.* Journal of the American Ceramic Society, 1993. **76**(10): p. 2475-2485.
114. Levich, V.G., *Motion and diffusion in thin liquid films*, in *Physicochemical Hydrodynamics*, N.R. Amundson, Editor. 1962, Prentice-Hall, Inc.: Englewood Cliffs, NJ.
115. Landau, L. and V. Levich, *Dragging of a liquid by a moving plate.* Acta Physicochimica, U.R.S.S., 1942. **12**(1-2): p. 42-54.
116. White, D.A. and J. Tallmadge, *Theory of drag out of liquids on flat plates.* Chemical Engineering Science, 1965. **20**(1): p. 33-37.

117. Groenveld, P., *High capillary number withdrawal from viscous Newtonian liquids by flat plates.* Chemical Engineering Science, 1970. **25**(1): p. 33-40.
118. Spiers, R.P., C.V. Subbaraman, and W.L. Wilkinson, *Free coating of a Newtonian liquid onto a vertical surface.* Chemical Engineering Science, 1974. **29**(2): p. 389-396.
119. Wilson, S.D.R., *The drag-out problem in film coating theory.* Journal of Engineering Mathematics, 1982. **16**(3): p. 209-221.
120. Agrawal, D.C. and R. Raj, *Measurement of the ultimate shear strength of a metal-ceramic interface.* Acta Metallurgica, 1989. **37**(4): p. 1265-1270.
121. Agrawal, D.C. and R. Raj, *Ultimate shear strengths of copper-silica and nickel-silica interfaces.* Materials Science and Engineering, 1990. **A126**: p. 125-131.
122. Hutchinson, J.W. *Mixed mode fracture mechanics of interfaces*. in *Metal-Ceramic Interfaces, Acta-Scripta Metallurgica Proceedings Series*. 1990: Pergamon Press.
123. Natesan, K., A. Purohit and D. L. Rink. *Fireside corrosion of alloys for combustion power plants*. in *The 16th Annual Conference on Fossil Energy Materials*. 2002. Baltimore, MD, USA.
124. Natesan, K., A. Purohit and D. L. Rink. *Coal-ash corrosion of alloys for combustion power plants*. in *The 17th Annual Conference on Fossil Energy Materials*. 2003. Baltimore, MD, USA.
125. Natesan, K. and J.H. Park, *Fireside and steamside corrosion of alloys for USC plants.* International Journal of Hydrogen Energy, 2007. **32**(16): p. 3689-3697.
126. Nava, J.C. and J. Henry, *Materials degradation mechanisms in coal-fired boilers.* Materials at High Temperatures, 2003. **20**(1): p. 55-60.
127. Micromeritics. *Saturn DigiSizer 5200*. Available from: http://www.micromeritics.com/Product-Showcase/Saturn-DigiSizer-5200.aspx.
128. Cleymand, F., et al., *Influence of indentation depth on the determination of the apparent Young's modulus of bi-layer material: Experiments and numerical simulation.* Surface & Coatings Technology, 2005. **200**(1-4): p. 890-893.
129. Gualandris, V., D. Hourlier-Bahloul, and F. Babonneau, *Structural investigation of the first stages of pyrolysis of Si-C-O preceramic polymers containing Si-H bonds.* Journal of Sol-Gel Science and Technology, 1999. **14**(1): p. 39-48.
130. Mutin, P.H., *Control of the composition and structure of silicon oxycarbide and oxynitride glasses derived from polysiloxane precursors.* Journal of Sol-Gel Science and Technology, 1999. **14**(1): p. 27-38.
131. Mutin, P.H., *Role of redistribution reactions in the polymer route to Silicon-Carbon-Oxygen ceramics.* Journal of the American Ceramic Society, 2002. **85**(5): p. 1185-1189.
132. Kleebe, H.J. and Y.D. Blum, *SiOC ceramic with high excess free carbon.* Journal of the European Ceramic Society, 2008. **28**(5): p. 1037-1042.
133. Samsonov, G.V., V. A. Lavrenko and L. A. Glebov, *Oxidation of chromium disilicide in oxygen.* Powder Metallurgy and Metal Ceramics, 1974. **13**(1): p. 36-38.
134. Gebwein, H., et al., *Fabrication of net shape reaction bonded oxide ceramics.* Journal of the European Ceramic Society, 2006. **26**(4-5): p. 697-702.
135. Du, H.L., et al., *Nanoscale studies of the early stages of oxidation of a TiAl-base alloy.* Oxidation of Metals, 2004. **62**(3-4): p. 175-193.

136. Chu, M.S. and S.K. Wu, *Oxidation behavior of Ti-50Al intermetallics with thin TiAl3 film at 1000 degrees C.* Oxidation of Metals, 2005. **63**(1-2): p. 1-13.
137. Lang, C. and M. Schutze, *TEM investigations of the early stages of TiAl oxidation.* Oxidation of Metals, 1996. **46**(3-4): p. 255-285.
138. Smith, G. and L. Shoemaker, *Advanced nickel alloys for coal-fired boiler tubing.* Advanced Materials & Processes, 2004. **162**(7): p. 23-26.
139. Viswanathan, R., *Materials technology for coal fired power plants.* Advanced Materials & Processes, 2004. **162**(8): p. 73-76.
140. Viswanathan, R. and W. Bakker, *Materials for ultrasupercritical coal power plants--boiler materials: Part 1.* Journal of Materials Engineering and Performance, 2001. **10**(1): p. 81-95.
141. Viswanathan, R. and W. Bakker, *Materials for ultrasupercritical coal power plants--turbine materials: Part II.* Journal of Materials Engineering and Performance, 2001. **10**(1): p. 96-101.
142. MatWeb of Automation Creations Inc. *Special Metals INCONEL Alloy 617*. Available from: http://www.matweb.com/search/datasheet.aspx?MatGUID=adf2123d8e494e75aef7417989ffea92.
143. MatWeb of Automation Creations Inc. *304 Stainless Steel*. Available from: http://www.matweb.com/search/DataSheet.aspx?MatGUID=abc4415b0f8b490387e3c922237098da.
144. Spiers, R.P., C.V. Subbaraman, and W.L. Wilkinson, *Free coating of Non-Newtonian liquids onto a vertical surface.* Chemical Engineering Science, 1975. **30**(4): p. 379-395.
145. Tallmadge, J., *Withdrawal of flat plates from power law fluids.* AIChE Journal, 1970. **16**(6): p. 925-930.